Multi-Epoch VLBI Analysis of Extragalactic Jets in Active Galactic Nuclei

Jan-Christopher Pappert

MASTERARBEIT

eingereicht an der

Fakultät für Physik und Astronomie
Julius-Maximilians-Universität Würzburg

im Juni 2017

Verantwortlicher Hochschullehrer: Prof. Dr. Matthias Kadler

Declaration

I hereby declare and confirm that this thesis is entirely the result of my own original work. Where other sources of information have been used, they have been indicated as such and properly acknowledged. I further declare that this or similar work has not been submitted for credit elsewhere.

Würzburg, June 22, 2017

Jan-Christopher Pappert

Zusammenfassung

Aktive Galaxienkerne (AGN) sind außergewöhnlich helle astrophysikalische Objekte, die starke nicht-thermische Strahlung im kompletten elektromagnetischen Spektrum aufweisen (von Radiofrequenzen bis zum Gamma-ray Energie Bereich). Einige AGN weisen sogenannte *jets* auf (stark kollimierte Materieausflüsse, die aus dem Zentrum von AGN ausströmen). Die spektrale Energieverteilung von AGN hat eine charakteristische Struktur, welche durch einen Doppelhöcker gekennzeichnet ist. Aktive Galaxienkerne gehören zu den stärksten beständigen Quellen des Universums und sind noch nicht vollständig verstanden, obwohl sie seit fast einem halben Jahrhundert untersucht werden. Zum aktuellen Stand der Forschung werden AGN durch das *Unified Model of AGN* (Antonucci, 1993) beschrieben, welches auch die unterschiedlichen Subklassen von AGN erklärt. Hiernach sind AGN sehr helle Kerne von fernen Galaxien. Ihre innere Struktur ist durch ein supermassives schwarzes Loch gegeben, welches von einer Akkretionsscheibe und einem Staubtorus umgeben ist. Unterschiedliche Klassen von AGN werden durch ihre Helligkeit und den Sichtwinkel relativ zur Quelle erklärt.

Das *TANAMI*-Projekt (Tracking Active Galactic Nuclei with Austral Milliarcsecond Interferometry) beobachtet regelmäßig Quellen von der Südhalbkugel aus. Es beinhaltet 86 Quellen südlich einer Deklination von $-30°$, die alle 3 oder 4 Monate mittels Radiofrequenzen beobachtet werden. TANAMI ist ein Array von Radioteleskopen, die die *VLBI* (Very Long Baseline Interferometry) Technik nutzen. Dies resultiert in einer bemerkenswerten Auflösung in der Radiobildgebung, die es erlaubt Quellen auf subparsec Skalen zu untersuchen. Ferner ist TANAMI Teil eines Multiwellenlängen Monitoring Programms. Beispielsweise wurde ein großer Teil der TANAMI Quellen auch vom *Fermi Gamma-ray Space Telescope* detektiert.

Diese Arbeit beinhaltet einen Katalog von AGN, welche durch das TANAMI-Array im X-Band beobachtet wurden. Die innere Jet-Struktur wurde untersucht, indem die Helligkeitsverteilung in bis zu neun Epochen rekonstruiert und anschließend kinematisch analysiert wurde. Die daraus abgeleiteten Helligkeitstemperaturen, Flussdichten und Leuchtkräfte erlauben Rückschlüsse auf intrinsische Jet-Eigenschaften wie Geschwindigkeit und Inklinationswinkel.

Abstract

AGN are exceptionally bright, astrophysical objects that exhibit strong non-thermal emission across the electromagnetic spectrum (ranging from radio frequencies to gamma-ray energies). Some AGN show jets (well collimated material outflow emerging from the center of AGN). Broadband spectral energy distributions of AGN show a characteristic double-humped structure. Active Galactic Nuclei, which belong to the most powerful and persistent sources in the universe, have been studied for about half a century. However, there still remain questions unanswered about their extreme physics till this day. Different phenomena regarding AGN are summarized in the *unified model* of AGN (Antonucci, 1993; Urry & Padovani, 1995) According to the Unified model, AGN are highly luminous cores of distant galaxies. Their substructure exhibits a supermassive black hole which is surrounded by an accretion disk and a dusk torus. Different classes of AGN are explained by the luminosity, the viewing angle relative to the source and the radio loudness.

The *TANAMI* program (Tracking Active Galactic Nuclei with Austral Milliarcsecond Interferometry) tracks sources on the southern hemisphere. It features 86 sources south of $-30°$ declination. Each source is observed every 3 or 4 months at radio frequencies. TANAMI consists of an array of radio telescopes and makes use of the *VLBI* (Very Long Baseline Interferometry) technique. This results in unprecedented resolution in radio imaging, resolving structures down to scales of less than a milliarcsecond, which means that sub-parsec scale morphology of sources can be studied. Furthermore, TANAMI is complemented with multiwavelength monitoring by the Fermi Gamma-ray Space Telescope, as a majority of its sources are also detected by Fermi.

This thesis contains a catalog of AGN, observed by the TANAMI array in the X-band. The jet structure was studied by generating brightness distribution maps of multiple sources in up to nine epochs for each of them. Sources that exhibited extended structure were used for kinematic analysis by fitting components with circular Gaussian models. This way, the brightness temperature, flux density and luminosities were studied, allowing inference about intrinsic jet properties such as speed and inclination angle.

Contents

Chapter 1

Active Galactic Nuclei

1.1 Discovery and history

The history of Active Galactic Nuclei (AGN) is tightly linked to the history of radio astronomy, since many of them are bright radio sources with puzzling morphology in the radio bands. Surprisingly, radio astronomy is a very recent branch of astronomy. It was not until 1933 that Karl Jansky discovered an extra-terrestrial radio source from the Milky Way, thereby opening a new window to the universe. This bright source turned out to be our galactic center. Notable discoveries followed. The first radio sky map was available in 1937 (Reber, 1988), revealing that stars are not the most dominant emitters in the radio regime. In 1954, the brightest radio sources with known optical counterparts were identified (Baade & Minkowski, 1954). Another breakthrough for cosmology was the discovery of the cosmic microwave background in 1965 by Penzias & Wilson (1965). In 1968, the first pulsar was discovered (Hewish et al.). Today, radio astronomy is most notable for achieving the highest resolutions in astronomy. This is possible because of VLBI (the Very Long Baseline Interferometry) technique. It is for this reason that radio astronomy is vital for the study of AGN and jets. The discovery of AGN dates back to H.D. Curtis, who noticed 'A curious straight ray' in M87. The first systematic studies can be credited to Carl Seyfert in the 1940s. He showed that the emission lines of AGN were unique in the sense that they could not be attributed to H II region, and that we were dealing with a new class of objects. Later, this led to the classification of AGN based on their optical emission lines in Seyfert 1 and 2 galaxies. In 1965, Ryle et al. identified the extended emission of AGN as hot spots and lobes associated with those sources.

1.2   Phenomenology & Unification

AGN refers to a galactic central region, which is overall distinctly brighter than regular galaxies (or the host galaxy for that matter). The main characteristic here is the high luminosity of $10^{42}\,\mathrm{erg\,s^{-1}} \lesssim L \lesssim 10^{48}\,\mathrm{erg\,s^{-1}}$. AGN exhibit powerful, non-thermal broadband emission which stands in contrast to non-active galaxies. The latter is dominated by thermal emission from stars, which can be modeled as a superposition of many Planck spectra, yielding a relatively narrow distribution. AGN possess a much broader spectrum, ranging from the radio over the X-ray up to the very high energy gamma-ray regime. However, there are various types of AGN, which vary substantially in terms of spectral and structural features. Furthermore, they exhibit variability across the whole electromagnetic spectrum on various time scales (minutes to months). Their classification is mainly based on their optical and radio properties. The broadband spectrum can be described by a power law, which again reflects the non-thermal emission. The compact and extremely luminous appearance originally led to the name "quasi-stellar objects" (QSOs) or "quasi-stellar radio source" (Quasar) when identified with a radio source. The distinction is mainly historic, however. The following phenomenological introduction is based on Krolik (1999), more detailed information can also be found in Boettcher et al. (2012).

1.2.1   Classes of AGN

Seyfert Galaxies

Seyfert galaxies are the most common class of AGN. They feature strong emission lines in the optical wavelengths. The phenomenology of this class of AGN is thus governed by the quantum mechanical description of atomic nuclei, which predicted allowed, semi-forbidden and forbidden lines. It is noteworthy that in an astrophysical context, even generally forbidden lines can be observed after collisional excitation, although a low density medium is required in this case. The classification of Seyfert galaxies is based on these emission lines which were discovered by Seyfert in 1943. Khachikyan & Weedman later introduced the distinction between Seyfert 1 galaxies (broad emission lines, indicating velocities up to $10^4\,km s^{-1}$) and Seyfert 2 galaxies (narrow, forbidden lines) in 1971. Seyfert 1 galaxies usually also have a higher level of continuum emission. However, it quickly became apparent that a finer classification was needed and thus, more nuanced classifications were introduced (Seyfert 1.5, Seyfert 1.8). The emission lines can be used to measure the distance by using the Doppler-Shift. Seyfert galaxies are spiral galaxies and (with few exceptions) radio-quiet. In optical images, Seyfert galaxies feature bright, point-like cores, but the host galaxy is generally still detectable.

Radio Galaxies

There is an apparent dichotomy in radio-loud and radio-quiet objects. The latter exhibits radio emission as well, however only very faint. Radio loudness can be defined by considering the flux density of the object in the radio and in the optical: If the ratio of radio flux to optical flux is greater than 10, an AGN is considered radio-loud. Otherwise, it is radio-quiet (only about 10 % of AGN are radio-loud). Radio galaxies are characterized mainly by their properties in the radio band, manifesting itself in the dominance of non-thermal radiation. Their strong radio emission can be observed over several orders of magnitude in size, ranging from their structure on parsec-scales up to the large-scale structure up to a few Mpc (Neeser et al., 1995). Radio-loud AGN exhibit powerful radio jets and are usually located in elliptical host galaxies. It should be mentioned that radio-quiet jets might also be able to produce jets (Stocke et al., 1992). They can be considered as a radio-loud analog to Seyfert galaxies, as they show the same distinctions based on optical emission lines. This leads to the classification of radio galaxies as Broad/Narrow Line Radio galaxies (BLRG/NLRG). Furthermore, the morphology and surface brightness of hot spots and radio lobes can be described. This was first introduced by Fanaroff & Riley (1974), distinguishing two types of AGN: Fanaroff-Riley (FR) I radio galaxies show a bright core but low power, two-sided jets. FR II radio galaxies exhibit a stronger one-sided jets and bright lobes and hot spots. The distinction also manifests in a rough distinction in the radio power with the dividing line being located at around $10^{25}\,\mathrm{W\,Hz^{-1}}$.

QSOs and Quasars

QSOs (Quasi-Stellar Objects) and *Quasars* (quasi-stellar radio sources) are the brightest objects in this classification. Historically, quasars were first discovered in the radio, then later found and identified in the optical regime. They are the among the most luminous, and also most distant AGN, and are typically found at high redshifts (Schmidt, 1963). The optical properties of QSOs are similar to those of Seyfert galaxies, with slightly weaker absorption features from the galaxy and weaker narrow lines. The distinction into Type 1 and Type 2 sources based on emission lines can be applied to QSOs similarly as well. They can be further classified based on magnitude, and also divided into radio-loud and radio-quiet sources (with about 10 times more radio-quiet QSOs than radio-loud ones).

Blazars

Blazars are AGN whose host galaxy can not be detected. They exhibit very luminous non-thermal emission in the broadband spectrum, up to the highest energies. Blazar emission is highly variable and strongly polarized. They

show relativistic jets which can be resolved with VLBI. Blazars can be further characterized based on their optical emission lines: Those with strong and broad emission lines are named *flat-spectrum radio quasar* (FSRQ) while blazars with weak or completely missing lines are called *BL Lac objects* (so-called after the AGN BL Lacertae). FSRQs are essentially more luminous versions of BL Lac objects with similar emission-line spectrum like those found in QSOs. Furthermore, particularly variable sources in the optical wavelengths are characterized as *optically violent variable* (OVV). An alternative classification is based on the double-hump structure in the spectral energy distribution (SED). Different classes are defined based on the location of the synchrotron peak (low-frequency, intermediate and high-frequency synchrotron peaked sources). This characterization gives rise to the so-called *blazar-sequence*: Ghisellini et al. (1998) and Fossati et al. (1998) showed that more luminous blazars feature a shift in both the synchrotron and the IC peak towards lower frequencies. At the same time, the IC peak also grew more dominant over the synchrotron peak for higher luminosities. While the blazar sequence is still under debate, recent research seems to confirm the general trend (Ghisellini, 2016). Blazars only represent a minority among the general population of AGN. Nevertheless, they dominate source catalogs in the gamma-ray regime (for instance more than 50% of sources detected by *Fermi*/LAT are blazars Acero et al. (2015)). They also encompass the largest group of sources for radio samples (MOJAVE, TANAMI) since their radio emission is strongly beamed. A detailed discussion of blazars can be found in (Véron-Cetty & Véron, 2000).

LINER

This subclass encompasses low-luminosity AGN which can be prevalently found in the nearby universe. *low-ionization nuclear emission-line regions* (LINERs) cover the lower end of the luminosity distribution of AGN in the optical and radio wavelengths. They feature strong emission lines which are similar in width to those found in Seyfert 2 galaxies. It is suspected that not all of them are AGN (Heckman & Best, 2014).

Compact steep spectrum sources

Sources which feature a characteristic turnover in their radio spectrum are named *compact steep spectrum sources* (CSS). Their morphology is very compact with a large scale size of less than 10 kpc. CSS are powerful radio emitters and might indicate an early stage of AGN evolution (Kunert-Bajraszewska et al., 2010). Sources with a turnover frequency of more than 1 GHz are called *Gigahertz-peaked spectrum objects* (GPS).

Table 1.1: The phenomenology of active galactic nuclei. Credit: Matthias Kadler

Type	Radio Loudness	Emission Lines	Luminosity	Jets?	Radio Morphology
Seyfert 1	radio-quiet	broad, narrow	low	-	-
Seyfert 2		narrow	low	-	-
QSO (Type 1)		broad, narrow	high	-	-
QSO (Type 2)		narrow	high	-	-
BLRG	radio-loud	broad, narrow	low	yes	FR 1
		broad, narrow	high	yes	FR 2
NLRG		narrow	low	yes	FR 1
		narrow	high	yes	FR 2
BL Lac		-	low	yes	compact
FSRQ		broad, narrow	high	yes	compact

1.2.2 Unification

The Unified model of Active Galactic Nuclei shall be outlined (Lawrence, 1987; Urry & Padovani, 1995; Antonucci, 1993). The general assumption is that all AGN are structurally similar and the phenomenology can be explained by their geometry. The central engine is a *supermassive black hole* (SMBH, $M \sim 10^7 - 10^8 M_\odot$), which is accreting material. Accretion on a compact object is the only mechanism to release this amount of energy within less than a cubic kiloparsec (Shakura & Sunyaev, 1973). Gas and dust orbiting the central SMBH form an accretion disk, continuously dissipating energy and losing angular momentum through friction and radiation. The spectrum of a thin accretion disk can be described by stretched black body emission with a radial temperature dependence. Apart from the accretion disk ($r \sim 10^{-3}$ pc), AGN feature a torus of dust a little farther out ($r \sim 1-10$ pc). Dust tori are clumpy structures with time variant absorption, which obscure certain features if the inclination angle towards the source is high. However, there are also fast rotating gas clouds, which (excited by the thermal emission from the accretion disk) feature line emission. These can be categorized in two groups: Very fast rotating clouds are situated at $r \sim 0.01-0.1$ pc. They are very dense and exhibit broad line emission (*BLR - Broad Line Region*). These emission lines are obscured by the dust torus at large inclination angles, explaining the phenomenology of Seyfert 2 Galaxies and Narrow Line Radio Galaxies. Farther out ($r \sim 100-1000$ pc) low density clouds can be found which feature narrow line emission as well as forbidden lines (*NLR - Narrow Line Region*). Notably, radio-loud AGN exhibit symmetric, collimated jets of relativistic outflowing material perpendicular to the plane of the accretion disk. Due to Doppler boosting (ref sec. 1.6.2), only the jet oriented towards the observer can be detected. Furthermore, the

projection effect lets jets appear at very high speed, exhibiting superluminal motion (up to 50 c, see Lister et al., 2013). Different phenomenology can be explained by luminosities, the existence of a jet and the orientation of the source to the line of sight (inclination angle) as well as projection effects and Doppler Boosting. The dust torus prevents the detection of broad lines from the BLR if the inclination angle is high. For moderate angles all those lines can be detected. For very small angles, the beamed luminosities of the jet overpowers any other emission and optical emission lines are drowned out. An illustration of the unification model of Active Galactic Nuclei is shown in Figure 1.1

It should be noted that the Unified model is still strongly debated. More AGN need to be explored in order to reach statistically significant conclusions on the unification. Problems arise from the multitude of different instruments that are required and varying data quality. There are still fundamental questions about AGN that remain unresolved to this day. The origin and formation processes of jets are still unclear. Furthermore, the question remains of what jets are made of. Both purely leptonic models and models which propose a mix of hadronic and leptonic processes have been proposed. It remains to be discovered what leads to the collimation of the jet's plasma.

1.3 Structure of AGN

Central engine

The paradigm of accretion onto a very massive, compact object was well accepted since the early days of AGN research. Jets with highly relativistic velocities have to originate from regions with similar escape velocities. Only black holes and neutron stars would be sufficiently compact, and only black holes can reach the required mass. This can be underlined by the Eddington limit, which describes the maximum luminosity emitted from an object with mass M in equilibrium with radiation pressure and in-falling matter: Of course, relativistic beaming has to be considered in this argument. Again, neutron stars cannot reach the mass outlined by the Eddington limit. Furthermore, the required efficiency of energy conversion favors such an accretion model. In such a model, matter is transported inward while angular momentum is transported outward due to the viscosity of the medium. Particles on the innermost stable orbit can be accreted into the black hole. This leads to a disk of matter ("Accretion disk") with optical and X-ray emission, cooling the flow. This phenomenon shows similarities to compact stellar systems like X-ray binaries (Marscher, 2006). Side-note: Even non-active galaxies may contain a SMBH. One interesting object in this context is the presumed center of our own galaxy, Sgr A*.
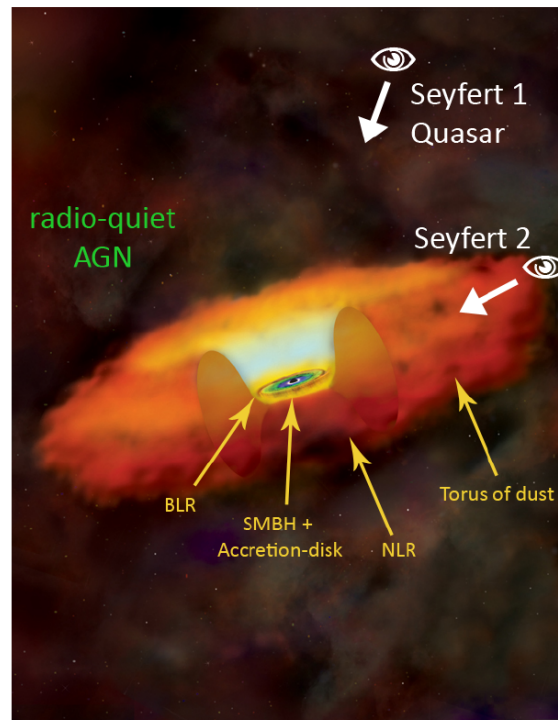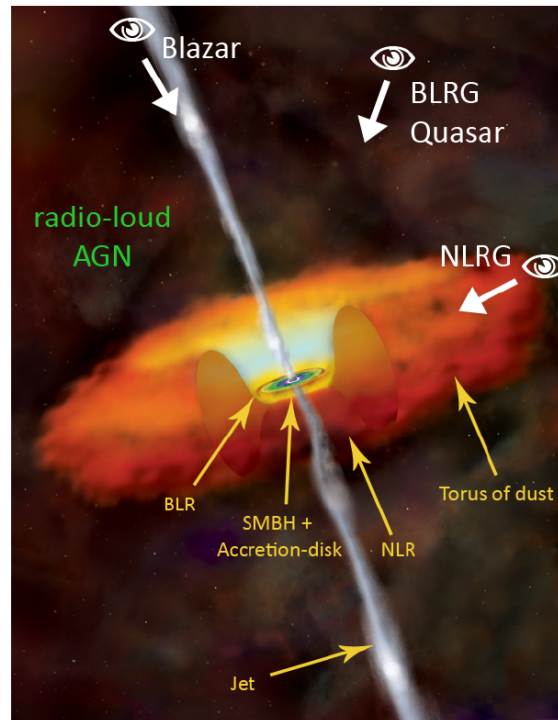
Figure 1.1: An illustration of the unified model of an Active Galactic Nucleus. Different regions are indicated with yellow arrows and text while white arrows and text convey the classification of how an AGN would be perceived under such an inclination angle (adaptation from Trüstedt, 2013, original image credit: NASA/CXC/M.Weiss).

Surroundings: The accretion disk

Unlike the spectra of ordinary galaxies, which are defined by the accumulated stellar (and thus thermal) emissions, the continuum spectra of AGN are highly non-thermal. However, a so-called *big blue bump* of thermal emission can often be detected in the optical/ultraviolet. This bump can be associated with thermal emission from the accretion disk.

Broad Line Region

The BLR is a region of very hot and dense gas clouds ($n \sim 10^{10} \, \mathrm{cm}^{-3}$). If the gas was uniformly distributed instead, the medium would be optically thick due to Thomson scattering. It is located still very close to the SMBH, rotating very fast and exhibiting turbulent motion (which manifests itself in the broad emission lines). Line widths reach orders of $1000 \, \mathrm{kms}^{-1}$, which can not be explained by thermal broadening as this would suggest temperatures at which the gas would be completely ionized, thus no lines would be observed to begin with. The variability further indicates that this region is close to the SMBH.

Narrow Line Region

The NLR exhibits narrow but strong permitted, but also narrow forbidden lines. Line widths reach the order of $100 \, \mathrm{kms}^{-1}$. Just like the BLR, the NLR consists of gas clouds. However, these clouds are colder and less dense ($n \sim 10^3 - 10^6 \, \mathrm{kms}^{-1}$). The NLR is thought to be farther away, approximately $r \sim 100 \, \mathrm{pc} - 10 \, \mathrm{kpc}$.

Symmetrical Jets

The jets can be seen in radio-loud AGN from sub-pc to kpc scales. Jets are highly relativistic, collimated outflow of plasma from the nucleus. Both one-sided and two-sided systems can be observed, which can be explained by Doppler boosting. They can be detected in the radio, but also at optical and X-ray energies. In the radio bands, jets can reach scales up to $\sim \mathrm{Mpc}$. It is possible to resolve jets close to the SMBH with sub-pc scale resolution using the VLBI technique. Jet features can be detected to reach superluminal motion.

Radio lobes

The very extended emission can be explained by jet-interaction with the inter-galactic medium. Here, the flow is strongly inhibited and large lobes are produced. This is not a single-event process, but rather continuously fueled by the jet.

1.4   Relativistic Jets

1.4.1   Jet phenomenology

Jets are characteristic for radio-loud AGN, but are also hosted in other AGN. They can be observed on a wide range of spatial scales, ranging from sub-pc to Mpc scales (Bridle & Perley, 1984; Zensus, 1997). The underlying physics depend strongly on the scale on which we seek to describe the jet, for instance interaction with the ambient medium has to be factored in for the largest scales. The substructure of jets can be studied using high resolution radio imaging via the Very Long Baseline Interferometry. This allows us to study jets on pc down to sub-pc scales. The structure on these scales is either compact, or features a jet extending from a bright central emission region which is dubbed *core*. Luminous emission regions outside the core are named *components*. Such features can be quasi-stationary, or even move with apparent superluminal motion in reference to the core. Blazars usually have a single-sided jet while radio galaxies may show one-sided or two-sided jets (this is due to viewing angle and Doppler boosting). The radio spectrum of pc-scale jets tends to be flat (in the range of $-0.5 < \alpha < 0.5$), especially the core which can be modeled by synchrotron self-absorption. The jet components tend to feature a steeper spectrum (Hovatta et al., 2014). Surveys show that the overall flow follows a uniform motion, while individual components can move independently (Kellermann et al., 2004; Lister et al., 2009b). Kellermann et al. further imply that components are detected with higher speed at larger frequencies, suggesting that different frequencies allow the observation of different parts of the jet. The motion of jets features is generally considered ballistic, but significant acceleration (both positive and negative) has been measured (Homan et al., 2015; Lister et al., 2013) both parallel and perpendicular to the jet axis. Piner et al. (2012) and Lister et al. (2013) showed that non-ballistic behavior is very common in blazar jets. While jets are often well collimated, some also show twists and bends (Zensus, 1997). However, even small intrinsic changes in the orientation of the jet are largely amplified in images due to the projection effect. There are multiple possible explanations for changes in the apparent jet orientation. Generally speaking, it is hard to distinguish between a change in the Lorentz factor and a change in the angle to the line of sight. While positive acceleration is more like to be found near the jet base, deceleration can be found farther out. An idealized jet would feature a conical geometry with a given opening angle. New plasma is then ejected into the stream (Blandford & Königl, 1979). This can for instance be detected indirectly by flux density changes over time, resulting in new and bright emerging features. If the injected plasma has a higher density compared to the rest of the jet, a shock front can be created (shock-in-jet model). The shock front then passes the acceleration and collimation region which is dominated by magnetic forces.

Particles are accelerated at when crossing the shock-front to the point where accelerated particles can emit up to gamma-ray wavelengths which can be detected in the form of flares (Fromm et al., 2011; Marscher & Gear, 1985). Such shocks can also be created by a difference in jet pressure relative to the pressure of the ambient medium. An expansion of an over-pressured jet is followed by recollimation, resulting in a recollimation shock, which in turn leads to an increase in intensity and polarization (Gómez et al., 1997; Agudo et al., 2012). Furthermore, recollimation shocks can become standing shocks. This opens up the possibility of shock-shock interactions (Perucho, 2013; Fromm et al., 2016). It has been shown that for high frequencies, the core can also be a recollimation shock rather than the $\tau = 1$ region (Gómez et al., 2016). Close to the black hole, the jet is driven by a toroidal magnetic field. Here, current-driven instabilities (CDI) can occur due to differences in magnetic flux. In the kinetic regime, Kelvin-Helmholtz instabilities (KHI) may occur due to differences in velocity within the plasma itself. Jet features can be strongly polarized, but rarely are so homogeneously throughout the whole jet. Jet polarization can also allow conclusions about the underlying magnetic field (Jorstad et al., 2005; Hovatta et al., 2012). However, since the underlying processes are not yet fully understood, VLBI needs to keep playing its crucial role by describing the kinematic behavior of extragalactic jets. On large scales, the morphologies of jets show a large variety. The kiloparsec-scale structure is dominated by the interactions of the jet plasma with the interstellar or the intergalactic medium, which leads to the formation of radio lobes and the eventual dissipation of the jet (Bridle & Perley, 1984). Thus, the morphology is strongly affected by the ambient medium and Kelvin-Helmholtz instabilities. As are result, simulations and emission models for these scales require different parameters compared to pc scale jets (Hardcastle & Krause, 2013).

1.4.2 Jet formation and evolution

As already hinted in Section 1.4.1, the origin and formation processes of jets are not yet fully understood. Many models have been formed that are based on magnetohydrodynamics (MHD), general relativity (GR) and electrodynamics. Parts of the processes are well explained while others remain unclear.
In order to establish a collimated flow at relativistic velocities, strong pressure gradients are required. According to Marscher (2009), jets with Lorentz factors of $\gamma > 10$ combined with a collimation of less than $1°$ cannot be formed via gas dynamics. Magnetic forces are the only viable option to provide enough power to create the required pressure gradients for such jets. Two magnetic jet formation scenarios are commonly discussed: The Blandford-Znajek process (BZ, Blandford & Znajek, 1977) and the Blandford-Payne process (BP, Blandford & Payne, 1982). The BZ process assumes a

quickly rotating SMBH (with spin a) which is surrounded by an accretion disk. The sphere of its gravitational influence can be described by the radius $R_G = GM_{SMBH}c^{-2}$ with G denoting the gravitational constant and c is the speed of light. The required magnetic fields are supplied by the accretion disk, leading to the formation of a magnetosphere around the rotating SMBH, in turn enabling the formation of a plasma. The plasma is then accelerated due to the interaction of the SMBH with the magnetic field. This process extracts energy from the SMBH quite efficiently for highly magnetized accretion disks and high spin a, which has been shown by simulations by Tchekhovskoy et al. (2012).

On the other hand, the BP model suggests that magnetic field lines of the disk have a toroidal component due to rotations, which allows the extraction of plasma from the disk into a relativistic, magnetically driven wind (Li et al., 1992). Here, magnetic pressure results in the initial acceleration of the jet. In both processes, the accretion disk plays a vital role in jet formation. The dominant forces for accretion are gravity, pressure and rotation (Abramowicz & Fragile, 2013), as well as the geometry of the disk. Accretion disk can be grouped in *thin*, *slim*, *thick* and *advection dominated accretion flow* (ADAF) based on their disk height, accretion rate, optical depth, advection dominance, radiation pressure and accretion efficiency. Recent simulations suggest that thick disks with high spin SMBHs can produce jets via the BZ process if the disk is magnetized (Tchekhovskoy et al., 2012; McKinney et al., 2012). Also, the efficiency should depend on the orientation of the rotation of the accretion disk and the black hole. However, Tchekhovskoy & McKinney (2012) have shown in simulations that the efficiency can be the same for equal orientation (prograde black holes) and opposite orientation (retrograde black holes). A different characteristic to tell apart prograde and retrograde systems could be the *innermost stable circular orbit* (ISCO), which should range from $1R_G$ to $9R_G$ depending on the system. This could potentially be probed observational by high angular resolutions imaging techniques.

On a different note, gas dynamics describe the observations far from the core accurately. Models based on gas dynamics predict shock waves which explain the features of jet components in VLBI images. Kelvin-Helmholtz-instabilities can be observed as disturbances in expanding jets. The core is a special, stationary feature which signifies the point where the jet region changes from optically thick to optically thin ($\tau = 1$). It is thus frequency dependent following the relation $r_{core} \propto \nu^{-\frac{1}{k_r}}$ with the power index k_r (Sokolovsky et al., 2011; Lobanov, 1998). This effect is illustrated in Figure 1.2.

This phenomenon is known as *Core-Shift* and can not always be observed. On a closing note, both model types (based on magnetic field lines and gas dynamics) predict a gradual acceleration with an opening angle which is
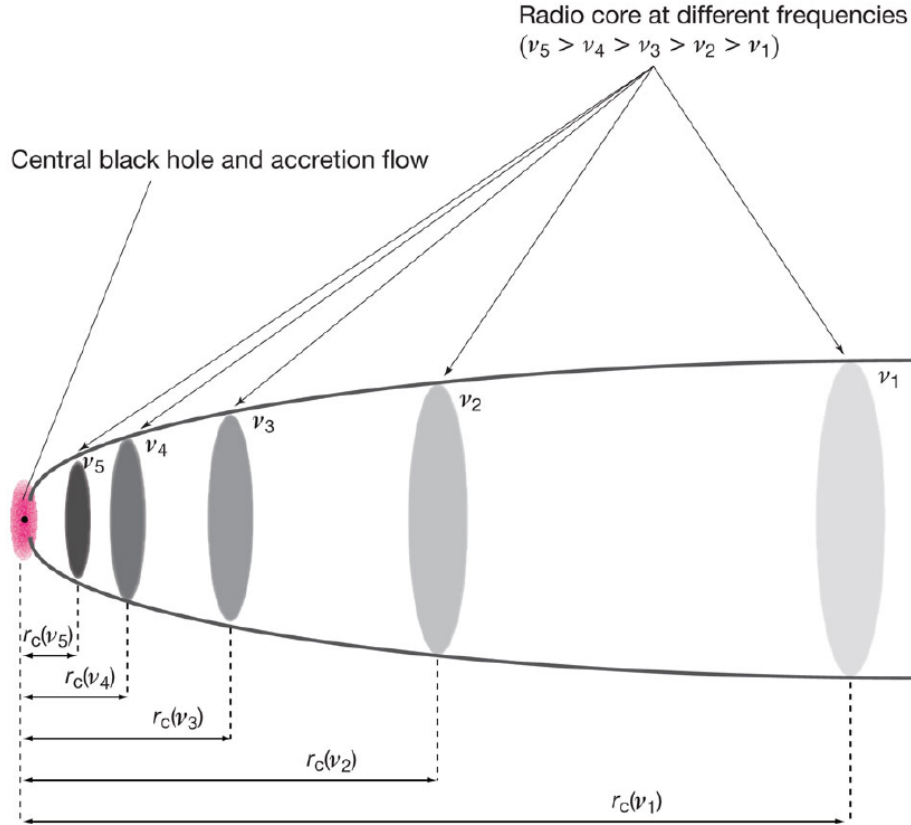
Figure 1.2: Illustration of the frequency dependence of the brightest component in VLBI images. The radio core shifts closer to the SMBH with increasing frequencies (Hada et al., 2011).

inversely proportional to the Lorentz factor. Thus, the highest intensity of observed emission is seen close to the core.

1.5 Broadband emission and variability

Active Galactic Nuclei are bright throughout the electromagnetic spectrum up to TeV energies (Dermer et al., 1992; Fossati et al., 1998; Ghisellini et al., 1998). Their broadband spectral energy distribution is made up of the superposition of the emission of all regions (accretion disk, dust torus, BLR, NLR, jet). The strength of the individual components may differ due to relativistic beaming effects (depending on the orientation of the inclination angle). Components in the vicinity of the SMBH remain spatially unresolved, despite the highest angular resolution of today's telescopes. However, spectral and temporal information help to shed light on the underlying structure.

Radio-loud AGN (especially blazars) feature a characteristic double-hump shape in their broadband energy distribution. Models can be distinguished in leptonic and lepto-hadronic models. Most models have in common that the low-frequency hump (from the radio to UV or X-ray regime) is attributed to synchrotron emission from the jet. The differences mainly regard the high-energy peak and the emission processes for this region are still under debate till this day.

Synchrotron emission (also called magnetobremsstrahlung) is the physical process of the radio emission, which was first established by Alfvén & Herlofson (1950). It explains the high degree of polarization from jets (Homan et al., 2002; Hovatta et al., 2010). Furthermore, it predicts the emission cone with an opening angle proportional to γ^{-1} accurately. The theoretical concepts behind synchrotron radiation will be discussed in Section 1.6.3.

Leptonic models suppose that the jet's emission is dominated by electrons and positrons which are accelerated and confined by a magnetic field. The high frequency emission is explained by inverse-Compton scattering of photons, which can originate from the jet itself or from external sources. These cases are referred to as *Synchrotron Self-Compton* (SSC, Bloom & Marscher, 1996) and *external Compton* (EC). In case of the EC model, seed photons may originate for instance from the accretion disk (Dermer et al., 1992), the broad-line region (Sikora et al., 1994), but also from the dusty torus (Błażejowski et al., 2000) or the cosmic microwave background (Georganopoulos et al., 2006). The inverse-Compton effect is characterized by low energy photons being upscattered by relativistic electrons. This effect is most relevant in astronomical sources which produce an abundance of hot electron gas (like the vicinity of a SMBH). The resulting spectral shape can be approximated by a power law with an exponential cut-off (Dermer & Schlickeiser, 1993). In the process, electrons lose energy ("Compton-loss") which leads to the so-called *Compton catastrophe*, a rapid down-cooling of the electrons (Kellermann & Pauliny-Toth, 1969). The strong cooling conditions a theoretical limit to the maximum brightness temperature of $T_B \sim 10^{12}\,\mathrm{K}$ of jets. However, this value changes for proton jets and non-equipartition jets (Singal, 2009; Kellermann, 2002). Relativistic jets are also promising candidates for ultra-high-energy cosmic rays (UHE-CRs) with energies greater than $10^{18}\,\mathrm{eV}$. Lepto-hadronic models require a significant contribution of protons in the jet. Proton-proton interaction then leads to pion and gamma-ray photon production. Pions in turn can further decay into muons and neutrinos. The latter may be detected, for instance by the IceCube Neutrino Observatory. Since only hadronic models are capable of producing neutrinos, the detection of the latter would be a strong hint towards those models (Mannheim, 1995; Stecker, 2013). The location of the high energy emission is also attractive for multi-wavelength studies. Comparing different models is made more complicated by the supposed geometry of the emission regions. The single-zone emission model is usually not sufficient to describe

the SEDs of blazars (Giommi et al., 2012). In this model, the emission region is assumed to be spherical with a given radius R moving relativistically with a Doppler factor $\delta = [\Gamma (1 - \beta \cos \theta)]^{-1}$. Single-zone models often require large Doppler factors, which is not backed by values found in very long baseline interferometry (Mankuzhiyil et al., 2011; Piner et al., 2010). Thus, more complex models have been proposed. Multi-zone models address these issues. Examples for these include the two-zone model (Abdo et al., 2011), the two-flow model or the spine-sheath model. In the latter, the jet is modeled by a fast moving spine surrounded by a slower layer. For this scenario, the TeV radiation is accounted for by the outer layer while the debeamed spine accounts for the radio to GeV emission (Tavecchio & Ghisellini, 2008). All things considered, fitting SEDs requires many parameters and comparing models statistically can prove difficult.

In radio-quiet sources, the emission from other components of the system become more important (dust torus, accretion disk, host galaxy). On a different note, blazars show high variability throughout the spectrum as well as correlations within different bands. This manifests itself in both short variability timescales (hours to days) but also longer active phases (weeks to months), see Urry (1996). Notably, the flaring behavior is frequently accompanied with a change in the polarization angle, indicating highly ordered magnetic fields or jet ejection events (Abdo et al., 2010). Understanding the relationship between the bands is crucial in order to model the emission mechanisms accurately, giving strong incentive for VLBI observations in conjunction with multiwavelength campaigns.

1.6 Theoretical Background

1.6.1 Superluminal Motion

The first detection of superluminal motion in an AGN jet was in 1969 by Gubbay et al. Although the phenomenon seems puzzling at first, it can easily be explained by a projection effect via the constant speed of light. The phenomenon was found in many of the monitored extragalactic jets (Cohen et al., 1977), which can be interpreted as evidence for the highly relativistic nature of jets. The highest measured velocity to date was $\sim 50 \, c$.

Consider a bright, moving jet feature with the relativistic velocity $v \approx c$ along a jet, with angle φ to the line of sight(cf. Figure 1.3). Two distinct light signals from this feature are detected in order to determine the velocity. Assume that the signals were emitted at the times t and $t + \Delta t_{emit}$. The feature moves a certain distance towards the observer before the second signal is emitted, however the observed distance (due to the projection) reads $\Delta x = v \Delta t_{emit} \sin \varphi$. Furthermore, the observer detects the signals separated by the time delay $\Delta t_{obs} = (1 - \frac{v}{c} \cos \varphi) \Delta t_{emit}$. Thus, the resulting
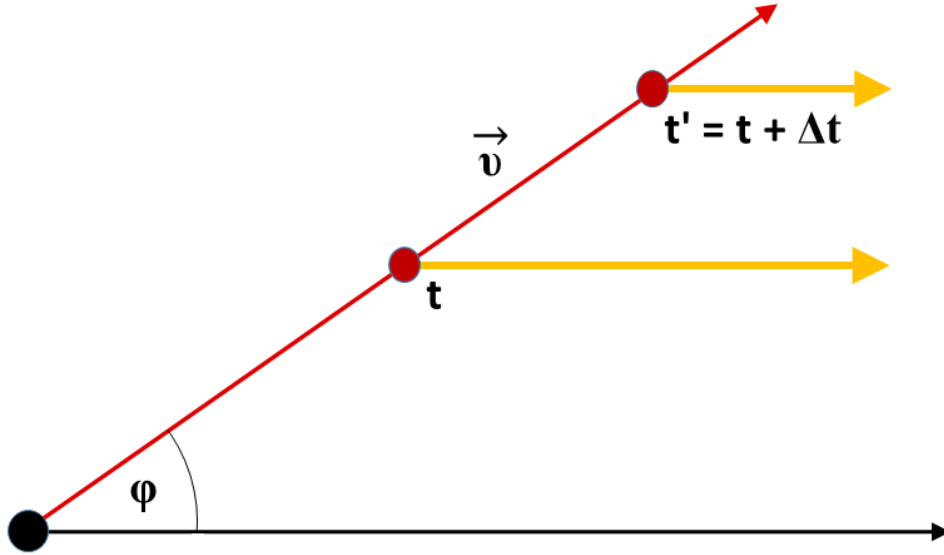
Figure 1.3: Sketch illustrative to the projection effect of superluminal motion. The bright feature propagates towards the observer with velocity v at an angle φ. Successive signals detected by the observer yield apparent speeds greater than the speed of light. Those apparent velocities strongly depend on the jet inclination angle.

observed velocity reads

$$v_{app} = \frac{v \sin \varphi}{1 - \frac{v}{c} \cos \varphi}. \tag{1.1}$$

Clearly, the apparent velocity strongly depends on the jet inclination angle φ, for small values it can reach $v_{app} > c$. Figure 1.4 shows the observed velocity as a function of inclination angle for different values of β. For relativistic jet features with a small inclination angle, superluminal observed velocities are to be expected.

1.6.2 Doppler Boosting

Doppler boosting is the effect of increased/decreased observed flux density due to the emission of a feature which is approaching/receding at relativistic speed on a path close to the line of sight. This is formally described by the Doppler-factor

$$D = \frac{\nu_{obs}}{\nu_{em}} = \frac{\sqrt{1 - \beta}}{1 - \beta \cos \varphi} = \frac{1}{\gamma(1 - \beta \cos \varphi)}. \tag{1.2}$$

The Doppler-factor strongly depends on the inclination angle. This is because spherical emission of a relativistic feature appears as a "boosting cone"
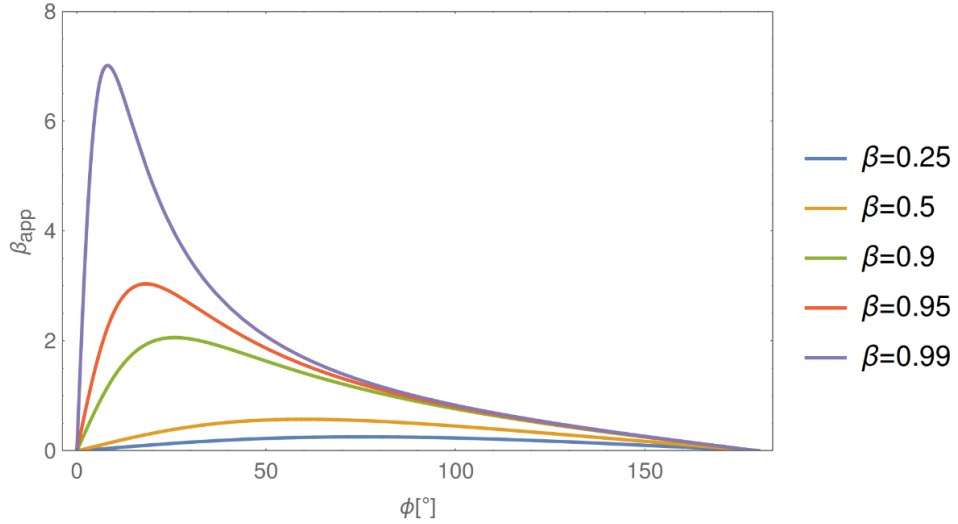
Figure 1.4: Apparent velocity β_{app} as a function of the inclination angle ϕ for a variety of intrinsic velocities β. The projection effect shows why highly relativistic jet features are observed with superluminal velocities.

with opening angle γ^{-1} in the laboratory system. Furthermore, it can be shown with the Lorentz invariant quantity $S_\nu \nu^{-3}$ (Rybicki & Lightman, 1979) that the observed intensity of a relativistically moving jet with power law spectrum ($S \sim \nu^\alpha$) is

$$S(\nu_{obs}) = D^{3-\alpha} S(\nu_{em}). \tag{1.3}$$

The angle has a prominent effect on the observed flux and spectrum because of the dependency of the flux on the frequency. This effect is clearly seen in VLBI images since one side of the jet is frequently missing. This results in the definition of the "counterjet". The flux ratio can be written as

$$R = \frac{S_{approach}}{S_{depart}} = \left(\frac{1 + \beta \cos \varphi}{1 - \beta \cos \varphi} \right)^{i-\alpha} \tag{1.4}$$

with $i = 2$ for a smooth jet and $i = 3$ for a spherical emission feature (Longair, 2011). This relation can be used to estimate the jet angle. Likewise, the flux of the counterjet can be estimated if the spectral index is known.

1.6.3   Emission processes in jets

For the low frequency emission in the radio, synchrotron radiation or *magnetobremsstrahlung* is very well-established. This proposition, which was first suggested by Alfvén & Herlofson (1950), explains the high degree of polarization which is typical for jets (Hovatta et al., 2010).

The important relations shall be presented here[1]. Please compare Rybicki & Lightman (1979) for detailed derivations of the formulae.

The origin of synchrotron emission are charged particles which are accelerated in a magnetic field (following classical electrodynamics). The result is polarized emission, with no emission in the direction of acceleration. In the non-relativistic case, this emission is known as *cyclotron radiation*. For the relativistic case, it is named *synchrotron radiation*. The Lorentz force can be written as

$$\frac{\mathrm{d}\vec{p}}{\mathrm{d}t} = \frac{e}{c}\vec{v} \times \vec{B} \tag{1.5}$$

with the particle momentum $\vec{p} = \gamma m_e \vec{v}$.

The resulting differential equation for the velocity

$$\frac{\mathrm{d}\vec{v}}{\mathrm{d}t} = \frac{e}{\gamma m_e c}\vec{v} \times \vec{B} \tag{1.6}$$

yields a helical motion with the frequency $\omega_B = \frac{eB}{\gamma m_e c}$. Here, $\gamma = \frac{1}{\sqrt{1-\beta^2}}$ is the Lorentz factor and $\beta = \frac{v}{c}$ is the ratio of the relative velocity to the speed of light. This frequency can also be expressed with the *Larmor frequency* and thus reads ω_L as $\omega_B = \frac{1}{\gamma}\frac{eB}{m_e c} = \frac{\omega_L}{\gamma}$. The power of this emission can be described using *Larmor's Formula*. This equation accounts for the emitted energy over an area $r^2 \mathrm{d}\Omega$ at an angle Θ with distance r. Here, q is a single charge, which is accelerated by $\boldsymbol{a}$ in an electric field:

$$\begin{aligned}
P &= \int_0^\infty \frac{q^2 a^2}{4\pi c^3} \sin^2\Theta \, \mathrm{d}\Omega \\
&= \frac{q^2 a^2}{4\pi c^3} \int_0^\pi 2\pi \sin^3\Theta \, \mathrm{d}\Theta \\
&= \frac{2q^2 a^2}{3c^3}
\end{aligned} \tag{1.7}$$

Under the assumption of an isotropic velocity distribution as well as relativistic electron speeds, the average emitted power can be worked out to

$$P_{em} = \frac{1}{6\pi}\beta^2\gamma^2 c\sigma_T B^2 \tag{1.8}$$

with the Thompson cross section $\sigma_T = \frac{8\pi e^2}{3m_e^2 c^4}$. Note that the power is proportional to the square of the particle energy $P_{em} \propto \gamma^2 \propto E^2$. Also note that the emitted power is inversely proportional to the particle mass $P_{em} \propto \sigma_T \propto m^{-2}$. This suggests that emission for massive particles is negligible in a first order approximation. In the particle rest frame, the radiation

---

[1]The derivation follows notes of *Extragalactic Jets*, a lecture held by M. Kadler at the JMU in the summer term of 2015.
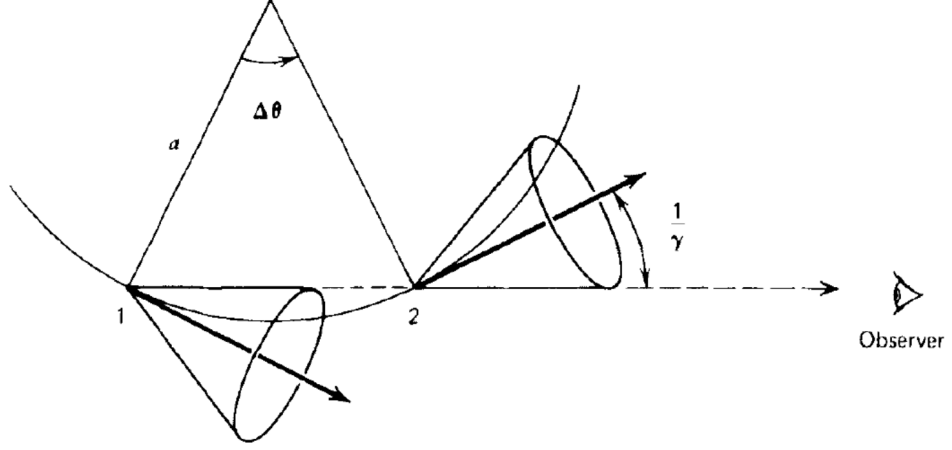
Figure 1.5: Emission cones along the trajectory of a particle in a magnetic field (taken from Rybicki & Lightman, 1979).

is characterized by dipole emission. However, due to relativistic beaming effects this is transformed to an emission cone with an opening angle proportional to $\frac{1}{\gamma}$. Due to the helical motion, the beam passes the line of sight in a limited time frame, leading to a short pulse.

In the electron rest frame, this time frame can be written as

$$
\begin{aligned}
\Delta t &= \frac{\Delta\theta}{\omega_B} \\
&= \frac{2}{\gamma} \cdot \frac{\gamma}{\omega_L} \\
&= \frac{2}{\omega_L}
\end{aligned}
\tag{1.9}
$$

using $\Delta\theta = \frac{2}{\gamma}$ from the geometry (cf. Figure 1.5). In the laboratory frame, this time interval is Doppler boosted and reads $\tau = (1 - \beta)\Delta t$. In the approximation of highly relativistic velocities $\beta \approx 1$, we find

$$
\begin{aligned}
\tau &= (1 - \beta)\Delta t \\
&= \frac{1 + \beta}{1 + \beta}(1 - \beta)\Delta t \\
&\approx \frac{1}{2}(1 - \beta^2)\Delta t \\
&= \frac{1}{\gamma^2 \omega_L}
\end{aligned}
\tag{1.10}
$$

Thus, the emission is governed by the characteristic frequency $\omega_c = \gamma^2 \omega_L$. Consider a distribution of electrons varying in γ. The resulting spectrum

can be obtained by integrating over the Lorentz factor:

$$P_\nu = \int_1^\infty P_\nu(\gamma) n(\gamma) \, d\gamma \tag{1.11}$$

Furthermore, let's consider the case of a power law distribution $n(\gamma) \, d\gamma = n_0 \gamma^{-p} \, d\gamma$. This is an important scenario which applies for synchrotron emission. In order to compute the resulting spectrum, the spectral shape $\phi_\nu(\gamma)$ has to be introduced:

$$\int \phi_\nu(\gamma) \, d\nu = 1 \tag{1.12}$$

Thus, the energy dependent emission reads

$$\begin{aligned} P_\nu(\gamma) &= \phi_\nu(\gamma) P_{em} \\ &= \frac{1}{6\pi} \beta^2 \gamma^2 c \sigma_T B^2 \phi_\nu(\gamma). \end{aligned} \tag{1.13}$$

The resulting integral can be solved under the assumption that all photons are emitted at the critical frequency ω_c, i.e. $\phi_\nu(\gamma) = \delta(\nu - \gamma^2 \nu_c)$. This is a good approximation, as the emission is strongly peaked around this frequency. For relativistic velocities $\beta \approx 1$, equation 1.13 can be written as:

$$\begin{aligned} P_\nu &= \int_1^\infty \frac{1}{6\pi} \beta^2 \gamma^2 c \sigma_T B^2 \delta(\nu - \gamma^2 \nu_c) n_0 \gamma^{-p} \, d\gamma \\ &= \frac{1}{12\pi} c \sigma_T n_0 \frac{B^2}{\nu_c} \left(\frac{\nu}{\nu_c} \right)^{-\frac{p-1}{2}} \end{aligned} \tag{1.14}$$

The important thing to note here is that a population of electrons distributed as a power law in energy, also yields a power law in its spectrum. The exponent $\alpha = \frac{1-p}{2}$ is named the *spectral index*. This relation governs the spectrum for larger frequencies in the *optically thin* or *transparent* regime. For lower frequencies in the *optically thick* or *opaque* regime, synchrotron self-absorption has to be considered. The optical depth τ is formally defined as $d\tau_\nu = \alpha_\nu \, ds$ or

$$\tau_\nu(s) = \int_{s_0}^s \alpha_\nu(s') \, ds' \tag{1.15}$$

along the path of light in the medium. In this context, α_ν is the absorption coefficient. The medium is considered optically thick for $\tau > 1$ and optically thin for $\tau < 1$, with $\tau = 1$ describing the turning point. In order to obtain the spectrum in the opaque case, the radiative transfer equations can be formulated in terms of τ and formally solved:

$$\frac{d I_\nu}{d\tau} = -I_\nu + S_\nu \tag{1.16}$$

$$I_\nu(\tau_\nu) = S_\nu + \exp^{-\tau_\nu} (I_\nu(0) - S_\nu) \tag{1.17}$$
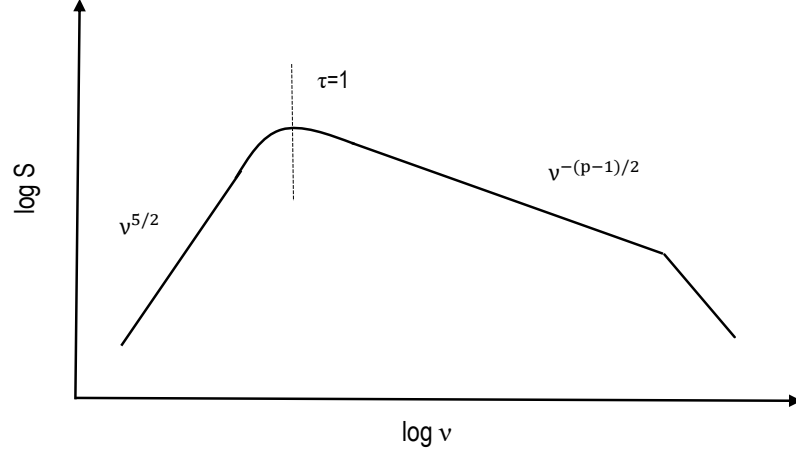
Figure 1.6: Overall spectral shape for a power law electron distribution in γ. The resulting spectrum is a broken power law, the spectral turnover at $\tau = 1$ is indicated.

For large values of τ, the intensity equals the source function S_ν, which is defined by $S_\nu = \frac{j_\nu}{\alpha_\nu}$. The emission coefficient in the isotropic case is given by $j_\nu = \frac{P_\nu}{4\pi}$. It can be shown that the absorption coefficient for synchrotron self-absorption is proportional to $\alpha_{\nu,ss} \propto \nu^{-\frac{p+4}{2}}$. Thus, we find that

$$S_\nu \propto \frac{\nu^{-\frac{p-1}{2}}}{\nu^{-\frac{p+4}{2}}} = \nu^{\frac{5}{2}}. \tag{1.18}$$

The resulting spectral shape for a power law distribution of the form $n(\gamma)\, d\gamma = n_0 \gamma^{-p}\, d\gamma$ is shown in Figure 1.6. It should be noted that for very high frequencies, the spectrum steepens since the energy-loss is larger for very energetic electrons. The spectral turnover at $\tau = 1$ is indicated. Larger structures feature a low optical depth while smaller structures are usually optically thick. The frequency at the turnover is named turnover frequency ν_t. The position of the turnover frequency also relates to the size of the emission region.

Summarizing the results, we can describe the spectrum obtained for a power law distribution as follows:

$$P_\nu \propto \begin{cases} \nu^{\frac{5}{2}} & \text{for } \nu < \nu_t \\ \nu^{\frac{1-p}{2}} & \text{for } \nu > \nu_t \end{cases} \tag{1.19}$$

Chapter 2

Very Long Baseline Interferometry

One of the big selling points for modern radio astronomy is its unprecedented and unrivaled spatial resolution. Astronomical observations down to less than a milliarcsecond are possible which means that interesting objects like AGN can be investigated on the parsec-scale level. This way the innermost regions of AGN can be tested in order to gain insight about the jet physics at work. In this chapter, the fundamental principles of radio astronomy and interferometry shall be outlined. A more detailed treatise of the subject can be found in Burke & Graham-Smith (2010).

2.1   Radio observations

Radio telescopes are built as parabolic reflectors. They feature a parabolic "dish", a receiving device as well as a recording system. The resolution of such an antenna is given by its diffraction pattern. A basic approximation can be derived from the Rayleigh criterion:

$$sin(\alpha) \approx 1.22 \frac{\lambda}{D}. \tag{2.1}$$

Here, λ is the wavelength and D is the diameter of the parabolic antenna. The numerical factor 1.22 arises from the first zero point of the order-one Bessel function of the first kind, which is the solution for the intensity distribution of an incoming signal through a circular aperture. This approximation suggests that large dishes are required in order to break even with the resolution of optical astronomy, simply because of the wavelength of the radiation. In fact, modern radio telescopes are mainly gated in resolution by their weight since both the parabolic form of the dish and the stability

of the whole structure is compromised above a certain diameter[1]. Due to the time invariance in Maxwell's equations, the antenna can be used both for emitting and detecting. Therefore, the radiation pattern ("beam") also characterizes the angular resolution, which is given by the main lobe. Side lobes are local maxima in the radiation signal strength in generally undesirable directions. The reception pattern is given by the Fourier transform of the aperture distribution. Incoming radiation is typically detected by a waveguide horn and subsequently converted into an electrical signal, which is then read out. The output signal T_A (antenna temperature) is the temperature of a hypothetical resistor that would generate the same power density per frequency bandwidth.

With few exceptions, single dish observations do not have the necessary resolution to resolve most astronomical sources spatially and are thus mainly used to measure the overall emission of a source (in order to obtain a spectrum or a light curve). Interferometry can be used to increase the resolution. Multiple telescopes act as one big telescope which is characterized by the baselines between the individual stations. The resulting resolution of the array is then formally defined as the half power width of the "synthesized beam" (the reception pattern of the array) and depends on the longest baseline in the form

$$\theta_{HPBW} \approx \frac{\lambda}{b_{max}}. \tag{2.2}$$

One prominent example of a radio interferometer is the *Karl G. Jansky Very Large Array* (VLA) on the plane of San Agustin, New Mexico. The VLA features 27 physically relocatable antennas in a Y-shaped configuration with a maximum baseline of 36 km.

The case of unconnected stations with baselines of tens to thousands of kilometers is referred to as *Very Long Baseline Interferometry* (VLBI).

2.2   Two-element interferometer

Modern telescope arrays used for interferometry feature many stations, however the basic ideas can be illustrated in the case of a two-element interferometer. An sketch is shown in figure 2.1.

The underlying assumption is that of an infinitely distant source with a flat spectrum in the observed bandwidth, ensuring a coherent incoming wavefront. In order to obtain a high resolution, the geometric time delay τ_g between the arrival of the wavefront at the two dishes has to be measured accurately.

$$\tau_g = \frac{b}{c} sin(\theta) \tag{2.3}$$

---

[1]Immovable telescopes reach values of $\approx 500\,m$ (FAST; Pingtang, China) while steerable ones feature diameters of up to $\approx 100\,m$ (Green Bank Telescope; Virgina, USA as well the Effelsberg 100-m Radio Telescope)
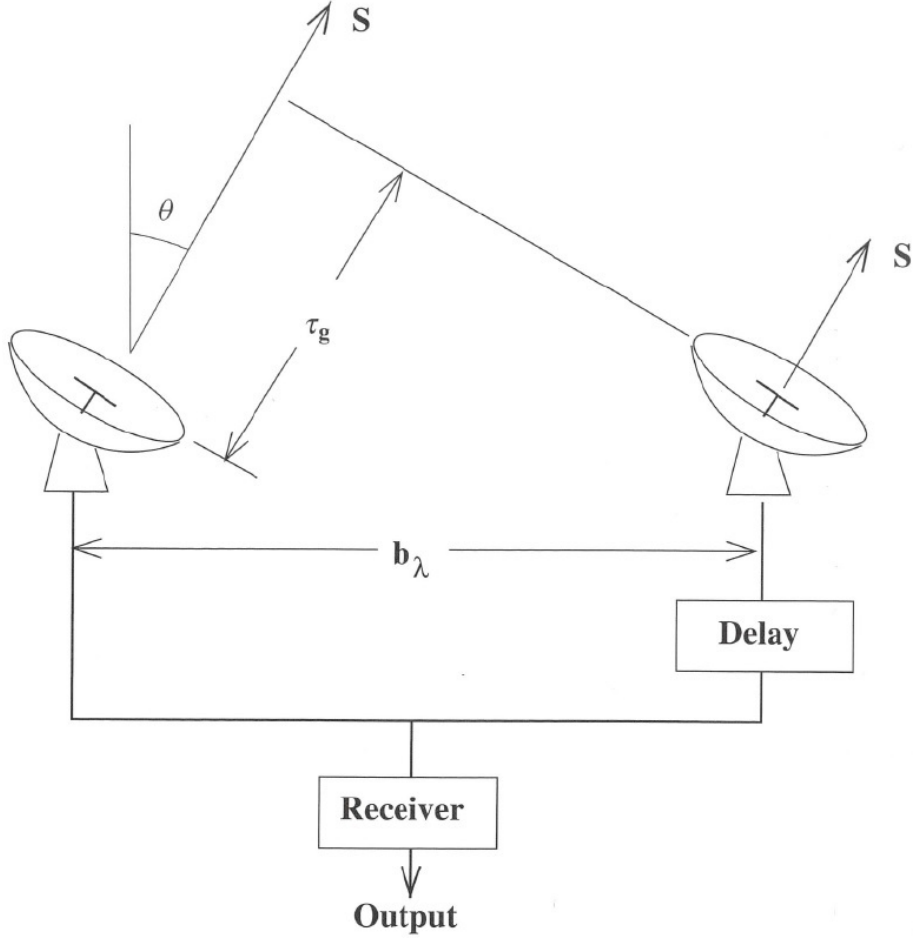
Figure 2.1: The characteristic geometry of the two element interferometer introduces the angle dependent geometric time delay τ_g. The delay circuit can introduce an additional time delay τ_i in order to compensate accordingly (Burke & Graham-Smith, 2010).

Here, b is the baseline, i.e. the distance between the two stations, c is the speed of light and θ describes the angle between the baseline vector and the vector pointing at the source $\vec{s}$. In order to measure this time delay, the stations are equipped with atomic clocks. Both stations log amplitude, phase and the corresponding time delay. This data is later processed by a correlator. The result of this time-averaged product is called *cross power product* R_{xy}

$$R_{xy}(\tau_g) = A(\vec{s}) \cdot S \cdot cos(2\pi\tau_g\nu) = A(\vec{s}) \cdot S \cdot cos\left(\frac{2\pi\,\nu b\sin(\theta)}{c}\right) \qquad (2.4)$$

which is also a function of the source flux S and the effective area $A(\vec{s})$.
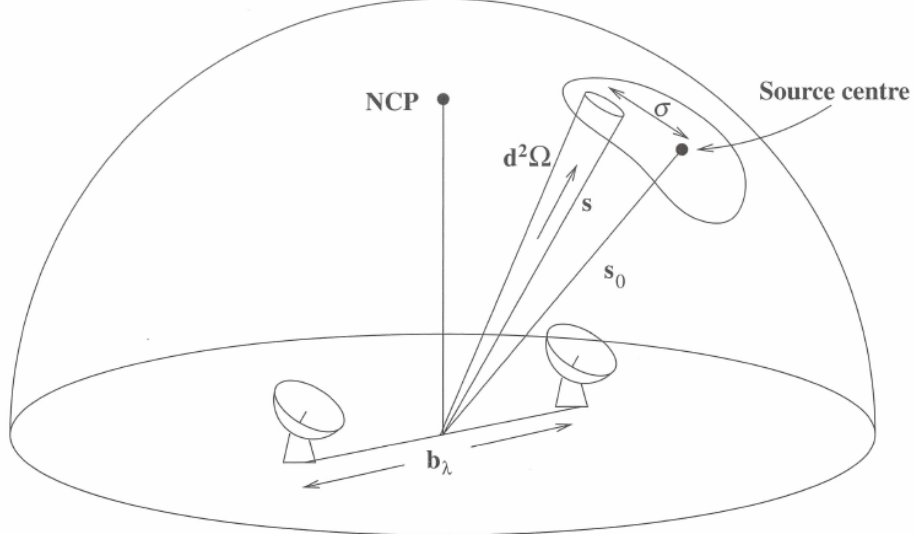
Figure 2.2: Sketch illustrating the phase-tracking center $\vec{s}_0$ and the displacement vector $\vec{\sigma}$. NCP denotes the North Celestial Pole (Burke & Graham-Smith, 2010).

The geometrical delay can be compensated by a time delay τ_i introduced by the correlator. Then, the *phase-tracking center* $\vec{s}_0$ can be defined, which is a reference vector pointing at a location very close to the source, formally defined by

$$\vec{s} = \vec{s}_0 + \vec{\sigma}. \tag{2.5}$$

Thus, $\vec{\sigma}$ describes the displacement of the source from this vector. Figure 2.2 shows a sketch of the setup, which also illustrates that $\vec{\sigma}$ is chosen to be orthogonal to $\vec{s}_0$. The observed visibility can then be written as

$$V_{i,j} = \int A_{\text{eff}} B_\nu(\sigma) \exp(i2\pi\vec{\sigma}\vec{b}_{i,j}) \, \mathrm{d}\Omega \tag{2.6}$$

as an integration over the brightness distribution on the sky B_ν over the solid angle $\mathrm{d}\Omega$. This complex visibility function is sampled over multiple baselines denoted by i, j. It should be emphasized that the effective area reflects the reception of the instrument, i.e. the synthesized beam of the telescope array. This means that the observable is a convolution between this beam and the source's brightness distribution. This is showing in equation 2.6 as the convolution of two quantities is equal to their product in the Fourier space according to the convolution theorem. A more convenient coordinate system can be chosen here. A right-handed rectilinear coordinate system (u, v, w) is used which features the spatial frequencies $u = \nu b \cos(\theta)$ and $v = \nu b \sin(\theta)$ in units of the observed wavelength. In this system, w is collinear to $\vec{s}_0$ and
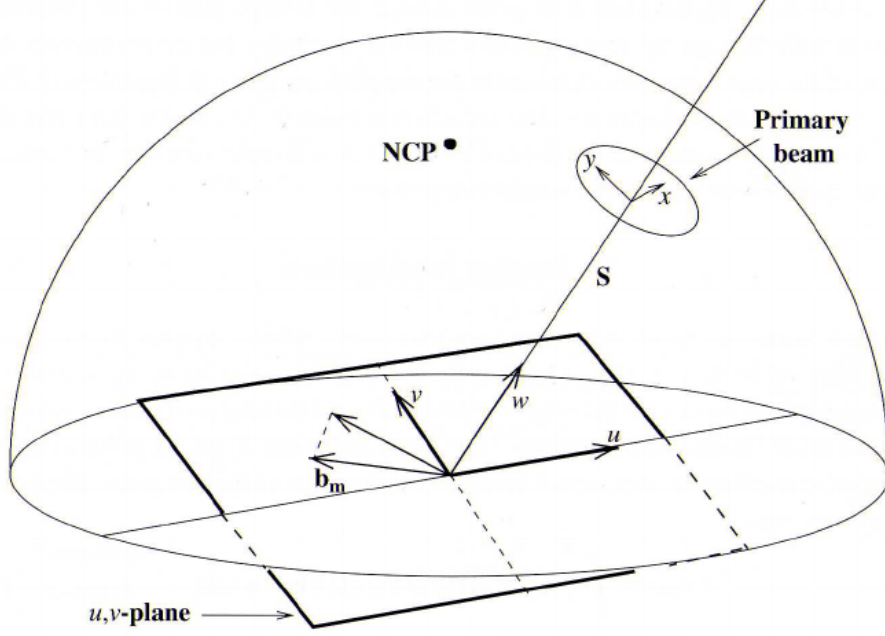
Figure 2.3: Sketch of the new coordinates (u, v, w) in relation to the interferometer and the source (Burke & Graham-Smith, 2010).

perpendicular to the so called (u, v) plane, which is parallel to both the baseline and σ. Under the assumption that the displacement σ is small, the visibility function can be expressed as

$$V(u,v) = \int \int_{-\infty}^{\infty} A_{\text{eff}}(x,y) B_\nu(x,y) \exp(i2\pi(ux + vy)) \, \mathrm{d}x\mathrm{d}y. \qquad (2.7)$$

The coordinates x and y form the plane in which the source is located, perpendicular main beam (compare figure 2.3). Reconstructing the true brightness distribution is an inversion problem which will be discussed in more detail in section 2.6. Equation 2.7 implies that the information gained about the source's brightness distribution corresponds to the coverage in the (u, v)-plane where one point represents one integration period (for a two-element interferometer). Additional telescopes naturally offer more baselines and thus a better coverage of the (u, v)-plane. The coverage is improved even further by a technique named *earth rotation synthesis*. This method takes advantage of the fact that the (u, v)-coverage depends on the projected baseline vector. Since the array tracks the source during extended observations, the angle towards the source changes. As a result, the baseline vector is time-dependent which leads to a denser coverage in the (u, v)-plane. Nevertheless, a full sampling in the Fourier domain is impossible. Gaps in the coverage introduce unwanted components in the synthesized beam, i.e. arti-

facts. In order to achieve the best coverage, radio telescopes spread out over the globe can be used. Long baselines correspond to small spatial frequencies, i.e. they contribute to the highest resolution while smaller baselines help to image larger scale structure. This means that radio interferometers act as spatial filters. The concept of the (u, v)-coverage can be formally described by introducing a sampling function $W(u, v)$. Comparable to the effective area of a single reflector, this function reflect the limitations of reconstructing the true brightness distribution induced by the concrete setup of the telescope array:

$$V_{\mathrm{measured}}(u, v) = W(u, v)w(u, v)V(u, v) \tag{2.8}$$

The response of the array V_{measured} can be further edited by adding the weighting factor $w(u, v)$. Depending on the scale of the structure of interest, longer or shorter spatial frequencies may be weighted more or less. For instance, *Uniform Weighting* yields the highest angular resolution at the cost of a higher noise level while *Natural Weighting* offers the best point source sensitivity.

2.3   Particularities of the VLBI technique

Interferometric techniques are applied on multiple scales. While telescopes are still connected in arrays like the VLA, this is not the case for *Very Long Baseline Interferometry*. Here, telescopes operate completely independently and only afterwards the data is shipped to the correlator. In principle, baselines are merely limited by the diameter of the earth for grounded operation. For space VLBI, even higher baselines are possible[2]. However, the separation of the stations also poses unique problems. As already mentioned, an accurate clock is required at every telescope. Additionally, a good model of the location of each station is required in order to measure the baselines, and thus the geometric delay. Furthermore, the stations are no longer arranged in a single plane (compared to the two-element interferometer). Thus, the (u, v)-plane is now a projection of the three-dimensional distribution of the antennas. On a different note, the weather conditions faced during the observations may vary for each station. As a result, opacity effects have to be taken into account for the calibration of the phases. Also, telescope arrays need not necessarily be homogeneous concerning their electronic systems and clocks. Since the correlator cannot account for all of these, delay errors occur. The process of correcting for these errors is named *fringe fitting*, based on a global fringe fitting technique developed by Schwab & Cotton (1983). This technique is based on the concept of closure phases, which shall be covered in section 2.6.

---

[2]The RadioAstron mission offers baselines up to 300000 km

2.4   Existing telescope arrays

Various VLBI telescope arrays exist both on the northern hemisphere and the southern hemisphere some of which are specifically built for this purpose. One example is the *VLBA* (Very Long Baseline Array, Napier, 1995) with its ten 25 m radio antennas spread over the USA. Other surveys utilize existing telescope that sync up for jointed observation sessions. Notably, the *EVN* (European VLBI Network, Venturi, 2010) features excellent angular resolution. The aforementioned *JVLA* (Jansky Very Large Array, Perley et al., 2011) can be used both as an array and as a single antenna by phasing up all antennas and can even be included into other arrays as a result, greatly enhancing resolution. Potential partners are the VLBA or for instance, the *GMVA* (Global Millimeter VLBI Array, Krichbaum et al., 2008). On the Southern Hemisphere, the Australian *LBA* (Long Baseline Array Norris, 1988) consists of a flexible subset of antennas which was not initially built for VLBI. Instead, they take part in multiple programs, one of which is the TANAMI program which will be discussed in more detail later. In the realm of millimeter wavelengths, *ALMA* (Atacama Large Millimeter Array Wootten & Thompson, 2009) constitutes a new asset to radio astronomy with it unprecedented resolution at those wavelengths. Current surveys also include the MOJAVE program (Lister et al., 2009a), monitoring several hundred AGN in the northern hemisphere.

A natural step to further improve resolution is providing greater baselines by having radio telescopes in space dedicated to radio interferometry. Early advances on this territory were made by *HALCA* (Highly Advanced Laboratory for Communications and Astronomy Hirabayashi et al., 2000), a Japanese radio telescope satellite which was gathering data from 1997 to 2005. In recent years, the Russian scientific satellite Spektr-R, also known as RadioAstron, has been participating in arrays in conjunction with ground based antennas, promising baselines of up to 300000 km.

2.5   The TANAMI Project

TANAMI[3] (Tracking Active Galactic Nuclei With Austral Milliarcsecond Interferometry) is a VLBI monitoring program with the goal to study parsec-scale structures of jets on the Southern Hemisphere. It consists of a heterogeneous array of radio telescopes which were not initially designed to be used for VLBI. The program is supplemented with multiwavelength observations. One particular goal is to investigate the so called *radio-gamma-connection* seen in AGN jets (correspondence of high energy emission and changes in the parsec-scale jet properties) in order to find where X-rays and γ-rays are produced. This is also reflected in the choice of the source sample. Further-

---

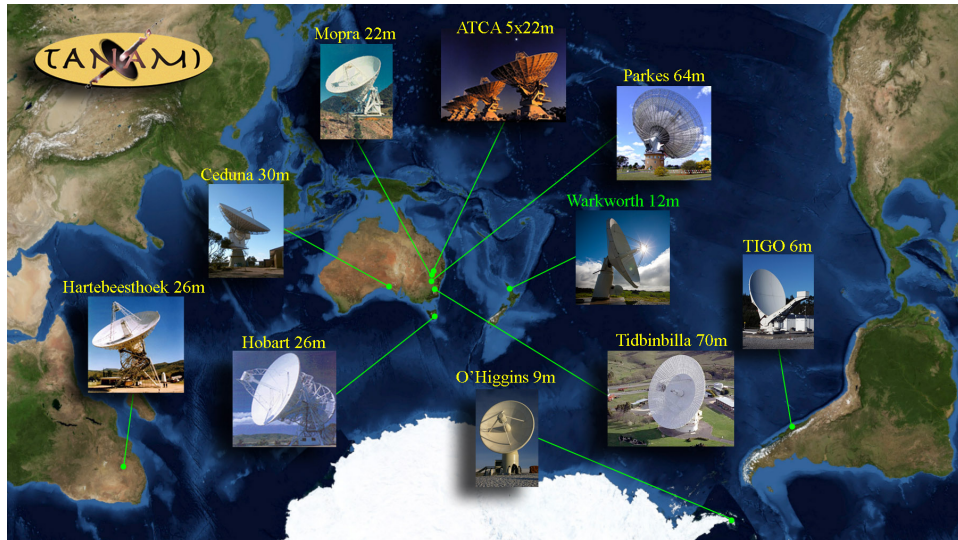[3]http://pulsar.sternwarte.uni-erlangen.de/tanami/

Figure 2.4: The TANAMI telescope array is spread out over the Southern Hemisphere (Credit: M. Kadler & J. Wilms). For a full list of participating telescopes, compare Table 2.1.

more, the emission and formation mechanisms of AGN jets are investigated. Observables include the jet properties, apparent speed, overall structure, changes with time (jet bends, knot ejection events), opening angles and the inclination of the jet. This structural information can be tested on its correlation with high energy flaring activity of the source. Additionally, the VLBI observations can be performed at 8.4 GHz and 22.3 GHz which can be used to obtain spatial spectral index distributions of individual jet features.

2.5.1   The TANAMI array

The TANAMI array includes the *Australian Long Baseline Array* (LBA) as well as the associated antennas Tidbinbilla (DSN 70 m or 34 m), joined by the South-African Hartebeeshoek antenna. Since 2009, the array is further augmented by the 9 m *German Arctic Receiving Station* (GARS) in O'Higgins/Antarctica and also the 6 m *Transportable Integrated Geodetic Observatory* (TIGO) in Chile. It should be noted that since 2014, the latter is operated in La Plata/Argentinia under the acronym *AGGO* (which stands for Argentinian-German Geodetic Observatory). Ever since 2011, further intermediate-length baselines are available due to the Warkworth, Katherine and Yarragadee antennas (located in New Zealand, northern Australia and western Australia respectively). Nevertheless, the uv-coverage for intermediate-length baselines is limited and special care has to be taken in calibration and the imaging process as a result (a typical uv-coverage is
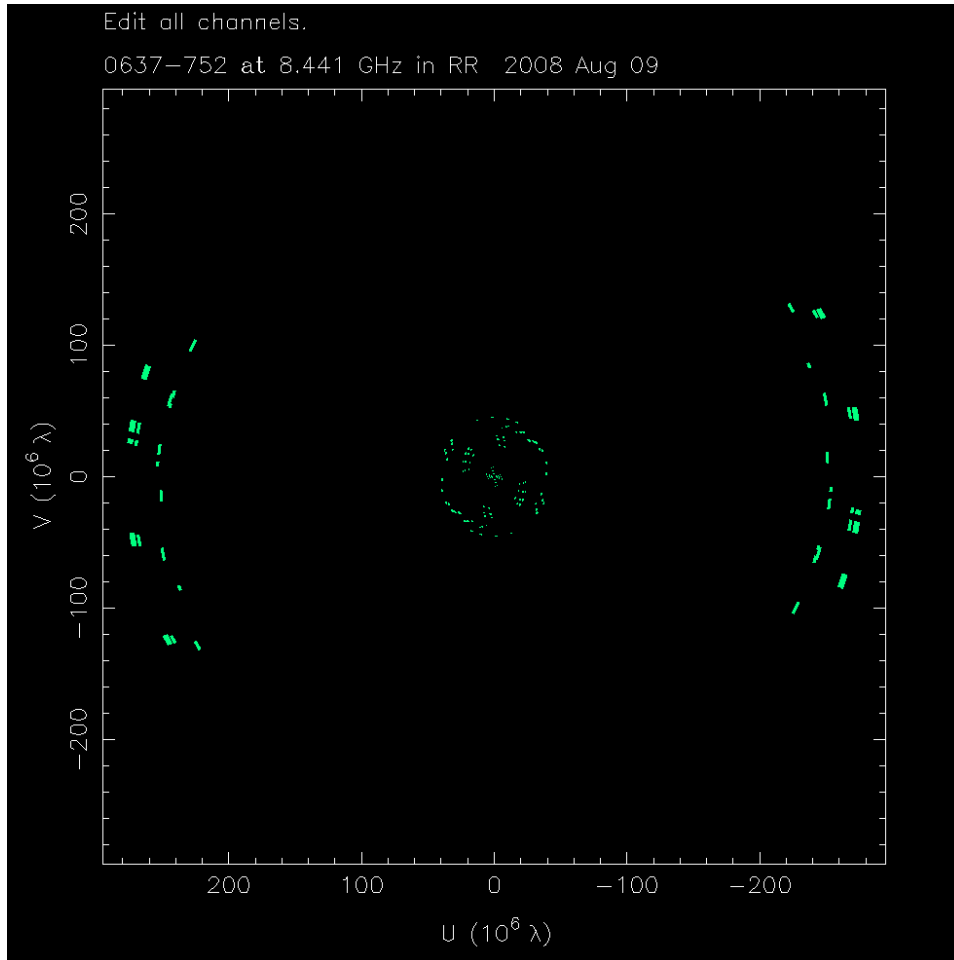
Figure 2.5: Typical (u,v)-plane coverage for a source in the TANAMI sample ([HB89] 0637-752) as seen in `DIFMAP`.

shown in figure 2.5).

The array is also joined by a single ASKAP antenna in western Australia (Kadler et al., 2015). The longest baselines, and as a result, the best resolution, is achieved in conjunction with the Hartebeeshoek, Tigo and O'Higgins antennas. Typical angular resolutions are in the magnitude of a few mas, in the best cases down to less than 1 mas. Table 2.1 summarizes the array configuration.

2.5.2   Data processing

Observations were initially performed twice per year since 2007. They are organized in so called *epochs*, which refers to a certain observation time/band. The data correlation is performed using the DiFX software correlator at

Table 2.1: Telescopes of the TANAMI array

Telescope	Diameter (meters)	Location
Parkes	64	Parkes, New South Wales, Australia
ATCA	5 x 22	Narrabri, New South Wales, Australia
Mopra	22	Coonabarabran, New South Wales, Australia
Hobart	26	Mt. Pleasant, Tasmania, Australia
Ceduna	30	Ceduna, South Australia
DSS43[a]	70	Tidbinbilla, Australia
DSS45[a]	34	Tidbinbilla, Australia
Hartebeesthoek[b]	26	Hartebeesthoek, South Africa
O'Higgins[c]	9	O'Higgins, Antarctica
TIGO[c]	6	Concepcion, Chile
Warkworth	12	Aukland, New Zealand
Katherine	12	Northern Territory, Australia
Yarragadee	12	Western Australia
ASKAP	36 x 12	Murchinson, Western Australia

Notes: [a] Operated by the Deep Space Network of the National Aeronautics and Space Administration.
[b] Not operational between Sept. 2008 and Sept. 2010 due to a major failure.
[c] Operated by the Bundesamt für Kartographie und Geodsie (BKG).

Curtin University in Perth, Western Australia (Deller et al., 2007). In the next step, an initial inspection and the fringe fitting process is done using *AIPS* (the National Radio Astronomy Observatory's Astronomical Image Processing System software, Fomalont, 1981). The amplitude calibration relies on known flux values of prior observed sources. The imaging process is performed in the program `DIFMAP` (Shepherd, 1997) using the `clean` algorithm as well as amplitude and self-calibration. This process will be illustrated in more detail in the following chapter.

As was already hinted, the VLBI monitoring program is supplemented by several associated multiwavelength observations which provide excellent NIR/optical/UV, X-ray and γ-ray coverage. Participating instruments include but are not limited to the *Fermi*/LAT-detector, the *X-ray Multi-Mirror Mission* (*XMM-Newton*) and the *Swift*-satellite for higher energies as well as the *Rapid Eye Mount* (REM) and the Gemini South Survey in the optical waveband.

2.5.3   Sample definition

Most of the selected sources have not been imaged on mas-scales yet. The initial sample was designed as a Southern Hemisphere extension of the *MO-JAVE* 1 sample (Lister et al., 2009a). It includes sources south of -30° declination. Part of the initially selected sources were chosen by a flux-density limit. Another fraction consists of γ-ray detected sources based on the results of CGRO/EGRET (Ojha et al., 2010). Later on, sources which were detected by *Fermi*/LAT were added to the sample, underlining the scientific goal of investigating the radio-gamma-connection. Currently, the TANAMI sample includes more than 80 sources.

2.6   Analyzing VLBI data in `DIFMAP`

After the data is calibrated in `AIPS` (Cotton, 1995; Diamond, 1995), it is stored in a uv-file in FITS format (Flexible Image Transport System, Wells et al., 1981). These files can be interactively edited and analyzed, using the hybrid mapping program `DIFMAP` (Shepherd, 1997). `DIFMAP` provides visualization of the data and model in multiple ways, including the residual map, which shows the difference between the data and the model (hence the name *difference mapping*). In an initial step, the data can be averaged since the error bars of calibrated data is rather high. The integration time is chosen within the coherence length of the data (for TANAMI data, an integration time of 32 s is applied). The aforementioned weighting method can be selected, as well as the map-/ and pixel-size. In an optional step, a taper can be introduced (for instance to down-weight longer baselines in order to improve sensitivity for extended emission).

2.6.1   The `clean` algorithm

As indicated by eq. 2.6, the amplitude and phase of $V_{i,j}$ are the observables in interferometry. They are related to the brightness distribution on the sky $B_\nu(\sigma)$ by a Fourier-transform relationship. Image reconstruction is thus a two step process: it involves the inverse Fourier transform of the complex visibilities and in a second step, the deconvolution of the synthesized beam and the intensity distribution of the source. This can be accomplished using the `clean` -algorithm, following the common procedure[4] (Högbom, 1974):

1. In the first step, (u,v)-data is interpolated to fit a regular grid, so that a *FFT* (Fast Fourier transform) can be applied on the gridded data. The result is the so-called *dirty image*. The latter is the convolution of the true image and the *dirty beam* (the point-spread function).

---

[4]based on instructions in *Modern astrophysics - Extragalactic jets*, a lecture held by M. Kadler at the JMU in the summer term of 2011.

2. The brightest pixel in the dirty image are identified (`DIFMAP` allows the selection of bright features using *windows*) and the dirty-beam response of a point source is subtracted. The subtracted point source model is saved in a new temporary map.

3. The dirty image (now called *residual map*) features new maxima. Repeating step 2 decreases their amplitudes until a weak noise background remains (the image is *cleaned*).

4. The developed clean model is convolved with a synthesized Gaussian beam (the *clean beam*), yielding the *clean image*. The residual map is added to the clean image.

2.6.2   Self-calibration and closure phases

Modern use includes a few alterations to this method. The modified method is known as *hybrid imaging* and involves self-calibration steps which are woven in the process. Self-calibration is based on closure relationships, which shall be outlined shortly. This step is necessary in cases where the relative phases of the signals are unknown, which is the case for VLBI where large differences in the transmission paths through atmosphere and ionosphere introduce phase errors. This means that the measured phase is given by

$$\phi_{i,j} = \phi_{0,i,j} + \Delta\phi_{i,j} = \phi_{0,i,j} + (\Theta_i + \Theta_j) \qquad (2.9)$$

with $\Theta_{i,j}$ describing phase errors associated with the respective stations. *Closure phases* $c_{i,j,k}$ are the sum of the observed phases of three telescopes (i,j,k). We find that the phase errors introduced by the individual stations cancel out (Walker, 1989):

$$\begin{aligned} c_{i,j,k} &= \phi_{0,i,j} + \phi_{0,j,k} + \phi_{0,k,i} + \Theta_i - \Theta_j + \Theta_j - \Theta_k + \Theta_k - \Theta_i \\ &= \phi_{0,i,j} + \phi_{0,j,k} + \phi_{0,k,i} \end{aligned} \qquad (2.10)$$

This means that the *closure phases* can be used as a conserved quantity that is independent of atmospheric errors for the purpose of phase self-calibration. Naturally, this method can only be used for data where three telescopes or more are available. The downside of this technique is that it is impossible to tell if one single phase error at one station or multiple errors are multiple stations are corrected in the process. This means that the information of the precise source position is lost. Since surveys like the TANAMI project are interested in structural information like the relative velocity of jet components, this is an acceptable drawback for the application. The same concept can also be applied to the amplitudes. The measured visibility amplitude $|V_{i,j}|$ is affected by gain errors $g_{i,j}$, i.e.

$$|V_{i,j}| = g_i g_j |V_{0,i,j}| \qquad (2.11)$$

A closure relationship for the amplitudes can be defined by utilizing four antennas (i, j, k, l) in the following way:

$$
\begin{aligned}
a_{i,j,k,l} &= \frac{|V_{i,j}||V_{k,l}|}{|V_{j,k}||V_{l,i}|} \\
&= \frac{g_i g_j |V_{0,i,j}| g_k g_l |V_{0,k,l}|}{g_j g_k |V_{0,j,k}| g_l g_i |V_{0,l,i}|} \\
&= \frac{|V_{0,i,j}||V_{0,k,l}|}{|V_{0,j,k}||V_{0,l,i}|}
\end{aligned}
\tag{2.12}
$$

While closure phases and closure amplitudes can be used with three or four antennas respectively, they are most effectively applied in large arrays (Kadler, 2011). *Hybrid imaging* introduces the following modifications to the procedure:

1. After the `clean` -algorithm is applied and a first model is obtained, a phase self-calibration is applied. The `clean` -selfcal cycle is repeated after no further improvement is possible.

2. In a second step, an amplitude self-calibration with a long solution interval is performed. This corrects for errors which are constant or only vary very slowly with time in the visibility amplitudes.

3. The corrected visibilities are used to obtain a new improved model using the `clean` -selfcal cycle. Subsequently, another amplitude self-calibration with a smaller time interval is performed.

4. This iterative process is repeated with incrementally decreasing time intervals for the amplitude self-calibration. The result is a self-consistent model that reproduces the calibrated data.

The final clean image can be used to identify components in the jet structure. In the next step, the point sources in the vicinity of these features are replaced by 2D Gaussian components. This is achieved using the `modelfit`-algorithm which utilizes a non-linear least squares minimization technique (Levenberg, 1944; Bevington & Robinson, 2003). Those model components are defined by their relative position, their integrated flux density as well as major and minor axis.

2.6.3 Statistical error evaluation

`DIFMAP` itself does not yield uncertainties for the model parameters which were derived during the imaging process. Thus, the *Interactive Spectral Interpretation System* (`ISIS` , Houck & Denicola, 2000) was used to determine parameter values and their uncertainties using χ^2 -statistics. Credit for the initial implementation of the `ISIS` -scripts is given to C. Großberger of the Dr. Remeis Observatory in Bamberg (details in Großberger, 2014).

Chapter 3

TANAMI VLBI observations

The sub-sample which was imaged in this thesis consists of five sources which were selected with potential kinematic studies in mind. Each source features at least seven observation epochs between March, 2008 and March, 2013. A detailed overview of the sample including information regarding source position, brightness and redshift is given in Table 3.1. A detailed overview of the observation epochs including information on the telescope configuration can be found in Table 3.2. In this chapter, previous results will be discussed and the imaging results will be presented. Multiple sources showed extended emission with cross-identifiable components. These sources were analyzed kinematically, which is detailed in Section 3.4.

Table 3.1: List of sources

Name	R.A.[a][b]	Dec.[a][b]	Redshift	Magnitude[b][c]	LAT
PKS B0637-752	$06^h35^m46.5^s$	$-75^d16^m17^s$	0.653	15.7	Y
PKS B0405-385	$04^h06^m59.0^s$	$-38^d26^m28^s$	1.285	18.0	Y
PKS B1144-379	$11^h47^m01.4^s$	$-38^d12^m11^s$	1.048	16.2	Y
PKS B2204-540	$22^h07^m43.7^s$	$-53^d46^m34^s$	1.206	17.7	Y
PKS B2355-534	$23^h57^m53.2^s$	$-53^d11^m14^s$	1.006	17.8	Y

Notes: [a] Right ascension and declination in J2000.0
[b] According to NED(NASA/IPAC Extragalactic Database)
[c] Optical magnitude

Table 3.2: List of epochs

Epoch (date)	Telescopes[a]	Sample
2008-02-07	PA-CATW104-MP-HO-CD-DSS43, HART	2355-534, 2204-540, 1144-379, 0405-385, 0637-752
2008-03-28	PA-CATW104-MP-HO-CD-DSS43-HART	1144-379, 0405-385, 0637-752
2008-06-09	PA-CATW109-MP-HO-CD-HART	2355-534, 2204-540
2008-08-08	PA-CATW104-MP-HO-CD-HART-DSS45	1144-379, 0405-385, 0637-752
2008-11-27	PA-CATW104-MP-HO-CD-OH-TC-DSS43	2355-534, 2204-540
2009-02-23	AT-CD-DSS34-DSS45-HO-MP-OH-PA-TC	0405-385, 0637-752
2009-02-27	AT-CD-DSS45-HO-MP-OH-PA-TC	1144-379
2009-09-06	AT-CD-HO-MP-PA-TC-TI	2355-534, 2204-540
2010-03-12	AT-CD-HO-MP-PA-TI	1144-379, 0405-385, 0637-752
2010-05-07	AT-CD-HO-MP-PA-TC-TI	2355-534, 2204-540
2010-10-28	AT-CD-DSS34-HH-HO-MP-PA-TC-DSS45	1144-379, 0405-385, 0637-752
2011-07-21	AT-CD-DSS45-DSS43-HH-HO-MP-PA-TC-WW	1144-379, 0405-385, 0637-752
2011-08-14	AT-CD-HH-HO-KE-MP-PA-TC-TI-YG	2355-534, 2204-540
2012-04-27	AK-AT-CD-HH-HO-MP-PA-TC-WW	1144-379, 0405-385, 0637-752
2012-09-16	AK-AT-CD-HH-HO-KE-PA-TC-TI	2355-534, 2204-540
2013-03-14	AK-AT-CD-HO-KE-PA-TC-TD-TI-WW	0637-752
2013-03-14[b]	AK-AT-CD-HO-KE-PA-TC-TD-TI-WW AK-AT-CD-HH-HO-KE-PA-TI-WW	0405-385

Notes: [a] Telescope abbreviations: Parkes (PA), ATCA (AT, CATW104, CATW109), Mopra (MP), Hobart (HO), Ceduna (CD), Hartebeesthoek (HART), O'Higgins (OH), TIGO (TC), Warkworth (WW), Katherine (KE), Yarragadee (YG), ASKAP(AK).
[b] For this observation, two sub-arrays were used.

3.1 Previous results

PKS 2204-540

PKS 2204-540 is a bright quasar located at a redshift of $z \approx 1.206$. It features a high polarization (Ricci et al., 2004). While not being detected by EGRET, it was seen by *Fermi*/LAT during the first three months of its all-sky survey (Abdo et al., 2009), in which it was classified as a FSRQ. First epoch images of this source at 8 GHz showed a high brightness temperature core and a short, possibly curved jet about 4 mas south and south-west of the core (Ojha et al., 2010). These results are consistent with preliminary results published by Müller et al. (2012) of a later epoch. The latter also published an image at 22 Ghz which shows structure to the south, but misses the extension to the south-west.

PKS 2355-534

The earliest measurements of the radio structure of PKS 2355-534 were performed at 4.85 GHz by Shen et al. (1998), yielding a distinct component from the core at a distance of 4.0 mas at a position angle of 235°. First epoch TANAMI images of this source reveal an extended jet structure to the south-west with at least two distinct components at a radius of 3.5 mas and 12 mas (Ojha et al., 2010). A 22 GHz image of this source also shows a close component in the south-west direction, however it misses the emission region further out (Müller et al., 2012). PKS 2355-534, which features a redshift of $z \approx 1.006$ is noted to be optically violent and has a high polarization (Impey & Tapia, 1988).

PKS 0637-752

The radio-loud source PKS 0637-752 is a bright quasar with a redshift of $z \approx 0.653$. The kiloparsec-scale structure of this source is known to feature a jet extending up to 10 arcsec to the west before bending to the north-west. In the east, a single hot-spot is detected at around 10 arcsec (Edwards et al., 2006). Early VLBI images also show a jet towards the west, following the morphology of the kpc-scale (Tingay et al., 1998). Notably, Edwards et al. (2006) observed superluminal motion of the jet components on parsec-scales. This source has also been extensively studied in the X-ray regime, being the first target observed by *Chandra*. Schwartz et al. (2000) found a 100 kpc X-ray jet which coincides with the radio morphology of the source. First epoch TANAMI images confirm this result by showing jet structure in the same orientation, with tapered images revealing jet emission extending beyond 50 mas from the core (Ojha et al., 2010).

PKS 0405-352

This source is a quasar with a redshift of $z \approx 1.285$. It was not seen by EGRET, however there is a low confidence detection by *Fermi*/LAT regarding this source location (Ojha et al., 2010). Previous VLBI observations show a compact structure, commonly associated with a weak extension to the west in the form of a component located at about $1 - 5$ mas (Zensus et al., 2002; Ojha et al., 2010).
PKS 0405-385 is most known for exhibiting violent variability on very short timescales of a few hours. Sources with this characteristic are called IDV (intraday variability) sources. The reason why these AGN are unusual is because their variability is commonly used to infer the brightness distribution of the source, as well as constrain the size of the source. However, theory dictates that for static radio sources, the brightness temperature has an upper limit due to inverse Compton scattering, effectively confining it to $T_B < 10^{12}$ K (Kellermann & Pauliny-Toth, 1969). Under the assumption

that the observed variability in IDV sources was intrinsic, they would violate
this upper limit. There are multiple ways to interpret such a variability. One
approach would be to assume intrinsic fluctuations and explain the unusual
brightness temperature in terms of beamed synchrotron emission. However,
this would imply bulk motion with unusually large Lorentz factors. In the
case of PKS 0405-385, such superluminal motion has not been found and
evidence suggest that this holds true for most IDV sources. Other poten-
tial explanations have been proposed, however Kedziora-Chudczer (2006)
established interstellar scintillations (ISS) as the explanation for IDV in this
source. ISS is an extrinsic interpretation of IDV: The variability is explained
by turbulent motion of a small-scale structure in the ionized interstellar
medium. This acts as a scattering screen for the radio flux of the target of
interest, thus explaining the observed variability. This effect depends on mul-
tiple parameters, including the compactness of the radio source, the distance
of the ionized scattering screen and the velocity of the medium relative to
the observer. Kedziora-Chudczer (2006) show that (a) the scintillating com-
ponent of PKS 0405-352 has to be very compact (i.e. $<5\,\mu$m) and (b) the
ionized screen responsible for the scattering has to be relatively close (about
$20\,$pc). However, there still remain questions unanswered, mainly related to
the episodic nature of the short term variability which does feature tran-
sient events in which there is no IDV. PKS 0405-385 is one of the strongest
sources showing intraday variability in the TANAMI sample.

PKS 1144-379

PKS 1144-379 is a highly variable radio source with a redshift of $z \approx 1.048$.
Nicolson et al. (1979) have identified this source as a BL Lac type object
based on its optical and infrared properties, featuring a featureless powerlaw
spectrum. Veron-Cetty & Veron (2006) however classify it as a quasar. Early
VLBI images show an unresolved core (Shen et al., 1997). On the other
hand, first epoch TANAMI results yield an extension to the south-east up
to $16\,$mas (Ojha et al., 2010). This source was not detected by EGRET,
but was observed by *Fermi*/LAT (Abdo et al., 2009). Turner et al. (2012)
label PKS 1144-379 *an extreme scintillator*, referencing its nature as an IDV
source like PKS 0405-352.

3.2   Data evaluation

This section explains why the imaging process for all data sets in this thesis
was prefaced with an initial *modelfit-selfcal* cycle.
Following routine imaging procedure, the data set is read into `DIFMAP` using
the *observe* command. Subsequently, the weighting and the polarization as
well as the map size is selected. In the next step, the data is averaged over
timescales of $32\,$s in order to improve the signal-to-noise ratio. I will argue

in this section that this step is actually premature. Instead, better results can be obtained by performing a phase self-calibration first, and averaging after.

In Figure 3.1a, an example for uncorrected, original data is shown (featuring PKS 0405-385 observed in V252H on the Hobart-Ceduna baseline). A comparison with the panel to its right (Figure 3.1b) illustrates the effect of a phase calibration. In DIFMAP, this is performed using the *selfcal* command without any arguments. The theoretical background behind this command is explained in Section 2.6. *selfcal* is not the only command to perform a phase calibration. In order to obtain the plots in Figure 3.1b, 3.1c and 3.1d, the *startmod* command was used instead. This command reads in a 1 Jy point source as a starting model and phase self-calibrates against it, which for most sources is a reasonable first approximation to start with. The top panel illustrates that after the phase calibration, delays are corrected and phases appear flat around zero.

The two plots on the bottom show the data after averaging over 32 s. Figure 3.1d represents the ideal procedure: first a phase self-calibration was applied using the *startmod* command, and afterwards the data was averaged using the *uvaver* command. In order to draw a fair comparison, the data in the plot on the left (Figure 3.1c) was phase calibrated as well, but only after the data was averaged. It is quite noticeable that the phases on the far-right plot are smoother still. However, the important point addresses the amplitudes. Unlike *startmod*, *uvaver* is a command that has both phases and amplitudes as arguments and results. Thus, different starting phases also yield different amplitudes, which is evident in the difference in amplitudes in the plots. This can prove problematic in the imaging process as extended structures can easily be misinterpreted as an amplitude error, and vice versa. Using phase calibration before averaging makes use of the fact that the phase closure relationship is independent of the errors introduced by the atmosphere and ionosphere. As a result, propagation of these errors to amplitude errors in the averaging process is avoided. The plots illustrates the effect for one specific baseline, although it does appear in all baselines to varying extend. The alteration in amplitude depends on the original phase data: if phases are rather flat to begin with, the effect is much less pronounced.

For this thesis, one further (minor) improvement was applied to this procedure: rather than relying on the 1 Jy point-source approximation of the *startmod* command, a Gaussian component was fitted to the data using the *modelfit* algorithm, followed by a phase self-calibration using the *selfcal* command - and only after that, the data was averaged.
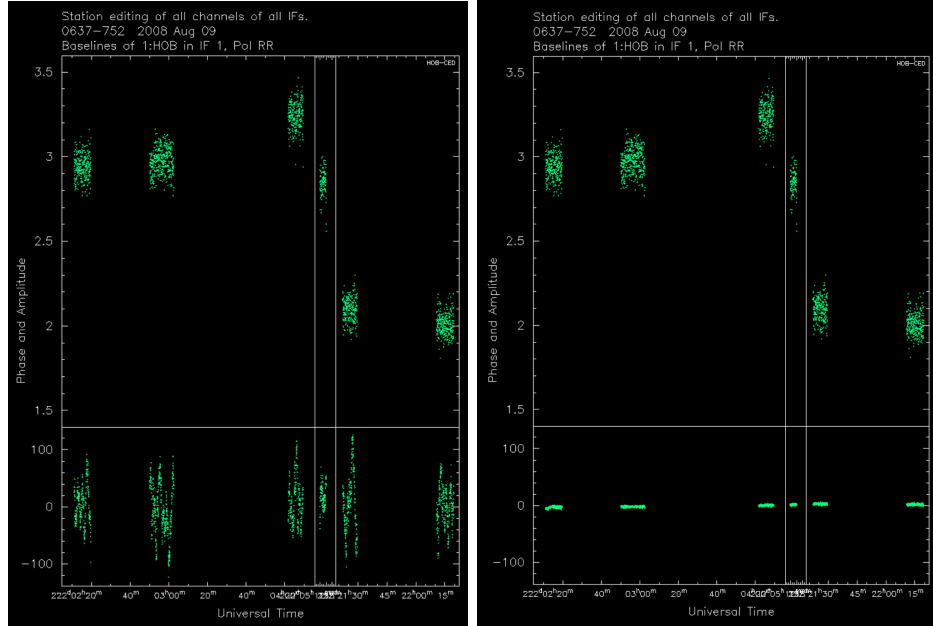
(a) Original data

(b) After phase calibration
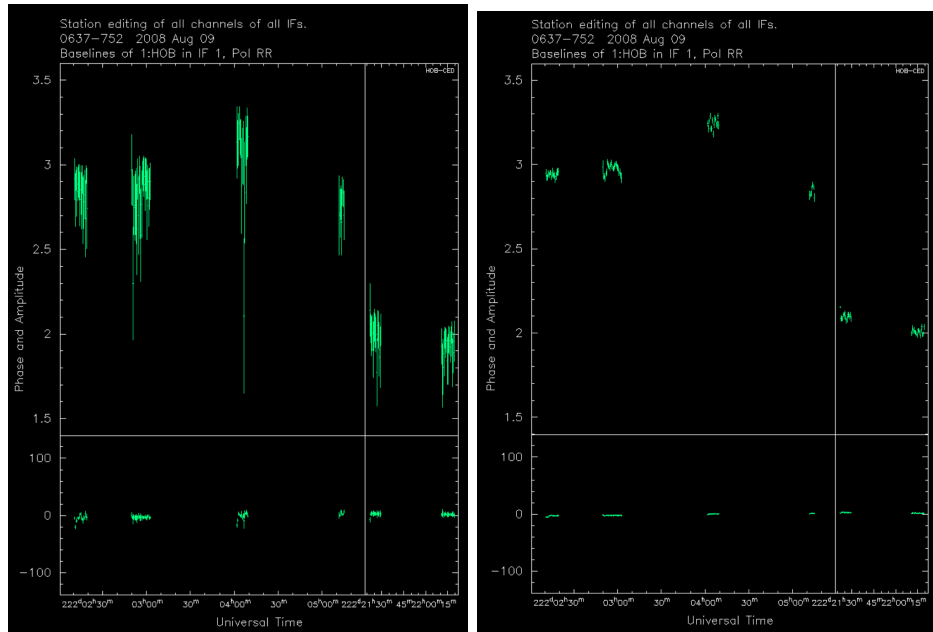
(c) After averaging, followed by phase calibration

(d) After phase calibration, followed by averaging

Figure 3.1: Evaluation of different approaches to the averaging process. Depicted are phases and amplitudes of PKS 0637-752 plotted against time on the Hobart-Ceduna baseline. Figures 3.1a and 3.1b show the influence of phase calibration on the data itself. Figures 3.1c and 3.1d show that phase calibration and averaging are not commutative.

3.3   Discussion of the imaging results

This section discusses the imaging process with its peculiarities for each source. Furthermore, the results are presented and discussed in the form of the clean images as well as the imaging parameters in the context of previous results. The kinematic analysis will be discussed subsequently in Section 3.4.

PKS 2204-540

The clean images of PKS 2204-540 are shown in Figure 3.2. This source's morphology is consistent with previously published VLBI images. The epoch V252I (dated 2008-11-27) was previously imaged and published (Müller et al., 2012), showing similar structure with a bright core and an extension to the south south-west. The first epoch V252C (dated 2008-02-07) was one of the first images published in (Ojha et al., 2010), also showing an extension to the south-west, but missing structure in the same direction at around 8 mas from the phase center. However, emission this far out only appeared in this epoch and V252R (dated 2009-09-05). Considering this cross-epoch information, the emission was not considered believable enough in order to be modelfitted for the kinematic analysis. The imaging parameters for all sources can be found in Appendix A, specifically in Table A.1 for PKS 2204-540. The total flux of this source follows a steady decrease in the early epochs, only to flare in V252AA (dated 2011-08-13), more than doubling its emission compared to the previous epoch in the process. In comparison to the mean flux over the whole observation period, this outburst at 1.44 Jy is statistically significant with conservative estimates for uncertainties of around 15 % to 20 % (this error refers to a random component in a random epoch and thus represents an upper limit for the uncertainty of the flux, Ojha et al., 2010). It is evident that by 2012-09-15, the radio flux has returned to a lower level, which means that this observation represents a flaring event rather than a transition to a long-term state with higher emission. Due to the sampling, it is not possible to constrain the timing of the flaring event effectively since V252AA is the only data point in the time frame given by the adjacent epochs which spans over more than two years (V252R was taken on 2010-05-07 while V252AE was taken on 2012-09-15). With the given information, the peak flux from this event might very well have been higher than 1.44 Jy. While this topic will be further addressed in the kinematic analysis, this event is at least not obviously coupled with any drastic change in the morphology of the source, e.g. a new component.

PKS 2355-534

This source features a clear jet structure towards the south-west, as shown in Figure 3.3. Again, the V252C (dated 2008-02-27) epoch yields the same
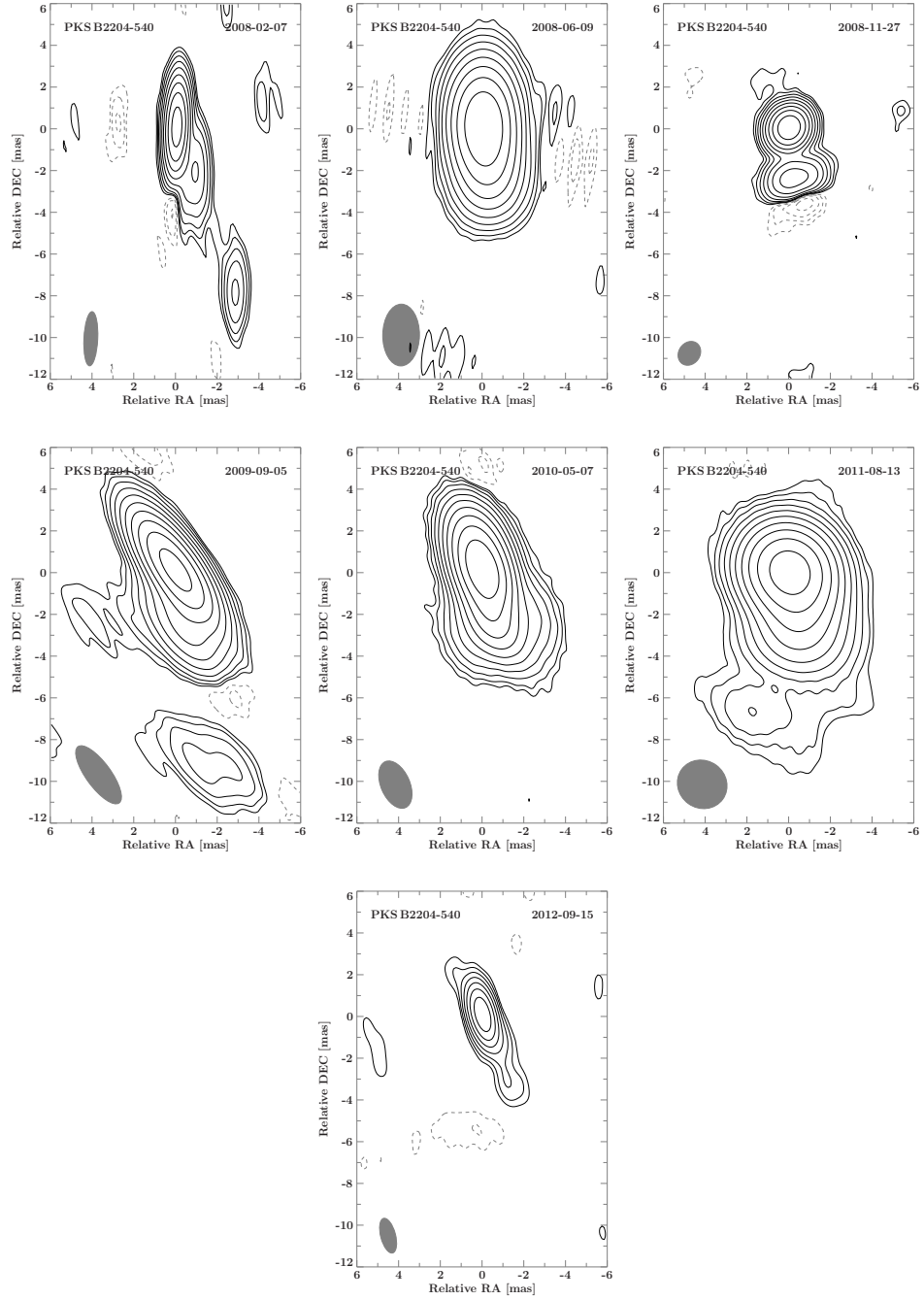
Figure 3.2: Clean images of 2204-540 in 7 observation epochs from 2008 to 2012. The contours show the flux density level, scaling logarithmically by a factor of 2 and starting at $3\,\sigma$ noise level for the first contour. The gray ellipse represents the synthesized beam.
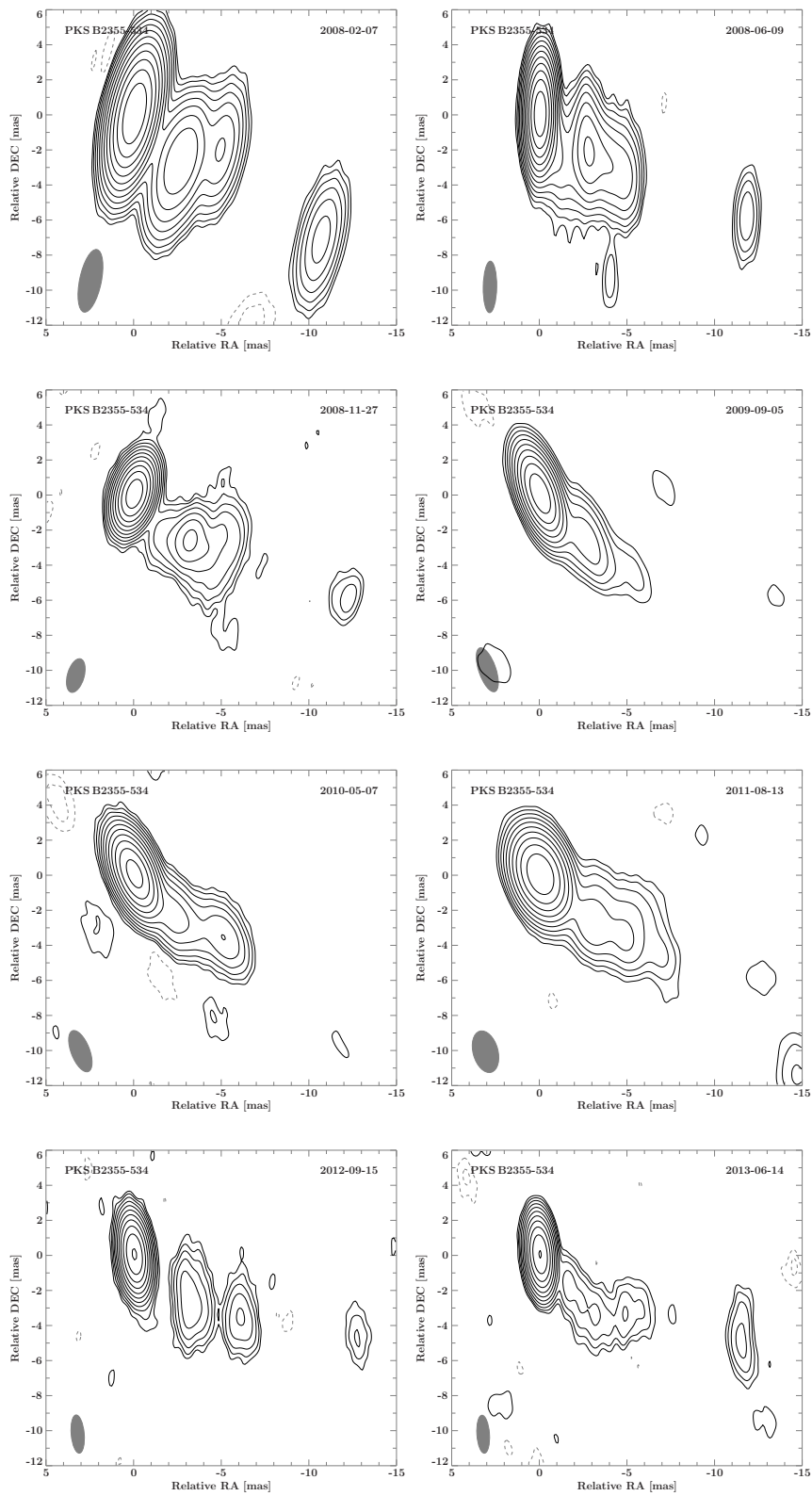
Figure 3.3: Clean images of 2355-534 in eight observation epochs from 2008 to 2013. The contours show the flux density level, scaling logarithmically by a factor of 2 and starting at 3σ noise level for the first contour. The gray ellipse represents the beam.

Figure 3.4: Clean images of 0637-752 in nine observation epochs from 2008 to 2013. The contours show the flux density level, scaling logarithmically by a factor of 2 and starting at $3\,\sigma$ noise level for the first contour. The gray ellipse represents the beam.

Figure 3.5: Clean images of 1144-379 in eight observation epochs from 2008 to 2013. The contours show the flux density level, scaling logarithmically by a factor of 2 and starting at 3σ noise level for the first contour. The gray ellipse represents the beam.
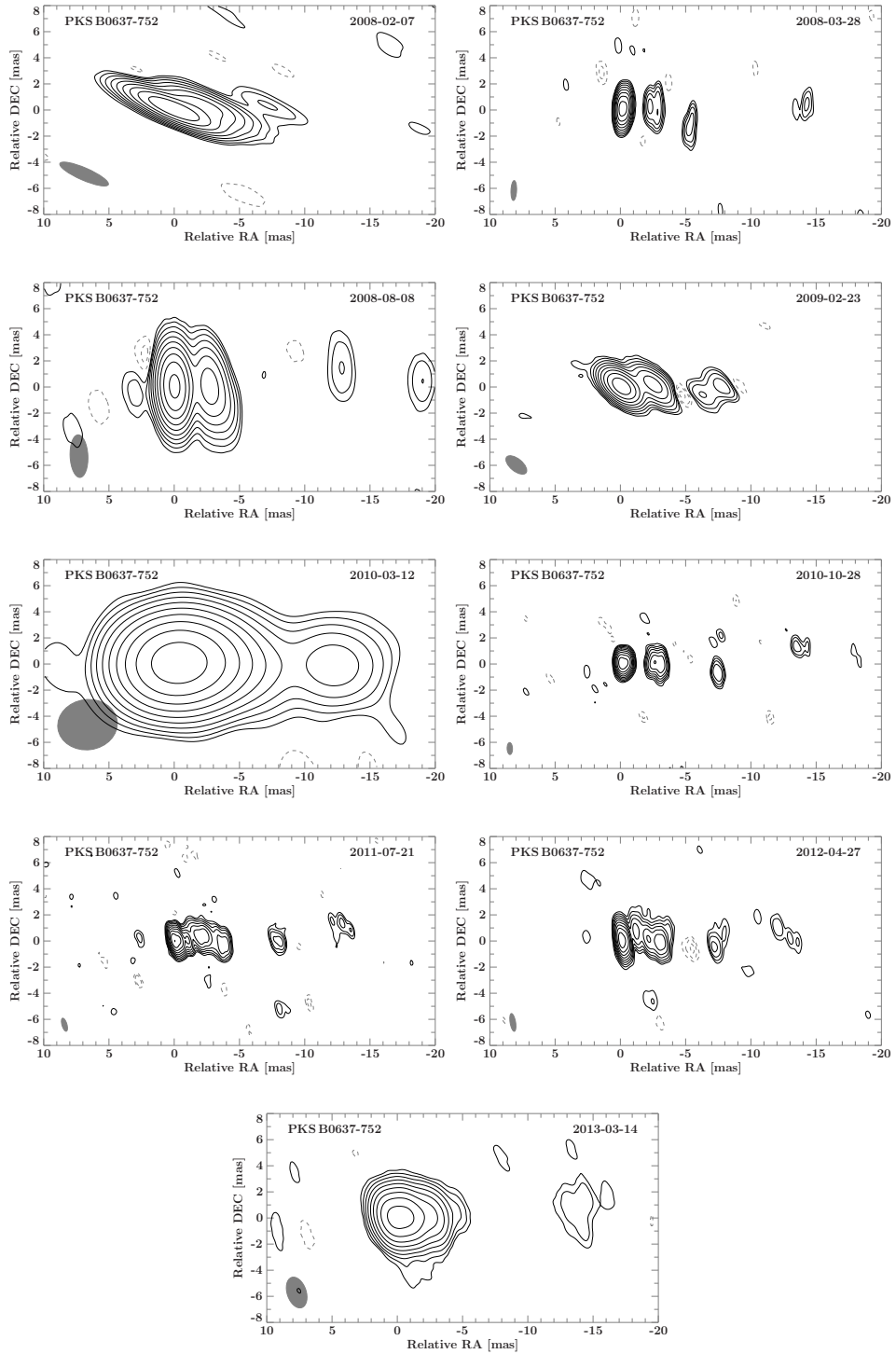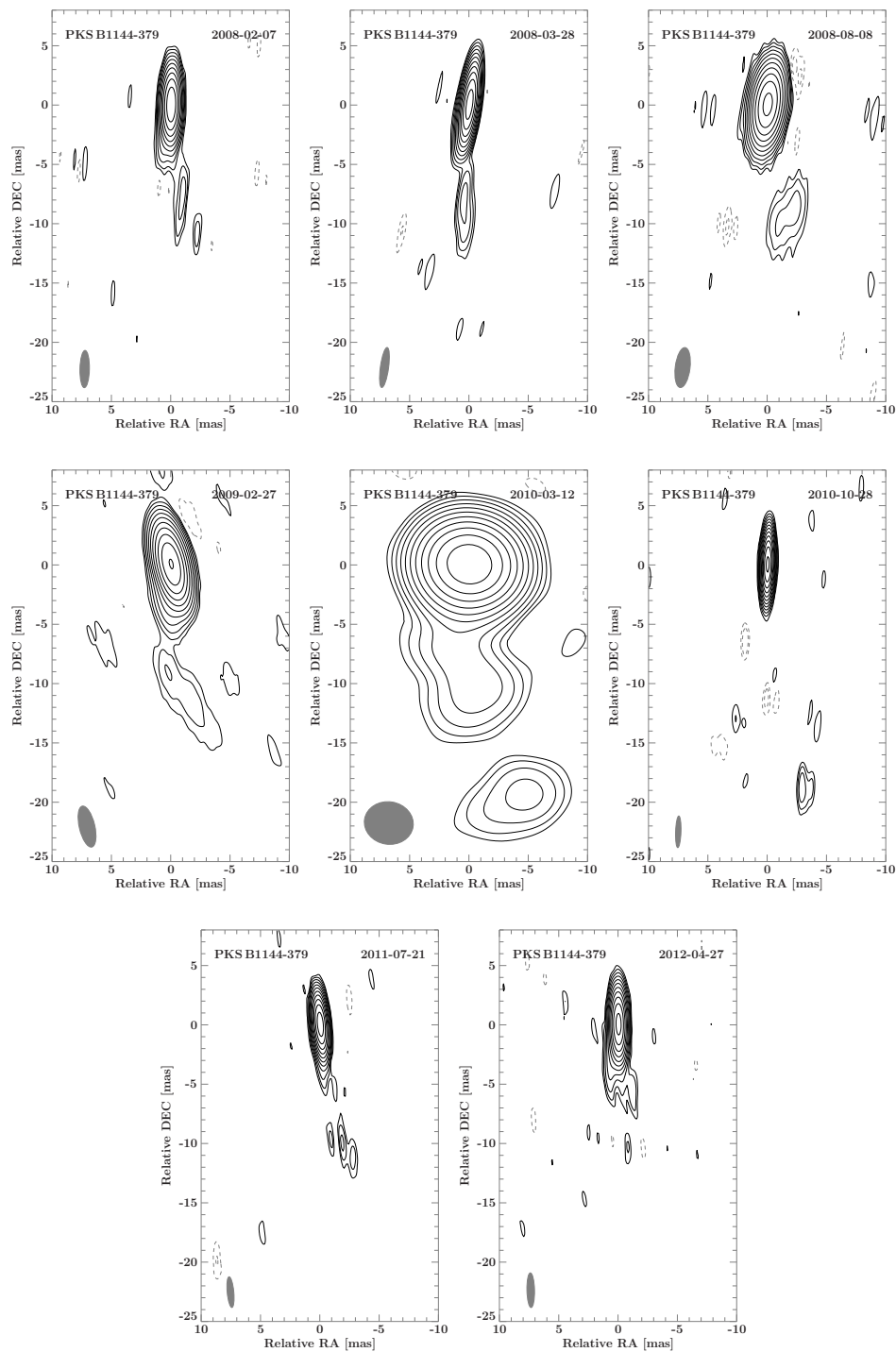
morphology as the one already published in Ojha et al. (2010), albeit with a more clearly cut-out structure in the emission region at around 4 mas (due to slightly different placement of windows in the imaging process). Two distinct components can be identified in this emission region. Those two components can be cross-identified in all other epochs except V252N (dated 2009-09-05), in which the structure is still visible albeit only with two contours. The emission region further out at around 12 mas can be seen as well, however this component will not be used in the kinematic analysis, since there are multiple epochs in which it does not appear. This source features a higher total flux compared to PKS 2204-540. Furthermore, the flux of the first and last epoch has a lower value, however both of these are reconcilable with the assertion of no change in total flux if we again consider the uncertainties (compare Table A.3).

PKS 0637-752

PKS 0637-752 has a jet structure which seems perfectly aligned to the west direction as can be seen in Figure 3.4. This is in agreement with previous findings which show a similar morphology (Tingay et al., 1998; Edwards et al., 2006; Ojha et al., 2010). It should be noted that during the imaging process, there were cases of residuals located to the east of the core, perhaps indicating the existence of a counterjet. However, previous results on this source indicate a low inclination angle resulting in strong Doppler boosting associated with the emission from the jet (Stawarz & Ostrowski, 2002). Thus, the detection of the counterjet of 0637-752 should not be possible since the jet would be far too bright in comparison. As a result, these residuals were interpreted as artifacts and no windows were set in their locations (they might be visible in the clean images regardless, for instance in epoch V252H, dated 2008-08-08). PKS 0637-752 has a very complex morphology with multiple distinct components besides the core. The most obvious ones are those found at distances around 3 mas, 7 mas and 13 mas relative to the phase center, which are all cross-identifiable in almost all epochs. The most interesting finding however might be a more subtle one: the core component in V252T (dated 2010-10-28) shows an extension to the west. This might be a hint for an entirely new component, which is supported by the fact that this epoch is brighter than previous ones and also the brightest epoch available for this analysis (compare Table A.5). This increase in total flux is significant when the uncertainties are taken into account. Taking a look at the beam in V252T and the following two epochs shows that the uv-coverage happened to be very fortunate, resulting in a good resolution along the jet-axis in those epochs which might allow us to track this new component accurately. PKS 0637-752 also features a very bright epoch in V252AIJ (dated 2013-03-14) and a very faint one in V252E (dated 2008-03-28), as well as being the brightest source among those which were studied in the scope of this thesis.

PKS 1144-380

This source shows a bright core with an extension to the south, notably a reoccurring component located roughly 10 mas south relative to the core. This is not in compliance with preliminary images of this source in epoch V252C (dated 2008-02-07) which did show jet structure to the south, however with extensions to the south-east. The image obtained in the scope of this thesis (shown in Figure 3.5) shows jet structure which is angled south south-west instead. The clean images of later epochs confirm this trend, showing jets which are angled straight south or tilted lightly to the west in relation to that. The progression of the total flux in this source is rather violent (compare Table A.7), featuring very low flux in V252P (dated 2010-03-12) followed by more luminous epochs.

PKS 0405-385

The imaging process of PKS 0405-385 had multiple iterations. Earlier iterations yielded a rather compact source with an extension to the west at about 1 to 5 mas. This might very well be the true structure of the source, the results of this thesis are inconclusive on this matter. The issue with these iterations were that despite yielding a morphology that was in agreement with previous VLBI images (Kedziora-Chudczer et al., 2001) as well as compatible within the epochs that were available for this analysis, these clean maps did not yield converging fits in the modelfitting process. This means that it was not possible to fit the core and the extensions with 2D Gaussian components in all epochs in order to do a kinematic analysis. Thus, Table A.9 represents the parameters when imaging 0405 as a compact source. This was done because Kedziora-Chudczer (2006) established PKS 0405-385 as an IDV source, featuring a very compact region which shows variability on timescales of hours. The reason why variability on such timescales might cause issues for VLBI observations is that the data comprises multiple scans of 10 min taken over a couple hours, sometimes spreading out over two days and one general assumption is that the total flux of the source does not fluctuate significantly over that time period. Naturally, IDV sources do not fulfill this requirement. Section 3.5 discusses the possibility of detecting intraday variability in VLBI sources by taking advantage of how the data is taken.

3.4 Kinematic analysis

In order to analyze the sources kinematically, they were fitted using 2D Gaussian components. During the regular imaging process, the clean image is composed of numerous point sources which in sum, describe the data very accurately, yielding detailed images of the brightness distribution. This way,

components can be identified. The point sources in these regions are then removed and replaced by Gaussian models and subsequently modelfitted. This process yields the modelfitting parameters like component flux, distance to the core, position angle as well as major and minor axis which are all saved in a FITS file. The values can then be read out and analyzed. It should be noted that the non-linear least squares minimization technique of the `modelfit`-algorithm need not necessarily yield physical results, since no boundary conditions are initially imposed on the parameters. However, VLBI observations naturally have a finite resolution. This means that the minor and major axis of the Gaussian components have a lower boundary. Kovalev et al. (2005) calculated this minimum size θ_{lim} as a function of the signal-to-noise ratio SNR and the half-power beam size b_{maj}:

$$\theta_{\mathrm{lim}} = b_{\mathrm{maj}} \sqrt{\frac{4 \ln 2}{\pi} \, \ln\left(\frac{\mathrm{SNR}}{\mathrm{SNR} - 1}\right)} \tag{3.1}$$

Equation 3.1 describes the minimum resolvable size of a Gaussian component. Interestingly, this value can be smaller than the size of the resolving beam and the Rayleigh limit. The reason for this is that by applying a Gaussian modelfit, a concrete shape of the emitting region is assumed. In the rare cases where the fit yielded a value for the major/minor axis which was smaller than θ_{min}, the component was considered unresolved and instead, θ_{lim} was used as an upper limit for the component size. The signal-to-noise ratio was computed by determining the noise level in a relatively empty area in the vicinity of the component.

Kovalev et al. (2005) show that the brightness temperature can be expressed by the modeling parameters according to

$$T_{\mathrm{b}} = \frac{2 \ln 2}{\pi \, k_{\mathrm{B}}} \frac{S \lambda^2 \, (1 + z)}{\theta_{\mathrm{maj}} \, \theta_{\mathrm{min}}} \tag{3.2}$$

with S representing the flux of the component, k_{B} being the Boltzmann constant, z describing the redshift of the source and λ the observing frequency. If the size of the component was lower than the resolution limit and θ_{lim} was used as an upper limit for the component size, then the derived brightness temperature represents a lower limit for T_{b}. As discussed earlier, models predict upper limits for intrinsic brightness temperatures like the equipartition value of $10^{11} \, K$ (Readhead, 1994) or the inverse Compton limit of $10^{12} \, K$ (Kellermann & Pauliny-Toth, 1969), however the measured brightness temperatures may still be higher, for instance due to Doppler boosting (Kellermann, 2003).

In the following subsections, the results of the kinematic analysis are discussed in detail.

PKS 2204-540

An overview of the model for PKS 2204-540 is given in Figure 3.6, which presents the clean images overlaid with the Gaussian model components (the images are rotated by 90 degrees in order to accomplish an overlay, the jet structure is facing south). The colors code the components: the central component (the *core*) and the associated regression fit is shown in blue while the second Component *C2* is shown in purple. In three epochs, there is weaker emission found further out. They were not considered for the kinematic analysis however mainly because they do not appear in all epochs and the position angle is not the same for all of them.

The distance evolution of the components is shown in Figure 3.7. The error bars for the distance is assumed to be half the major axis of the fit. The derived apparent velocities are shown in Table 3.3. Within the uncertainties of the linear regression, the observed velocities for C2 are in compliance with the hypothesis of a stationary component. Such stationary components can be explained for instance by standing re-collimation shocks (Lister et al., 2009b).

Table 3.3: Results of the kinematic analysis for 2204-540

Label	apparent velocity[a] [mas/yr]	apparent velocity[a] [c]
Core	0.002 ± 0.005	0.13 ± 0.33
C2	0.056 ± 0.066	3.32 ± 3.97

Notes: [a] Apparent speed was obtained using linear regression, with half the major axis as an estimation for the error.

The plots for the radio flux and the brightness temperature can be seen in Figure 3.8 and 3.9 respectively. The radio light curves feature error bars corresponding to an estimated relative error of 10 %, arising from the calibration and imaging process (this estimation is also used for the fluxes of the other sources which were analyzed kinematically). It is evident that the increase in total flux that was already apparent in the imaging parameters, is reflected in the light curve as well. In this two component model, the main increase in flux is allotted to the core component, while C2 remains stable in most epochs. The brightness temperature does not exceed the inverse Compton limit of 10^{12} K for neither component in any epoch.

PKS 2355-534

The overview plot for PKS 2355-534 is shown in Figure 3.10, featuring its west south-west jet-structure which can be consistently fitted using three
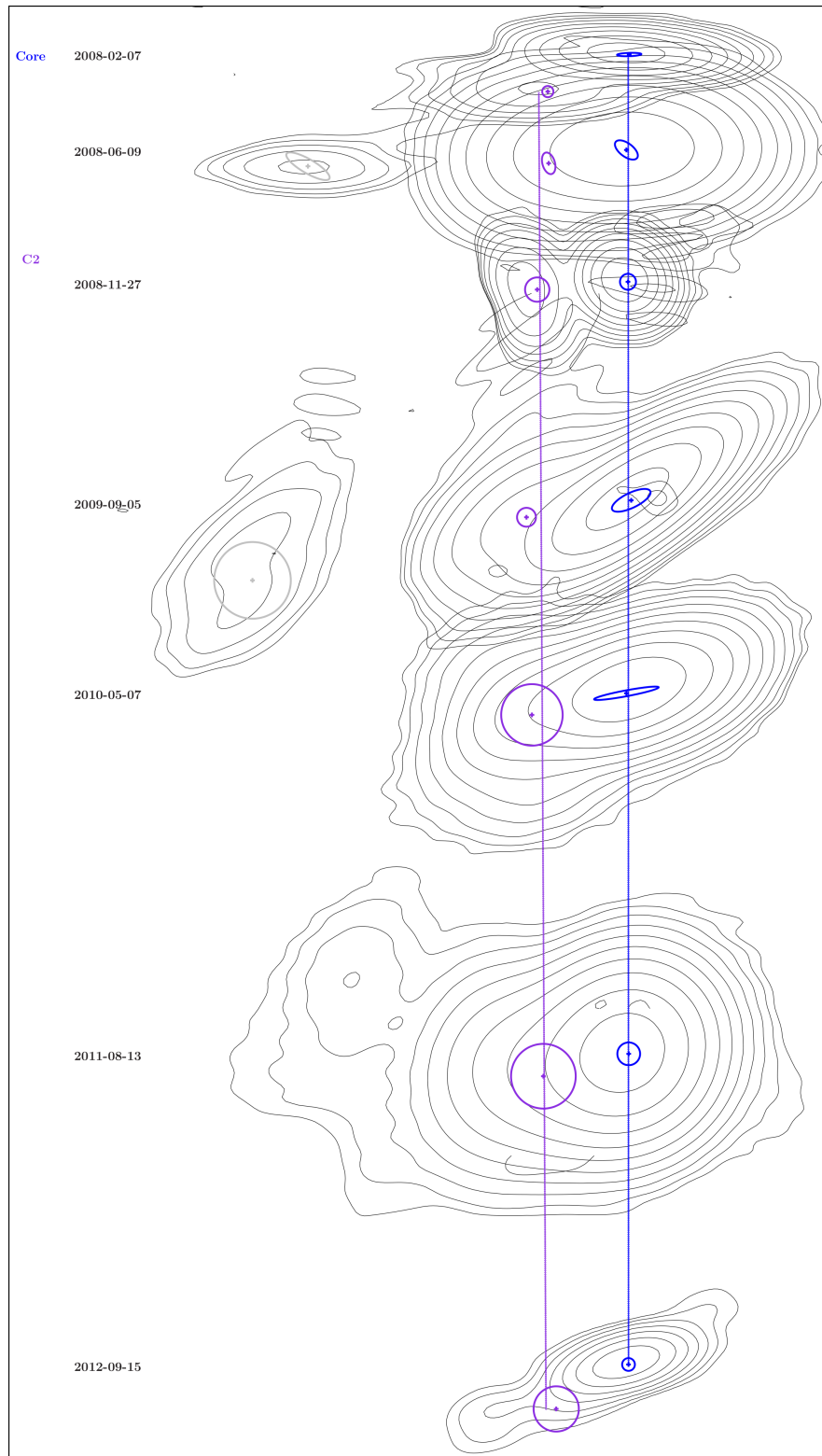
Figure 3.6: Jet evolution of the source 2204-540. The plot shows the clean images of the respective epochs overlaid with the associated model components. The contours correspond to those shown in Figure 3.2. The blue model is the central core component while the purple component is located south-west relative to the core.
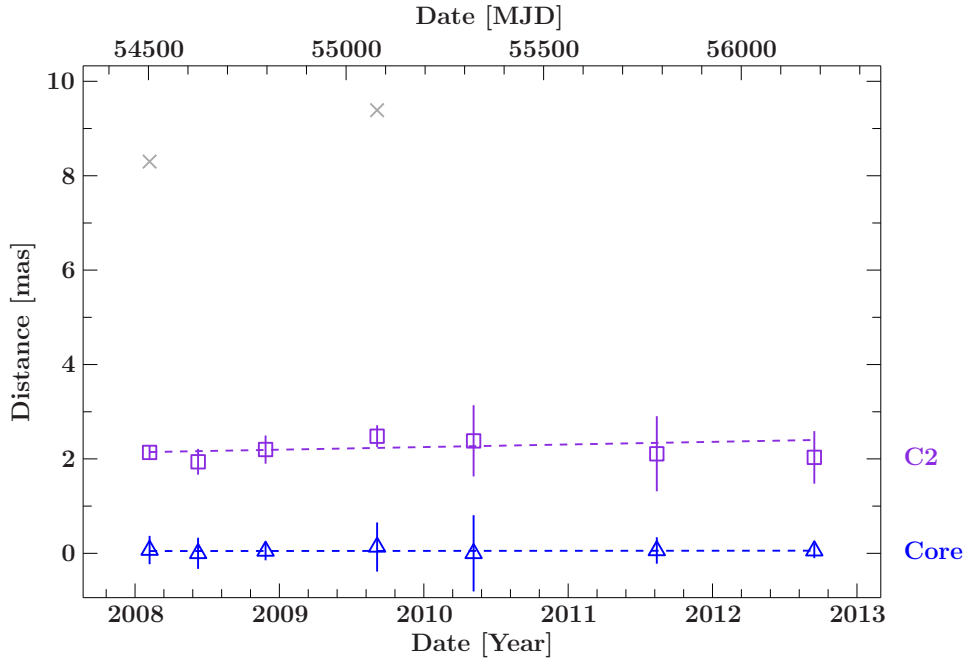
Figure 3.7: Distance evolution for each associated component in 2204-540. Error bars indicate half the major axis of the Gaussian modelfit. The dotted lines represented the fit which was obtained by linear regression. The component C2 is revealed to be stationary within the uncertainties.

components across all epochs. Plotting distance versus time as shown in Figure 3.11 reveals that the two components, which were identified distinct from the core, behave differently from one another. While C3 remains relatively stationary, C2 is rapidly moving outwards with about 0.7 mas/yr which turns out to be superluminal motion even considering the uncertainties of the regression (compare Table 3.4). This behavior of jet components moving with different speeds is well supported by the shock-in-jet model, which may feature standing shocks in otherwise rapidly flowing jets (Lister et al., 2009b). The radio light curve of PKS 2355-534 in Figure 3.12 shows a very stable behavior.
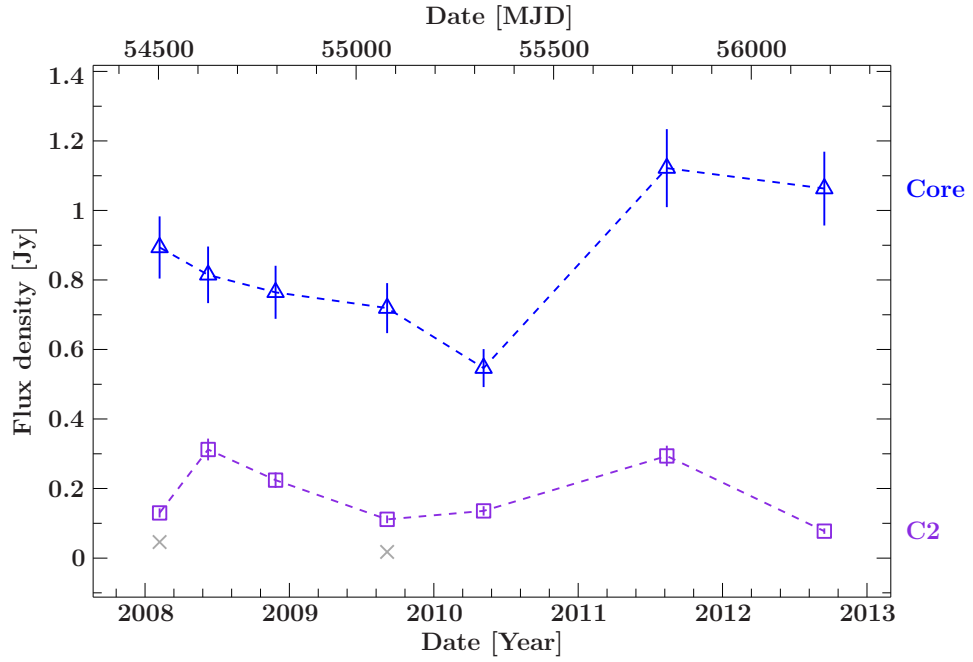
Figure 3.8: Flux density evolution of 2204-540 in seven epochs between 2008 and 2012. The error bars are set to 10% of the flux value.
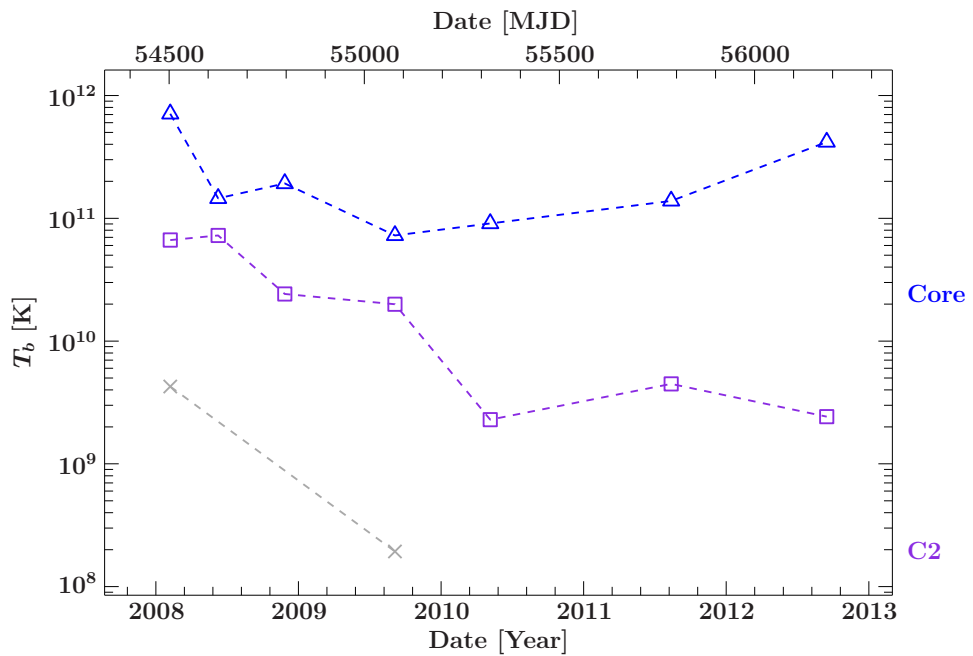

Figure 3.9: Evolution of the brightness temperature plotted in logarithmic scale in 2204-540.

Table 3.4: Results of the kinematic analysis for 2355-534

Label	apparent velocity[a] [mas/yr]	apparent velocity[a] [c]
Core	-0.011 ± 0.004	-0.59 ± 0.21
C2	0.238 ± 0.056	12.46 ± 2.92
C3	0.030 ± 0.032	1.59 ± 1.69

Notes: [a] Apparent speed was obtained using linear regression, with half the major axis as an estimation for the error.

The shown fluxes are all reconcilable with no variability on timescales of years over the duration of the measurement. In comparison to PKS 2204-540, this source is heavily dominated in flux by its core region which is one order of magnitude brighter than the next component, C3. While decreasing flux is to be expected when considering components further away from the core, this effect is more pronounced here than it was in the previous source. The discrepancy is mainly found in the core component: While C3 in 2355-534 is similarly bright compared to C2 in 2204-540, 2350-534's core region is much brighter than its counterpart. The brightness temperature is shown in Figure 3.13, revealing very high values for the core. Striking the eye is $T_{\mathrm{b}} = 1.3 \times 10^{13}$ K in V252C (dated 2008-02-07) as a clear exception to the rule. Note that this value is not a lower limit resulting from θ_{lim}. Instead, the core is merely very compact and slightly less luminous compared to other epochs. If we assume that V252C is an outlier in terms of component size and brightness temperature, the brightness temperature remains stable for the core and follows a similar trend for C2 and C3.

PKS 0637-752

As can be seen in the overview plot in Figure 3.14, PKS 0637-752 was modeled by not four but five distinct components. Such a complex model is mainly possible due to the epochs taken from 2010 to 2012 which offer great spatial resolution in the direction of the jet structure. As the plot shows, it was possible to modelfit C5 (shown with green color in the plot), which represents a new emerging component which is first detectable in the epoch V252T (taken 2010-10-28). The distance evolution of the individual components can be traced in Figure 3.15. C3, C4 and C5 all show significant outward motion. C2 on the other hand is seemingly moving inward. However, the uncertainties of the regression (Table 3.5) reveal that we cannot out rule the more likely hypothesis of a stationary component.

It should be noted however that apparent superluminal inward motion is not strictly ruled out by theory and has been reported in VLBI observations
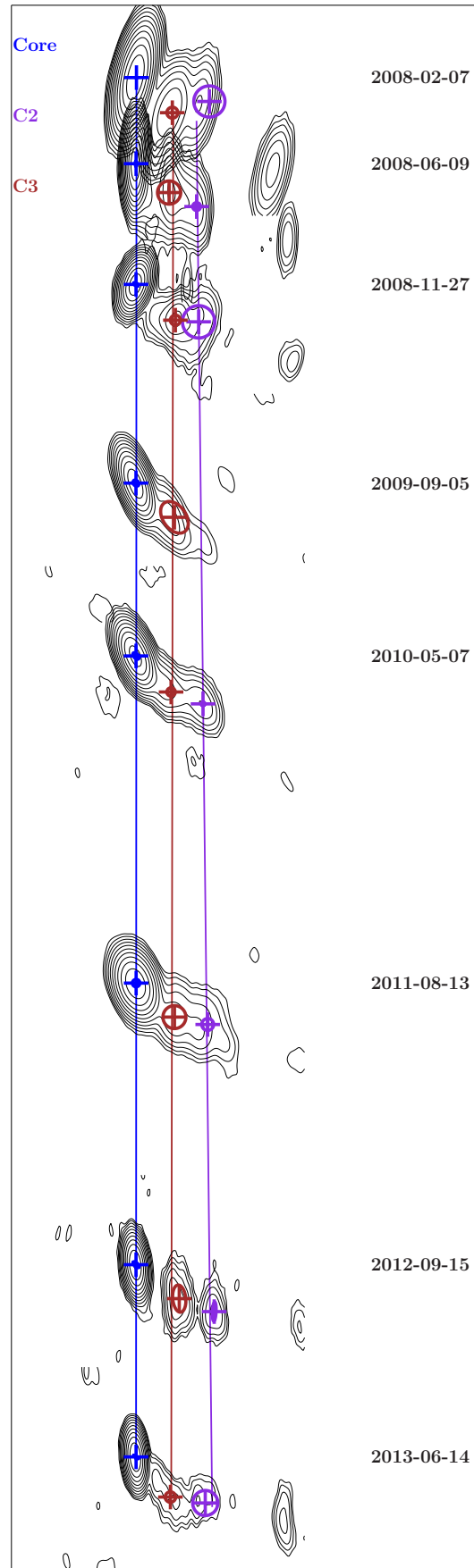
Figure 3.10: Jet evolution of the source 2355-534. The plot shows the clean images of the respective epochs overlaid with the associated model components. The contours correspond to those shown in Figure 3.3. The three component model of core (blue) and C2 and C3 (shown in purple and red) form a jet in south-west orientation.
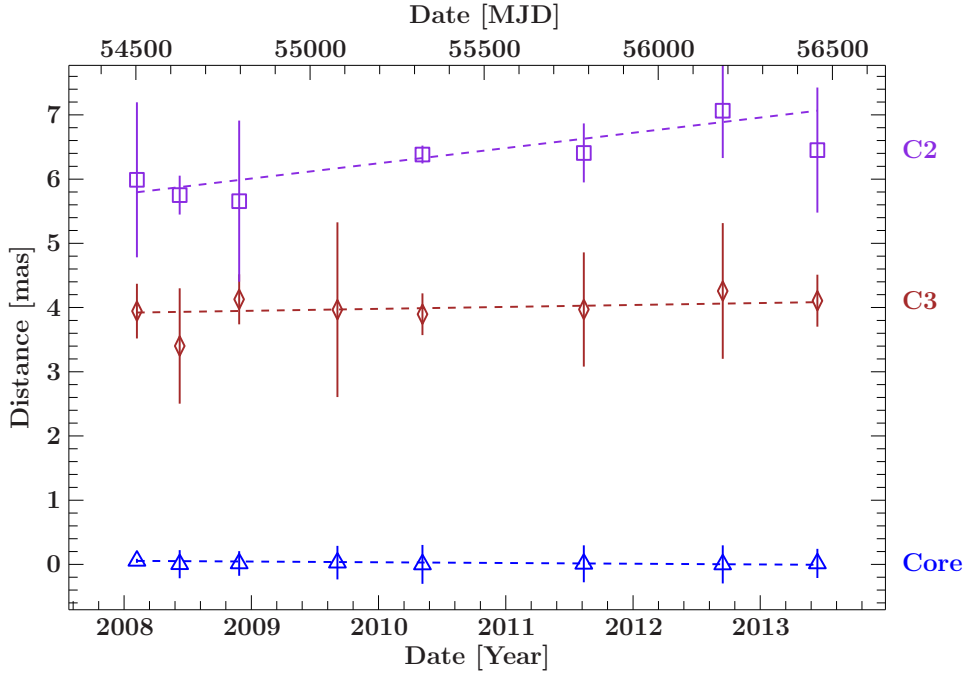
Figure 3.11: Distance evolution for each associated component in 2355-534. Error bars indicate half the major axis of the Gaussian modelfit. The dotted lines represented the fit which was obtained by linear regression. C3 is stationary within the uncertainties. C2 on the other hand features significant outward motion.

before (Niinuma et al., 2012). The superluminal outward motion of C3, C4 and C5 is in agreement with previous results published by Edwards et al. (2006), who reported superluminal motion of $(13.3 \pm 1.0)\,c$ in PKS 0637-752 for VLBI data from 1995 to 2000. Figure 3.17 shows the radio flux for individual components in each epoch. Between 2010 and 2013, the core component becomes fainter and a new component is observed which is initially equally bright compared to the core, then becomes fainter and is seen very bright again in the last epoch. The brightness temperature plot as shown in Figure 3.18 reveals that once again V252C (dated 2008-02-07) features an outlier in T_{b}, but otherwise shows no surprises.

One main goal of the TANAMI program with its associated multiwavelength observations is to check for correlations of changes in the radio morphology with high energy flares. The *Fermi*/LAT γ-ray light curve provided by Michael Kreter is shown in Figure 3.16. The plot reveals a period of heightened activity between the beginning of 2009 and mid 2010 and suggest a flaring event towards the end of 2009. This is in agreement with the detection of a new component in C5 in the radio morphology. From the linear regression of the component we can determine when the jet ejection event
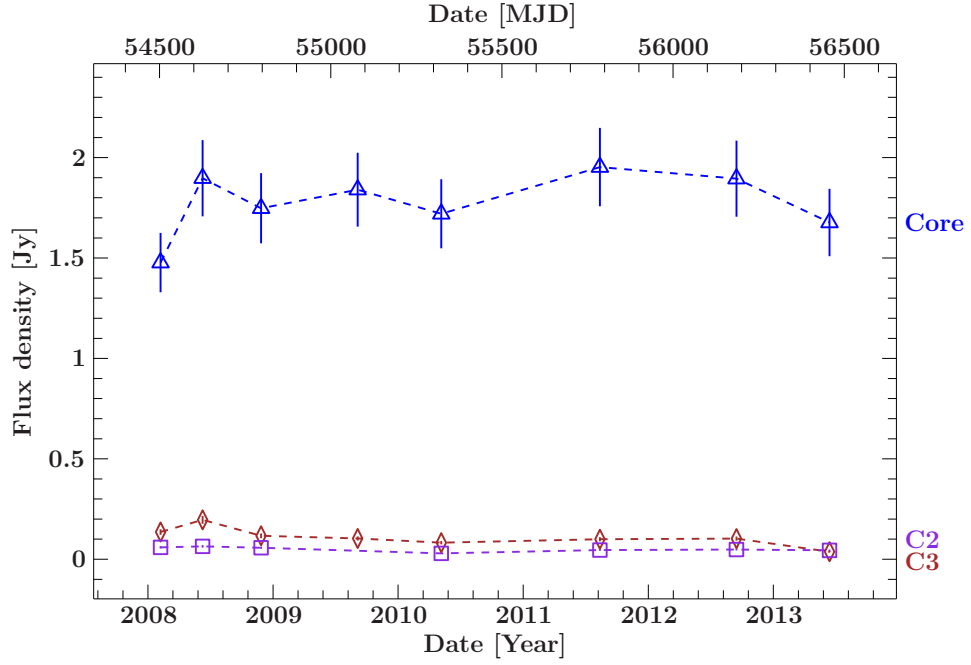
Figure 3.12: Flux density evolution of 2355-534 in seven epochs between 2008 and 2012. The error bars are set to 10% of the flux value.
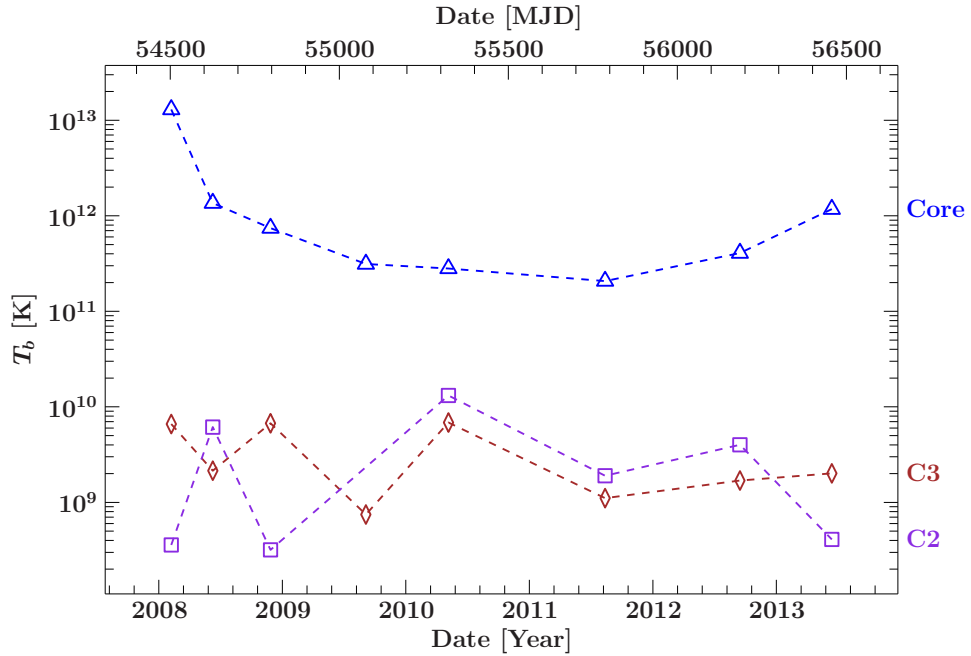

Figure 3.13: Evolution of the brightness temperature plotted in logarithmic scale in 2355-534.

happened. This yields a date of (2009.8 ± 0.9), the uncertainty originating from the linear regression. While this level of uncertainty does not allow us to infer if the change in radio morphology predated or postdated the flaring event (or even happened at the same time), this result is a strong hint for a correlation between the two. This result can not be understated as finding this kind of correlation is precisely what TANAMI as a multiwavelength program was designed for in the very first place. This finding is a strong indicator that changes in the parsec-scale structure are related to high-energy flaring and might answer questions about the production mechanisms and sites of highly energetic photons.

Table 3.5: Results of the kinematic analysis for 0637-752

Label	apparent velocity[a] [mas/yr]	apparent velocity[a] [c]
Core	0.002 ± 0.004	0.08 ± 0.15
C2	-0.159 ± 0.184	-5.97 ± 6.87
C3	0.365 ± 0.167	13.64 ± 6.23
C4	0.246 ± 0.070	9.20 ± 2.64
C5	0.439 ± 0.226	16.44 ± 8.47

Notes: [a] Apparent speed was obtained using linear regression, with half the major axis as an estimation for the error.

PKS 1144-379

The overview plot for the model in PKS 1144-379 is shown in Figure 3.19. Besides the core component, two additional components were identified. The newest component C3 shows significant outward motion, which can also be seen in the distance evolution in Figure 3.20. C2 however is seemingly stationary. It should be noted that the position angle in the modelfit components of C2 features considerable variations (compare Table A.8). However, the emission regions of C2 are also rather large (which is reflected in the values of b_{min} and b_{maj}). Table 3.6 shows that C2 can be regarded as a stationary emission region within the uncertainties while C3 is a outward moving feature with superluminal velocities. Figure 3.21 shows the radio light curve of PKS 1144-379. Its flux is extremely core dominated with significant variability, especially toward the later epochs after 2010. The brightness temperature evolution is shown in Figure 3.22, revealing very large values for the core emission region which surpasses the inverse Compton limit in four epochs. These observations are unsurprising considering that PKS 1144-379 is a known IDV source and only sources with a bright and very compact
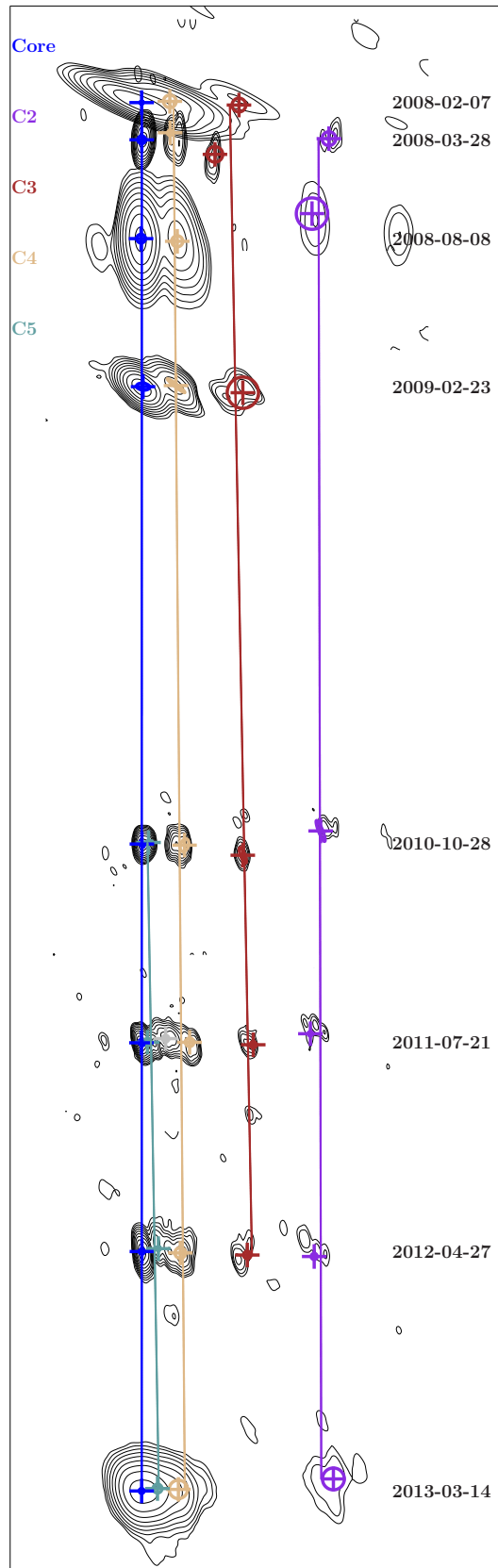
Figure 3.14: Jet evolution of the source 0637-752. The plot shows the clean images of the respective epochs overlaid with the associated model components. The contours correspond to those shown in Figure 3.4. The five component model reveals a jet oriented west.
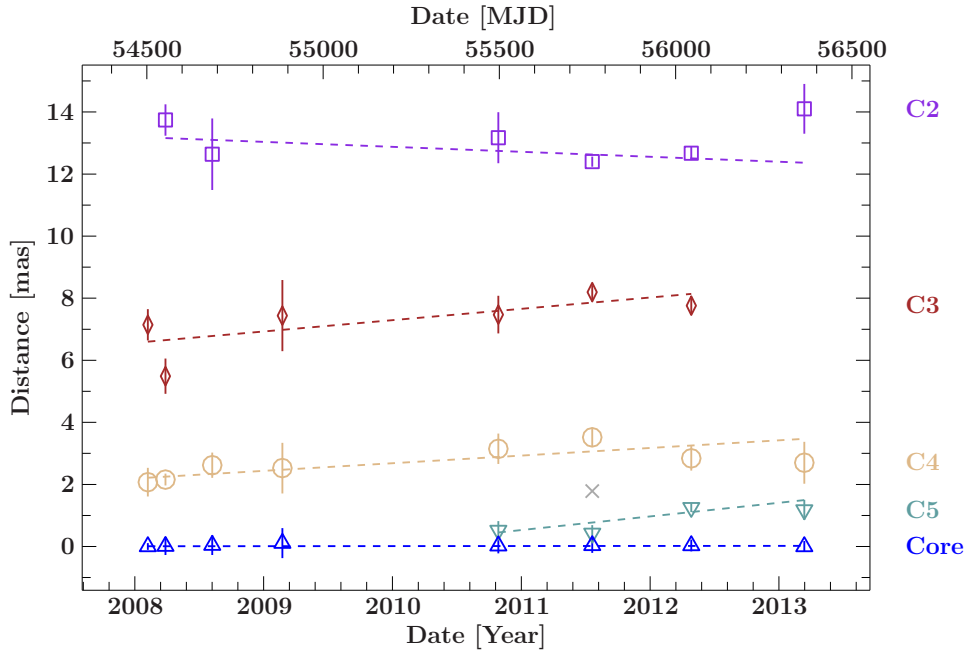
Figure 3.15: Distance evolution for each associated component in 0637-752. Error bars indicate half the major axis of the Gaussian modelfit. The dotted lines represented the fit which was obtained by linear regression. C3, C4 and C5 show significant outward motion. C2 however features inward motion which turns out to be reconcilable with no motion within uncertainties. C5 is a candidate for a potential jet ejection event.

emission region are capable of showing ISS. As mentioned earlier, variability on timescales of hours violates the assumption in VLBI imaging that the flux is constant over the observation time of each epoch. However, IDV sources whose variability can be explained by ISS also show periods where these fluctuations do not occur. This might be why the modelfitting process was successful for this IDV source. Nevertheless, a *Fermi*/LAT light curve was provided by Michael Kreter in the hope that correlations might be found for the variability in the radio flux. The γ-ray light curve is shown in Figure 3.23. However, no flaring event can be observed in this data (the observed flux is comparable with the background flux in the γ-ray light curve for PKS 0637-752).
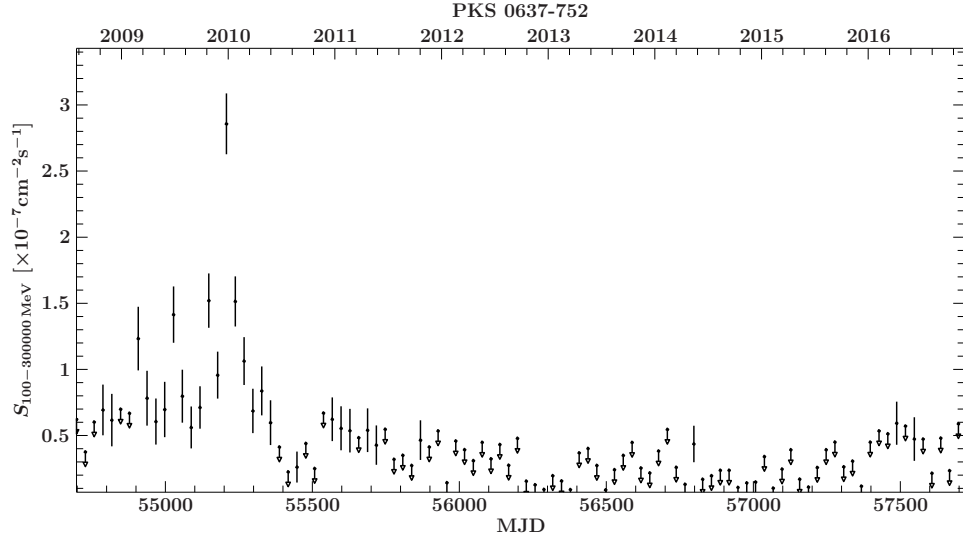
Figure 3.16: Fermi light curve of 0637-752. The x-axes show the time in years (top) and represented in major julian date (bottom). Points are detections while downward pointing arrows represent upper limits. The light curve yields a state of high activity before mid 2010 and suggests a flaring event towards the end of 2009. Credit: Michael Kreter

Figure 3.17: Flux density evolution of 0637-752 in eight epochs between 2008 and 2013. The error bars are set to 10% of the flux value. The behavior of the fluxes of the Core and C5 might indicate a jet ejection event.
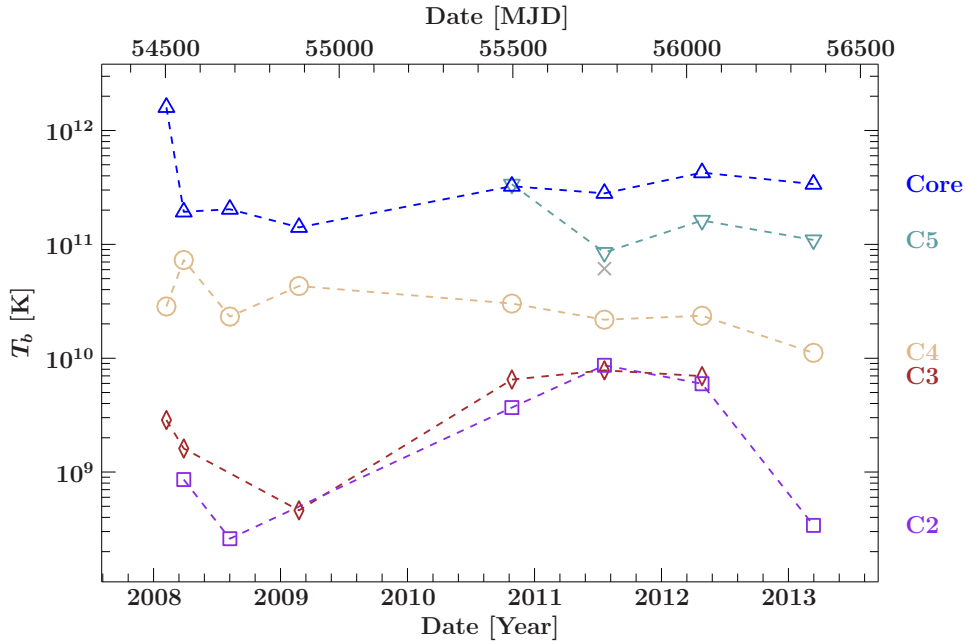
Figure 3.18: Evolution of the brightness temperature plotted in logarithmic scale in 0637-752.

Table 3.6: Results of the kinematic analysis for 1144-379

Label	apparent velocity[a] [mas/yr]	apparent velocity[a] [c]
Core	0.009 ± 0.004	0.50 ± 0.22
C2	0.024 ± 0.153	1.28 ± 8.27
C3	0.717 ± 0.177	38.74 ± 9.56

Notes: [a] Apparent speed was obtained using linear regression, with half the major axis as an estimation for the error.

3.5 Detecting the Intraday Variability of PKS 0405-385

As discussed in Section 3.3, imaging IDV sources using VLBI techniques is notoriously difficult due to the fact that the general assumption of a constant source flux over the duration of the measurement is not met. PKS 0405-385 is an extreme intraday variable scintillator and arguably the figurehead of ISS since interstellar scintillation was first established as the main explanation
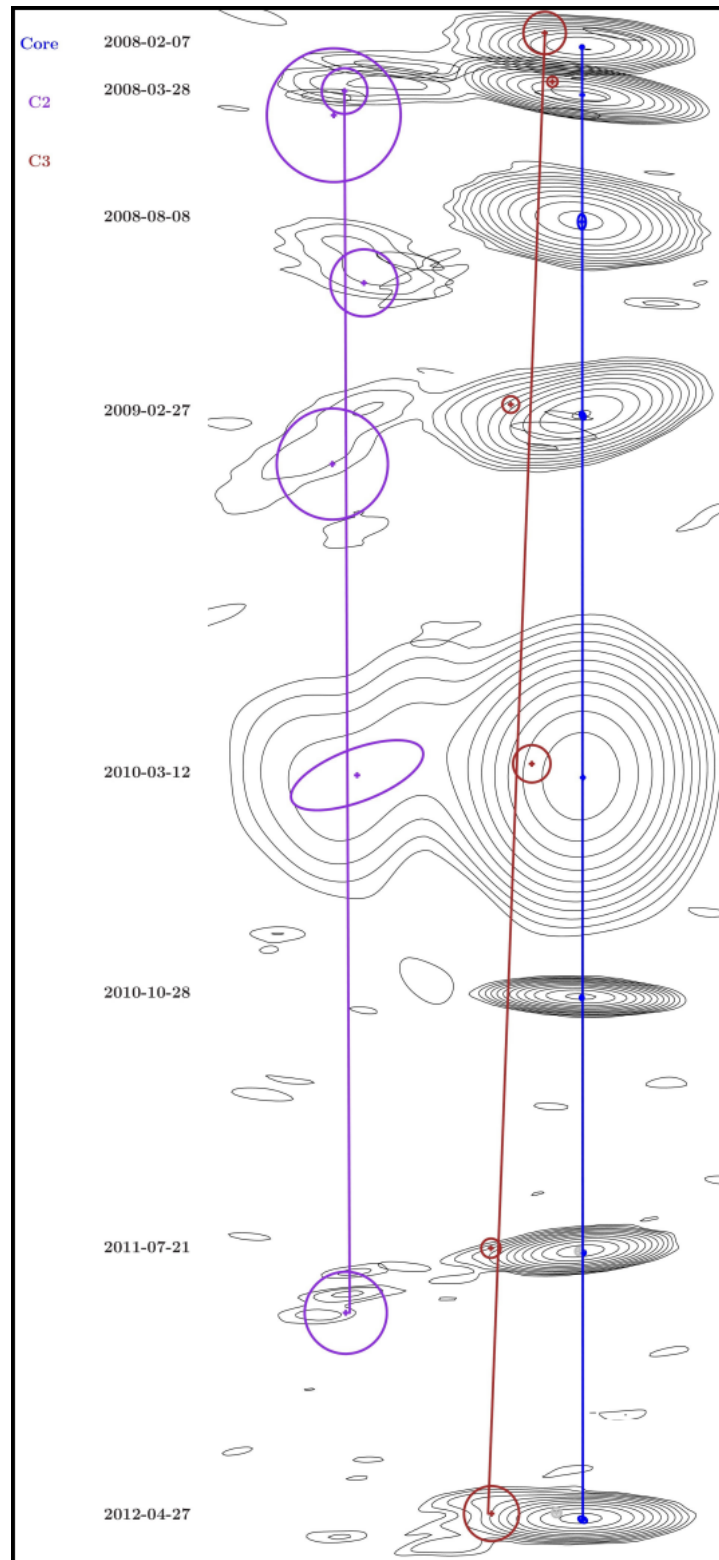
Figure 3.19: Jet evolution of the source 1144-379. The plot shows the clean images of the respective epochs overlaid with the associated model components. The contours correspond to those shown in Figure 3.5. The three component model of core (blue) and C2 as well as C3 (purple and red) forms a jet directed south.
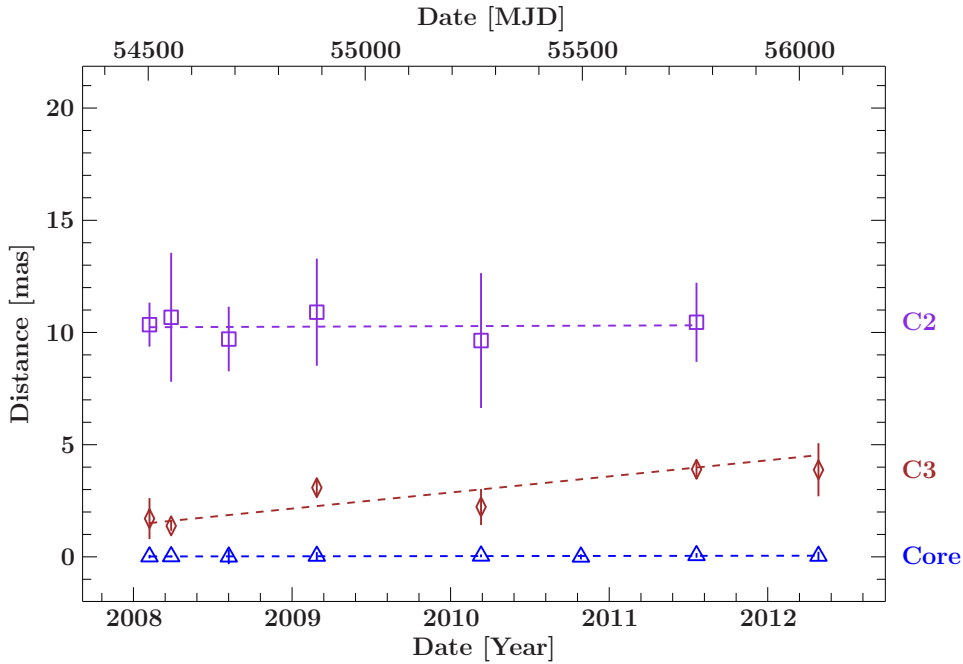
Figure 3.20: Distance evolution for each associated component in 1144-379. Error bars indicate half the major axis of the Gaussian modelfit. The dotted lines represented the fit which was obtained by linear regression.

for IDV in AGN in this particular source. Despite the fact that IDV sources also show periods of non-variability on these timescales, it is quite plausible to assume that variability during the time frame when TANAMI gathered data led to the issues in the imaging process. However, the same variability also offers the opportunity to test if it is possible to detect IDV in TANAMI data, creating a precedent that would allow to identify variability in sources that were not previously known to show IDV. The detection of variability utilizing VLBI is not completely unheard of. Savolainen & Kovalev (2008) reported the detection of large-amplitude IDV in QSO 1156+295 in the framework of the MOJAVE survey program with the VLBA at 15 GHz.

A plot visualizing when data was taken for each telescope in the array is shown in Figure 3.24 (the data represents the V252C epoch in PKS 0405-385). It shows the individual scans with a duration of 10 min each, spread out over the total length of the observation (in this case about 4 h; In the case of the available epochs, the longest was about 24 h). It is possible to sample the observation, only selecting individual scans by flagging the remaining data. Naturally, flagging so much data would not help the imaging process and it would be impossible to recover a deep clean image. However, the idea here is to recover a value for the total flux of the source in order to
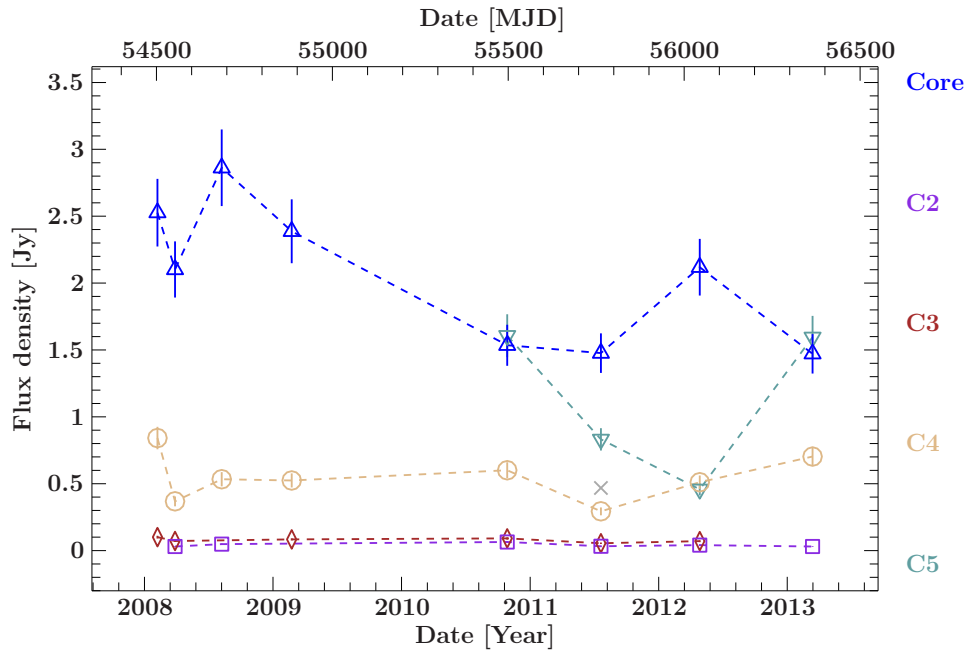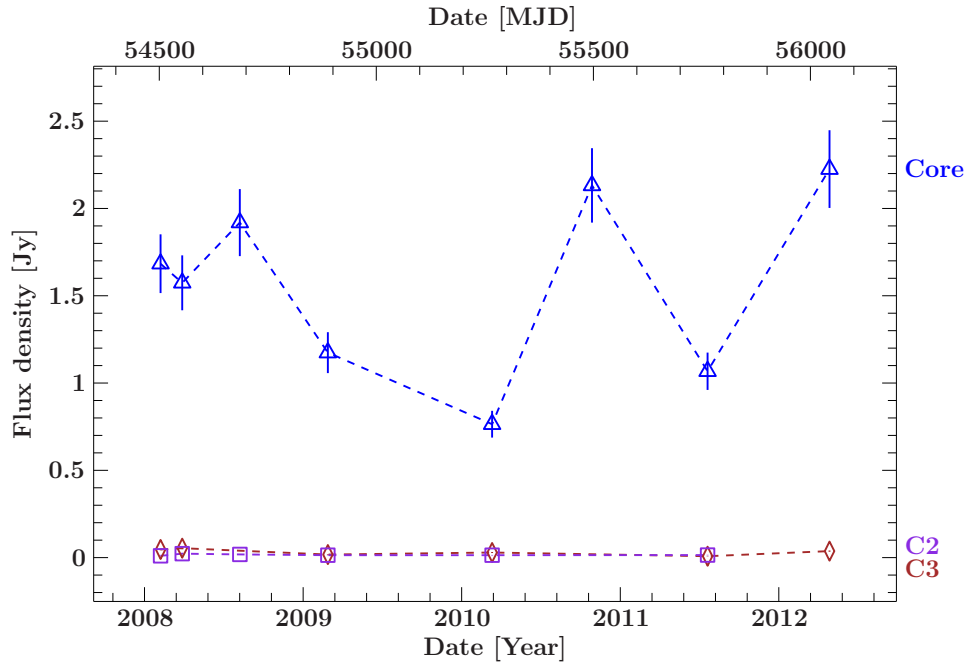
Figure 3.21: Flux density evolution of 1144-379 in nine epochs between 2008 and 2013. The error bars are set to 10% of the flux value. The behavior of the fluxes of the Core and C5 might indicate a jet ejection event.

obtain a light curve to infer information about the variability during the observation. According to Kedziora-Chudczer (2006), only the most compact radio sources can scintillate. More specifically in the case of PKS 0405-385, the size of the component that is scintillating has to be smaller than 5 μas. Thus, the imaging process can be performed using a single 2D Gaussian component modeling the scintillating core of the source. The source is then processed using regular imaging methods (as described in Section 2.6) and a value for the flux associated with this scan can be extracted. The idea behind this is that the assumption of a non-fluctuating source flux might not be given over the whole observation period, but it might be met for the individual scans of 10 min duration each.

Plotting the resulting fluxes against the time at which the scans were started yields the light curves shown in Figure B.1 (Appendix B). From a phenomenological point of view, we observe a constant flux in the first two epochs. In the following epochs, variability can be observed. In order to motivate that this approach yields plausible results, Table 3.7 compares the mean fluxes of these light curves with the total fluxes that we initially extracted from the images which were created using the full dataset for each epoch. We observe that for the most part, this method yields reasonable values for the fluxes.
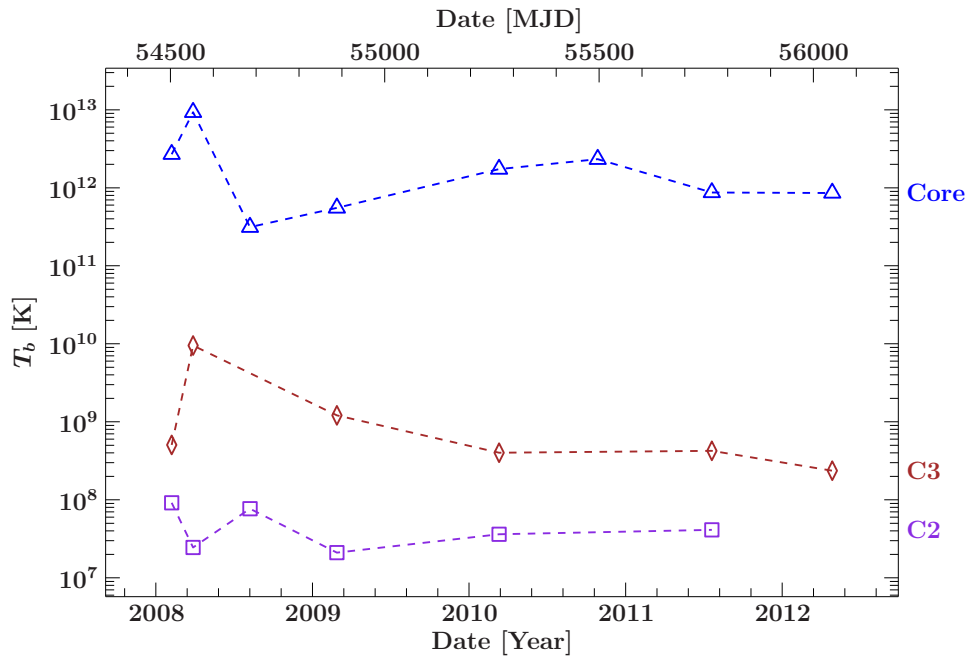
Figure 3.22: Evolution of the brightness temperature plotted in logarithmic scale in 1144-379.
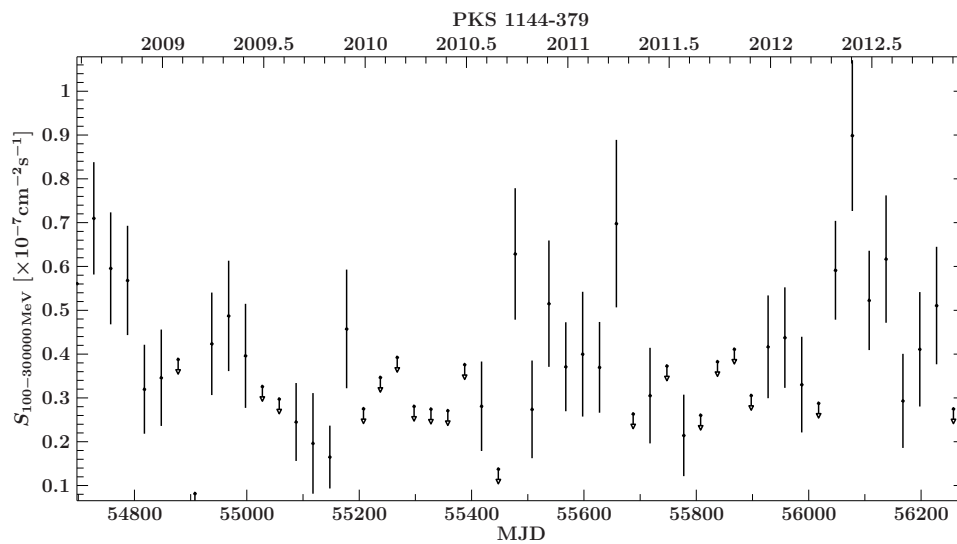
Figure 3.23: Fermi light curve of 1144-380. The x-axes show the time in years (top) and represented in major julian date (bottom). Points are detections while downward pointing arrows represent upper limits. No flaring event is observed. Credit: Michael Kreter
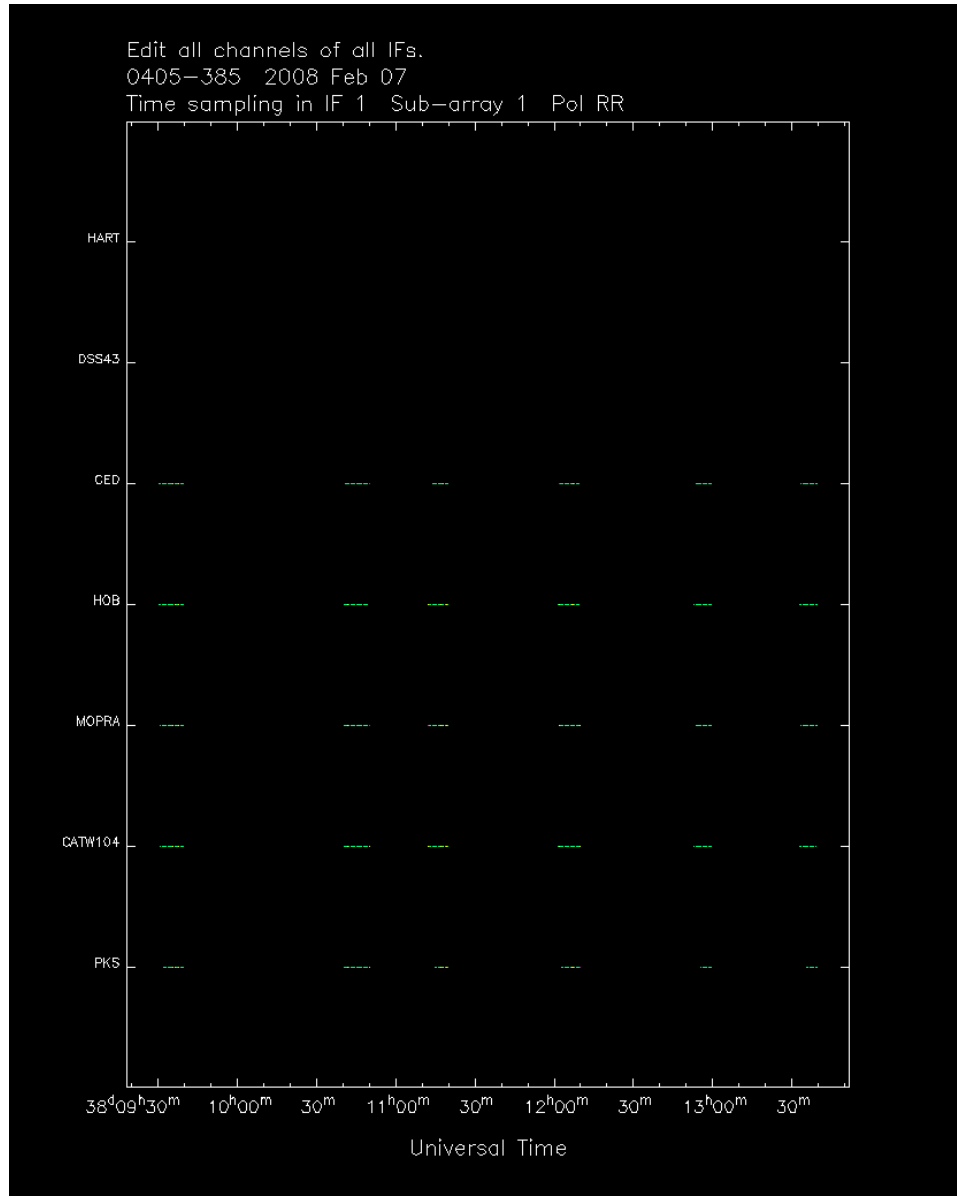
Figure 3.24: The plot visualizes when data was taken in one epoch (V252C) of PKS 0405-385. The x-axis shows the time and reveals the duration of the individual scans of 10 min. The y-axis shows the telescope involved in the observations (although this is not evident in this epoch, the array-configuration was not necessarily fixed throughout all scans). The sampling is also not equitemporal, sometimes with long gaps between scans (compare Figure B.1).

Table 3.7: Flux evaluation in PKS 0405-385

Epoch yyyy-mm-dd	S_{total}[a] [Jy]	S_{mean}[b] [Jy]	Δ[c] [%]
2008-02-07	1.41	1.402	2.97
2008-03-28	1.26	1.312	3.18
2008-08-08	1.37	1.377	7.75
2009-02-23	1.1	1.088	12.10
2010-03-12	1.2	1.224	5.39
2010-10-28	1.52	1.534	7.56
2011-07-21	1.14	1.102	7.078
2012-04-27	1.12	1.201	9.274
2013-03-14	1.42	1.41	0

Notes: [a] Total flux obtained when imaging the epoch with all scans.
[b] Mean flux of the Total flux values obtained when imaging each individual scan.
[c] Maximum relative deviation in flux of individual scans from S_{mean}.

However, there are two big issues with this approach of attempting to detect IDV using VLBI in this fashion, which are both evident in the light curves. The first one is an inherent problem which cannot be corrected for: undersampling. This factor already rules out a reliable inference of the timescales of the variability (even if it were established that the source it variable) due to aliasing. For IDV sources, these timescales are very short, in the case of PKS 0405-385 around 2 hours (Kedziora-Chudczer et al., 1997). For obvious reasons, TANAMI data was never taken with such considerations in mind to begin with. The best case scenario can be seen in V252T where four scans were taken in such a time frame. Due to undersampling, an IDV source might appear reconcilable with the hypothesis of a stable source due to unfortunate temporal spacing of the data points. The other challenge is the evaluation of the uncertainties without which it is impossible to draw any conclusions from such data. Unfortunately, `DIFMAP` does not offer any way to obtain intrinsic uncertainties from the data (see Section 2.6). Attempts to derive uncertainties for TANAMI data are empirical in nature. For instance, the gain correction factors in many observations were statistically analyzed in order to obtain an error for the flux values. However, such an evaluation does not exist for flux values derived from individual scans yet. The obvious solution to this issue is to analyze more sources in this fashion, i.e. obtaining a scan-resolved flux analysis in order to quantify the uncertainties.

The results for the sources that were analyzed this way up to this point are shown in Table B.1. Neither of the first two sources (PKS 2204-540 and PKS

0637-752) have been reported to show IDV in previous publications. Thus, we can use these in order to get an estimation for the typical error associated with inferring flux values from data limited to single scans by assuming that these don't show variability during the observation. For these two sources, we can attest that the standard deviation of the scan-resolved flux values never exceeds 5 % of mean flux of all scans in the epoch. In fact, the results motivate that an in-depth analysis involving more sources in the TANAMI sample yield should generally yield a low uncertainties. Until then, the value of 5 % was adopted in the in the light curves (Figure B.1) as a conservative estimation.
The standard deviation in flux was also calculated for the known IDV sources PKS 0405-385 and PKS 1144-379. The results show slightly higher uncertainties, indicating that the light curves of those sources are less reconcilable with the assumption of non-variability compared to the first two sources.

Can we infer the existence of IDV in PKS 0405-385 during the observation period. At the current point in the analysis, no. The flux curves look promising enough, revealing variations of the same magnitude that previous results have established (Kedziora-Chudczer et al., 2001). However, preliminary results (the uncertainties inferred by the flux values of PKS 2204-540 and PKS 0637-752) indicate that the uncertainties might not be low enough in order to rule out even the hypothesis of no measurable variability on these timescales. However, further scan-resolved flux measurements on other sources in the TANAMI samples are required in order to obtain an unbiased sample and thus a more reliable way to establish the uncertainties of the approach. Such an analysis would also be able rule out the possibility of a correlation of uncertainties with the observing epoch itself (there are no immediate hints of this so far, but the sample size is too small).
At the same time, sampling poses problems. In principal, VLBI data can reveal the existence of variability in IDV sources but detecting precise values for the corresponding timescales might remain a rather serendipitous possibility (Savolainen & Kovalev, 2008).
On a different note, analyzing individual scans can also benefit the overall imaging process. In VLBI imaging, data quality is frequently evaluated by comparing data from different telescopes or baselines. Parsing individual scans can reveal cases where one telescope is off merely in one scan, which means that this data can be corrected for using self-calibration without affecting the data in different scans.

Chapter 4

Summary and Outlook

Unraveling the intrinsic structure and emission mechanisms of extragalactic jets in Active Galactic Nuclei requires great precision regarding both spatial and temporal resolution as well as multiwavelength observations. This thesis focused on 6 years of VLBI data from the TANAMI project supplemented by γ-ray data detected by *Fermi*/LAT.

Very Long Baseline Interferometry offers great spatial resolution, which allowed tracking the morphology of AGN from the southern hemisphere on sub-parsec scales. Regarding the imaging process itself, it was demonstrated that phase self-calibration is beneficial as an initial step before averaging the data. Five sources were imaged in up to nine epochs Most of these sources have not been studied in detail on these scales before. By identifying components in the jet morphology, the apparent jet velocity was determined. Stationary components were detected, but also ones which were moving outwards with apparent superluminal velocities. Notably, previous results on apparent jet speeds in PKS 0637-752 of $(13.3 \pm 1.0)\,c$ given by Edwards et al. (2006) were confirmed. Furthermore, a new component was found in the same source to be emerging during the observing period in a way such that the presumed jet ejection event could successfully be dated to (2009.8 ± 0.9). A flaring event in the γ-ray regime was found coinciding with this detection, further underlining the close link between changes in the parsec-scale morphology and high-energy flaring events (e.g. Jorstad et al., 2012; Marscher et al., 2012; Rani et al., 2014). A fast-moving component with $(38.74 \pm 9.56)\,c$ as well as a dip in the core luminosity was found in PKS 1144-379 (the latter perhaps indicating another jet ejection event). However, a corresponding γ-ray light curve should no flaring events.

Since two of the sources were known to manifest intraday variability in the past, a new approach of analyzing VLBI data was proposed, which allows the retrieval of radio light curves on timescales of hours. While light curves for the extreme scintillator PKS 0405-385 look indicative of IDV, sampling issues remain a systematic problem in confirming the associated timescales.

69

Also, preliminary results of a survey of other sources in this regard indicate, that the uncertainties associated with obtaining flux values in this fashion might pose a problem. However, more sources need to be analyzed in this way, forming an unbiased sample and yielding more reliable estimations for the uncertainties.

Appendix A

Modelfit and imaging parameters

The following tables cover the results for the imaging process as well as the parameters for each individual jet component of the kinematic studies.

A.1 PKS 2204-540

Table A.1: Imaging parameters for 2204-540

Epoch yyyy-mm-dd	S_{total} [Jy]	S_{peak} [Jy/beam]	σ^{a} [mJy/beam]	$b_{\text{maj}}^{\text{b}}$ [mas]	$b_{\text{min}}^{\text{b}}$ [mas]	P.A.$^{\text{c}}$ [$^{\circ}$]
2008-02-07	1.08	0.88	0.80	2.60	0.66	-2.7
2008-06-09	1.13	0.90	0.59	2.96	1.76	-0.7
2008-11-27	0.99	0.70	0.49	1.20	1.02	-36.1
2009-09-05	0.85	0.66	0.31	3.34	1.19	36.2
2010-05-07	0.70	0.46	0.16	2.40	1.38	23.9
2011-08-13	1.44	1.12	0.47	2.43	2.27	54.1
2012-09-15	1.14	0.92	2.68	1.71	0.71	14.7

Notes: $^{\text{a}}$ Noise level of the image.
$^{\text{b}}$ Major and minor axis.
$^{\text{c}}$ Position angle.

Table A.2: Modelfit parameters for 2204-540

Epoch yyyy-mm-dd	Comp	S [Jy]	d^{a} [mas]	θ^{b} [°]	$b_{\mathrm{min}}{}^{\mathrm{c}}$ [mas]	$b_{\mathrm{maj}}{}^{\mathrm{c}}$ [mas]	T_{b} [10^9K]
2008-02-07	Core	0.894	0.070	-5.71	0.08	0.60	709.51
2008-06-09	Core	0.815	0.000	0.	0.33	0.66	145.35
2008-11-27	Core	0.765	0.049	36.75	0.39	0.39	192.06
2009-09-05	Core	0.719	0.135	28.21	0.37	1.04	72.53
2010-05-07	Core	0.546	0.000	0.	0.14	1.61	90.64
2011-08-13	Core	1.122	0.060	16.03	0.56	0.56	138.55
2012-09-15	Core	1.063	0.055	19.53	0.31	0.31	417.88
2008-02-07	C2	0.130	2.139	-154.59	0.28	0.28	66.51
2008-06-09	C2	0.312	1.939	-170.25	0.31	0.55	72.39
2008-11-27	C2	0.224	2.199	-175.77	0.60	0.60	24.20
2009-09-05	C2	0.111	2.482	-171.84	0.46	0.46	19.97
2010-05-07	C2	0.136	2.383	-167.12	1.51	1.51	2.29
2011-08-13	C2	0.294	2.110	-165.34	1.59	1.59	4.48
2012-09-15	C2	0.078	2.032	-148.1	1.11	1.11	2.42

Notes: [a] Relative distance to the phase center.
[b] Major and minor axis.
[c] Position angle of the component.

A.2 PKS 2355-534

Table A.3: Imaging parameters for 2355-534

Epoch yyyy-mm-dd	S_{total} [Jy]	S_{peak} [Jy/beam]	σ^{a} [mJy/beam]	$b_{\text{maj}}{}^{\text{b}}$ [mas]	$b_{\text{min}}{}^{\text{b}}$ [mas]	P.A.$^{\text{c}}$ [°]
2008-02-07	1.69	1.49	0.13	3.64	1.23	-11.7
2008-06-09	2.17	1.85	0.18	2.94	0.76	-0.9
2008-11-27	1.96	1.61	0.32	1.98	0.95	-16.0
2009-09-05	1.96	1.68	0.63	2.63	0.97	19.1
2010-05-07	1.83	1.57	0.37	2.49	1.05	21.2
2011-08-13	2.11	1.80	0.62	2.43	1.41	15.5
2012-09-15	2.04	1.63	0.50	2.19	0.74	5.1
2013-06-14	1.79	1.51	0.48	2.17	0.71	3.8

Notes: [a] Noise level of the image.
[b] Major and minor axis.
[c] Position angle.

Table A.4: Modelfit parameters for 2355-534

Epoch yyyy-mm-dd	Comp	S [Jy]	d^{a} [mas]	θ^{b} [°]	$b_{\mathrm{min}}{}^{\mathrm{c}}$ [mas]	$b_{\mathrm{maj}}{}^{\mathrm{c}}$ [mas]	T_{b} [10^9K]
2008-02-07	Core	1.477	0.056	-147.05	0.06	0.06	12976.06
2008-06-09	Core	1.897	0.002	-158.68	0.11	0.44	1357.12
2008-11-27	Core	1.748	0.014	167.62	0.21	0.38	743.10
2009-09-05	Core	1.840	0.027	11.4	0.40	0.52	312.76
2010-05-07	Core	1.720	0.000	0.	0.35	0.61	280.94
2011-08-13	Core	1.953	0.009	-50.1	0.57	0.57	207.36
2012-09-15	Core	1.895	0.000	0.	0.28	0.59	407.44
2013-06-14	Core	1.677	0.016	-171.25	0.11	0.45	1173.47
2008-02-07	C2	0.059	5.989	-108.48	2.41	2.41	0.36
2008-06-09	C2	0.064	5.752	-125.32	0.61	0.61	6.14
2008-11-27	C2	0.057	5.657	-121.01	2.51	2.51	0.32
2010-05-07	C2	0.029	6.383	-125.63	0.28	0.28	13.15
2011-08-13	C2	0.046	6.408	-120.	0.92	0.92	1.90
2012-09-15	C2	0.048	7.065	-121.01	0.29	1.47	4.01
2013-06-14	C2	0.044	6.452	-123.81	1.95	1.95	0.41
2008-02-07	C3	0.136	3.944	-134.53	0.85	0.85	6.61
2008-06-09	C3	0.196	3.402	-131.14	1.80	1.80	2.14
2008-11-27	C3	0.117	4.129	-132.44	0.78	0.78	6.73
2009-09-05	C3	0.103	3.967	-131.41	1.79	2.72	0.75
2010-05-07	C3	0.083	3.896	-135.87	0.65	0.65	6.86
2011-08-13	C3	0.100	3.970	-131.5	1.78	1.78	1.11
2012-09-15	C3	0.103	4.258	-128.18	1.01	2.11	1.69
2013-06-14	C3	0.037	4.106	-139.6	0.81	0.81	2.01

Notes: [a] Relative distance to the phase center.
[b] Major and minor axis.
[c] Position angle of the component.

A.3   PKS 0637-752

Table A.5: Imaging parameters for 0637-752

Epoch yyyy-mm-dd	S_{total} [Jy]	S_{peak} [Jy/beam]	σ^{a} [mJy/beam]	$b_{\text{maj}}{}^{\text{b}}$ [mas]	$b_{\text{min}}{}^{\text{b}}$ [mas]	P.A.$^{\text{c}}$ [°]
2008-02-07	3.49	2.65	1.74	4.05	0.94	66.5
2008-03-28	2.57	1.29	1.17	1.52	0.42	-2.5
2008-08-08	3.44	2.65	1.40	3.26	1.36	2.7
2009-02-23	3.02	1.95	1.55	1.91	0.95	50.8
2010-03-12	3.31	2.75	1.13	4.56	3.84	-82.7
2010-10-28	3.91	1.51	1.16	0.91	0.41	2.0
2011-07-21	3.17	1.25	0.81	1.03	0.38	16.3
2012-04-27	3.21	1.55	1.23	1.38	0.41	9.5
2013-03-14	3.82	1.96	1.80	2.44	1.45	18.7

Notes: [a] Noise level of the image.
[b] Major and minor axis.
[c] Position angle.

Table A.6: Modelfit parameters for 0637-752

Epoch yyyy-mm-dd	Comp	S [Jy]	d^{a} [mas]	θ^{b} [°]	$b_{\mathrm{min}}^{\mathrm{c}}$ [mas]	$b_{\mathrm{maj}}^{\mathrm{c}}$ [mas]	T_{b} [10^9K]
2008-02-07	Core	2.527	0.000	0.	0.21	0.21	1598.78
2008-03-28	Core	2.102	0.008	-71.1	0.56	0.56	193.02
2008-08-08	Core	2.862	0.043	71.16	0.64	0.64	203.45
2009-02-23	Core	2.387	0.109	-73.27	0.51	0.97	141.12
2010-10-28	Core	1.535	0.022	-121.16	0.28	0.49	324.44
2011-07-21	Core	1.476	0.033	146.8	0.32	0.48	280.63
2012-04-27	Core	2.119	0.032	-40.52	0.38	0.38	426.14
2013-03-14	Core	1.471	0.000	0.	0.35	0.35	338.09
2008-03-28	C2	0.030	13.743	-89.63	1.01	1.01	0.86
2008-08-08	C2	0.048	12.640	-81.58	2.31	2.31	0.26
2010-10-28	C2	0.064	13.171	-85.88	0.30	1.65	3.69
2011-07-21	C2	0.032	12.400	-87.07	0.33	0.33	8.66
2012-04-27	C2	0.040	12.671	-91.53	0.44	0.44	5.97
2013-03-14	C2	0.030	14.102	-86.41	1.60	1.60	0.34
2008-02-07	C3	0.101	7.144	-91.43	1.01	1.01	2.86
2008-03-28	C3	0.072	5.487	-101.21	1.14	1.14	1.61
2009-02-23	C3	0.084	7.440	-93.19	2.29	2.29	0.46
2010-10-28	C3	0.091	7.472	-96.44	0.33	1.21	6.49
2011-07-21	C3	0.055	8.195	-91.22	0.45	0.45	7.81
2012-04-27	C3	0.070	7.759	-91.71	0.54	0.54	6.97
2008-02-07	C4	0.841	2.073	-87.37	0.93	0.93	28.46
2008-03-28	C4	0.368	2.156	-76.07	0.38	0.38	72.83
2008-08-08	C4	0.534	2.620	-93.94	0.82	0.82	23.18
2009-02-23	C4	0.524	2.525	-87.55	0.22	1.63	43.06
2010-10-28	C4	0.600	3.148	-91.78	0.59	0.98	30.18
2011-07-21	C4	0.293	3.519	-89.86	0.62	0.62	21.79
2012-04-27	C4	0.511	2.841	-91.59	0.79	0.79	23.60
2013-03-14	C4	0.703	2.699	-87.54	1.35	1.35	11.15
2010-10-28	C5	1.607	0.518	-78.88	0.23	0.60	337.07
2011-07-21	C5	0.831	0.423	-88.25	0.53	0.53	84.76
2012-04-27	C5	0.458	1.253	-78.99	0.29	0.29	162.29
2013-03-14	C5	1.595	1.178	-81.36	0.65	0.65	109.29

Notes: [a] Relative distance to the phase center.
[b] Major and minor axis.
[c] Position angle of the component.

A.4 PKS 1144-379

Table A.7: Imaging parameters for 1144-379

Epoch yyyy-mm-dd	S_{total} [Jy]	S_{peak} [Jy/beam]	σ^{a} [mJy/beam]	$b_{\text{maj}}{}^{\text{b}}$ [mas]	$b_{\text{min}}{}^{\text{b}}$ [mas]	P.A.$^{\text{c}}$ [°]
2008-02-07	1.74	1.67	0.60	3.14	0.79	-1.2
2008-03-28	1.63	1.58	0.35	3.40	0.69	-7.8
2008-08-08	1.92	1.77	0.46	3.39	1.24	-7.1
2009-02-27	1.21	1.13	0.36	3.54	1.31	13.2
2010-03-12	0.81	0.77	0.14	4.13	3.58	81.0
2010-10-28	2.14	1.91	0.26	2.66	0.44	-1.9
2011-07-21	1.95	1.69	0.36	2.59	0.55	5.3
2012-04-27	2.39	2.08	0.52	2.92	0.64	1.3

Notes: [a] Noise level of the image.
[b] Major and minor axis.
[c] Position angle.

Table A.8: Modelfit parameters for 1144-379

Epoch yyyy-mm-dd	Comp	S [Jy]	d^{a} [mas]	θ^{b} [°]	$b_{\mathrm{min}}{}^{\mathrm{c}}$ [mas]	$b_{\mathrm{maj}}{}^{\mathrm{c}}$ [mas]	T_{b} [10^9K]
2008-02-07	Core	1.683	0.010	8.02	0.15	0.15	2691.76
2008-03-28	Core	1.574	0.019	-6.07	0.08	0.08	9304.50
2008-08-08	Core	1.919	0.003	56.22	0.34	0.65	313.15
2009-02-27	Core	1.174	0.038	8.4	0.22	0.35	552.47
2010-03-12	Core	0.764	0.046	1.28	0.13	0.13	1738.22
2010-10-28	Core	2.132	0.002	-172.74	0.15	0.22	2327.95
2011-07-21	Core	1.067	0.065	-15.24	0.21	0.21	871.72
2012-04-27	Core	2.225	0.037	-0.35	0.24	0.38	858.06
2008-02-07	C2	0.010	10.350	-169.51	1.96	1.96	0.09
2008-03-28	C2	0.022	10.677	-175.31	5.74	5.74	0.02
2008-08-08	C2	0.018	9.708	-164.33	2.88	2.88	0.08
2009-02-27	C2	0.013	10.903	-169.04	4.77	4.77	0.02
2010-03-12	C2	0.014	9.640	179.4	2.26	6.01	0.04
2011-07-21	C2	0.014	10.453	-165.63	3.52	3.52	0.04
2008-02-07	C3	0.047	1.706	159.1	1.82	1.82	0.51
2008-03-28	C3	0.053	1.383	155.83	0.45	0.45	9.50
2009-02-27	C3	0.018	3.083	171.01	0.72	0.72	1.21
2010-03-12	C3	0.029	2.226	164.6	1.61	1.61	0.40
2011-07-21	C3	0.008	3.902	177.41	0.83	0.83	0.42
2012-04-27	C3	0.037	3.882	176.14	2.36	2.36	0.24

Notes: [a] Relative distance to the phase center.
[b] Major and minor axis.
[c] Position angle of the component.

A.5 PKS 0405-385

Table A.9: Imaging parameters for 0405-385

Epoch yyyy-mm-dd	S_{total} [Jy]	S_{peak} [Jy/beam]	σ^{a} [mJy/beam]	$b_{\text{maj}}{}^{\text{b}}$ [mas]	$b_{\text{min}}{}^{\text{b}}$ [mas]	P.A.$^{\text{c}}$ [°]
2008-02-07	1.41	1.31	0.28	4.89	3.33	-63.5
2008-03-28	1.26	0.93	0.64	2.86	0.61	2.6
2008-08-08	1.37	1.27	0.62	3.51	1.44	3.0
2009-02-23	1.10	0.94	1.42	1.97	0.93	32.8
2010-03-12	1.20	1.17	0.32	6.31	4.64	71.5
2010-10-28	1.52	1.23	0.49	3.36	0.56	-4.7
2011-07-21	1.14	0.82	0.84	2.31	0.44	1.1
2012-04-27	1.12	0.82	0.89	2.73	0.55	1.5
2013-03-14	1.42	0.89	1.09	2.08	0.56	-5.6

Notes: [a] Noise level of the image.
[b] Major and minor axis.
[c] Position angle.

Appendix B

Flux analysis of individual scans

B.1 Radio light curves in PKS 0405-385

The following plots show the total flux evolution within each epoch for PKS 0405-385. The x-axis shows the time relative to the start of the observing session in hours.

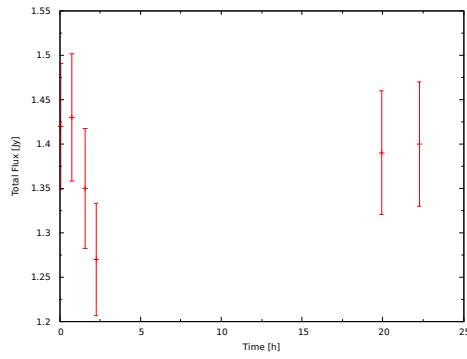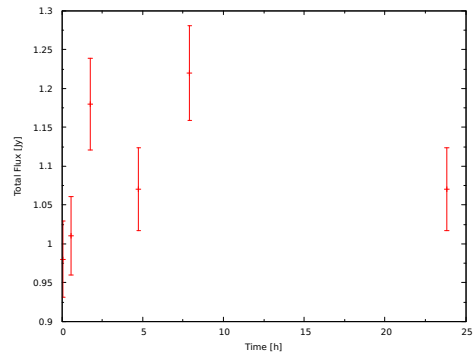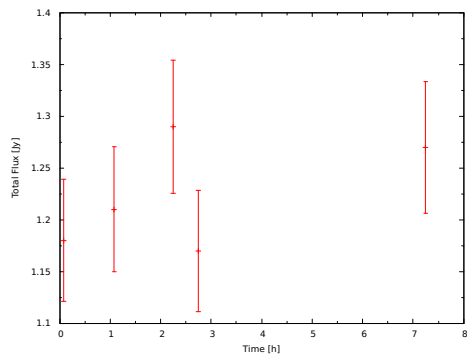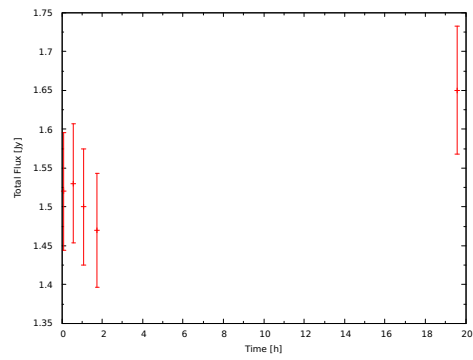**Figure B.1:** Total flux of PKS 0405-385 within each epoch.

(a) V252C

(b) V252E
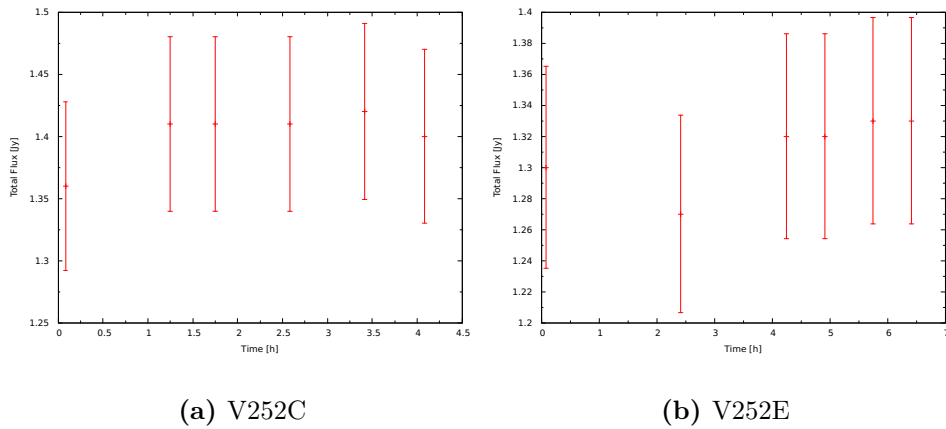
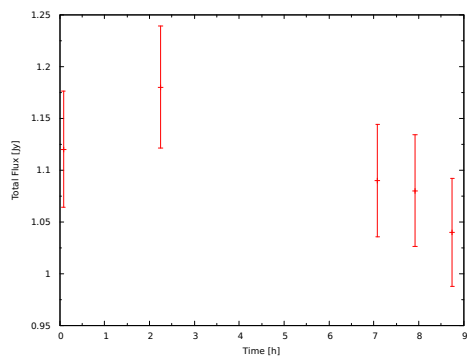**Figure B.1:** Total flux of PKS 0405-385 within each epoch.

(c) V252H

(d) V252K
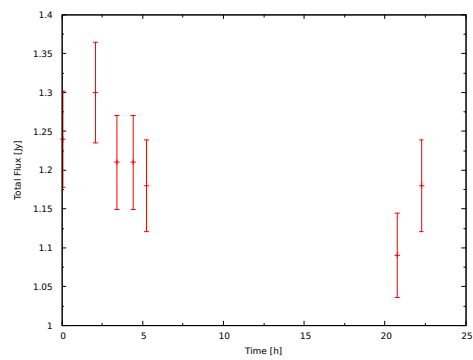

(e) V252P

(f) V252T

(g) V252Z
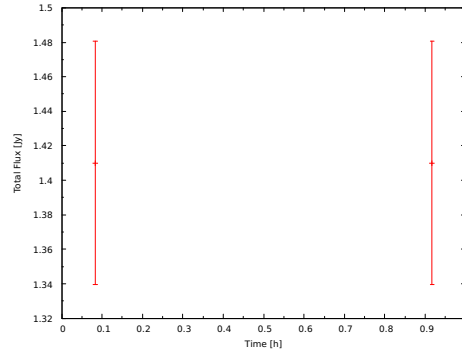

(h) V252AD

(i) V252AIJ

B.2 Estimation of errors of the flux analysis in individual scans

Table B.1 lists the flux values for the scan analysis in various sources. PKS 2204-540 and PKS 0637-752 are not known to show IDV. Assuming a constant source flux, the standard deviation and the relative error was calculated for these sources in order to estimate the typical error associated with measuring the flux for each scan using VLBI data. The same was done for the known IDV sources PKS 0405-385 and PKS 1144-279 in order to provide a fair comparison.

Table B.1: Modelfit parameters for 1144-379

Source	Epoch yyyy-mm-dd	Number of scans	S_{mean} [Jy]	σ^{a} [Jy]	Relative error [%]
2204-540	2008-02-07	5	1.087	0.038	3.47
	2008-06-09	6	1.22	0.052	4.26
	2008-11-27	6	1.002	0.021	2.15
	2009-09-05	6	0.87	0.039	4.50
	2010-05-07	5	0.683	0.0043	0.63
	2011-08-13	5	1.419	0.0152	1.069
	2012-09-15	6	1.208	0.057	4.72
0637-752	2008-02-07	6	3.47	0.11	3.11
	2008-03-28	6	3.27	0.061	1.87
	2008-08-08	6	3.37	0.11	3.19
	2009-02-23	6	2.99	0.077	2.57
	2010-03-12	6	2.386	0.091	2.79
	2010-10-28	6	3.90	0.19	4.97
	2011-07-21	6	3.23	0.12	3.67
	2012-04-27	7	3.198	0.095	2.97
	2013-03-14	5	3.73	0.17	4.52
0405-385	2008-02-07	6	1.402	0.021	1.52
	2008-03-28	6	1.312	0.023	1.78
	2008-08-08	6	1.377	0.059	4.3
	2009-02-23	6	1.088	0.094	8.65
	2010-03-12	5	1.224	0.054	4.38
	2010-10-28	5	1.534	0.069	4.48
	2011-07-22	5	1.102	0.052	4.73
	2012-04-28	7	1.201	0.064	5.34
	2013-03-14	2	1.41195	0.00049	0.035
1144-379	2008-02-07	6	1.757	0.059	3.38
	2008-03-28	6	1.782	0.018	1.01
	2008-08-08	6	1.907	0.081	4.25
	2009-02-27	6	1.18	0.11	9.27
	2010-03-12	6	0.839	0.040	4.80
	2010-10-28	6	2.23	0.14	6.46
	2011-07-21	5	1.961	0.074	3.75
	2012-04-27	6	2.38	0.11	4.65

Notes: [a] Standard deviation of the flux values of all scans.

Bibliography

Abdo A.A., Ackermann M., Ajello M., et al., 2011, ApJ 730, 101

Abdo A.A., Ackermann M., Ajello M., et al., 2009, ApJ 700, 597

Abdo A.A., Ackermann M., Ajello M., et al., 2010, Nat 463, 919

Abramowicz M.A., Fragile P.C., 2013, Living Reviews in Relativity 16, 1

Acero F., Ackermann M., Ajello M., et al., 2015, ApJS 218, 23

Agudo I., Gómez J.L., Casadio C., et al., 2012, ApJ 752, 92

Alfvén H., Herlofson N., 1950, Physical Review 78, 616

Antonucci R., 1993, ARA&A 31, 473

Baade W., Minkowski R., 1954, ApJ 119, 215

Bevington P.R., Robinson D.K., 2003, Data reduction and error analysis for
the physical sciences

Blandford R.D., Königl A., 1979, ApJ 232, 34

Blandford R.D., Payne D.G., 1982, MNRAS 199, 883

Blandford R.D., Znajek R.L., 1977, MNRAS 179, 433

Błażejowski M., Sikora M., Moderski R., Madejski G.M., 2000, ApJ 545, 107

Bloom S.D., Marscher A.P., 1996, ApJ 461, 657

Boettcher M., Harris D.E., Krawczynski H., 2012, Relativistic Jets from
Active Galactic Nuclei

Bridle A.H., Perley R.A., 1984, ARA&A 22, 319

Burke B.F., Graham-Smith F., 2010, An introduction to radio astronomy,
Cambridge University Press

Cohen M.H., Linfield R.P., Moffet A.T., et al., 1977, Nat 268, 405

Cotton W.D., 1995, In: Zensus J.A., Diamond P.J., Napier P.J. (eds.) Very Long Baseline Interferometry and the VLBA, Vol. 82. Astronomical Society of the Pacific Conference Series, p. 189

Deller A.T., Tingay S.J., Bailes M., West C., 2007, PASP 119, 318

Dermer C.D., Schlickeiser R., 1993, ApJ 416, 458

Dermer C.D., Schlickeiser R., Mastichiadis A., 1992, A&A 256, L27

Diamond P.J., 1995, In: Zensus J.A., Diamond P.J., Napier P.J. (eds.) Very Long Baseline Interferometry and the VLBA, Vol. 82. Astronomical Society of the Pacific Conference Series, p. 227

Edwards P.G., Piner B.G., Tingay S.J., et al., 2006, PASJ 58, 233

Fanaroff B.L., Riley J.M., 1974, MNRAS 167, 31P

Fossati G., Maraschi L., Celotti A., et al., 1998, MNRAS 299, 433

Fromm C.M., Perucho M., Mimica P., Ros E., 2016, A&A 588, A101

Fromm C.M., Perucho M., Ros E., et al., 2011, A&A 531, A95

Georganopoulos M., Perlman E.S., Kazanas D., McEnery J., 2006, ApJL 653, L5

Ghisellini G., 2016, Galaxies 4, 36

Ghisellini G., Celotti A., Fossati G., et al., 1998, MNRAS 301, 451

Giommi P., Polenta G., Lähteenmäki A., et al., 2012, A&A 541, A160

Gómez J.L., Lobanov A.P., Bruni G., et al., 2016, ApJ 817, 96

Gómez J.L., Martí J.M., Marscher A.P., et al., 1997, ApJL 482, L33

Großberger C., 2014, Ph.D. thesis, Friedrich-Alexander-Universität Erlangen-Nürnberg

Hada K., Doi A., Kino M., et al., 2011, Nat 477, 185

Hardcastle M.J., Krause M.G.H., 2013, MNRAS 430, 174

Heckman T.M., Best P.N., 2014, ARA&A 52, 589

Hewish A., Bell S.J., Pilkington J.D.H., et al., 1968, Nat 217, 709

Hirabayashi H., Hirosawa H., Kobayashi H., et al., 2000, PASJ 52, 955

Högbom J.A., 1974, Astron. Astrophys. Suppl. 15, 417

Homan D.C., Lister M.L., Kovalev Y.Y., et al., 2015, ApJ 798, 134

Homan D.C., Ojha R., Wardle J.F.C., et al., 2002, ApJ 568, 99

Houck J.C., Denicola L.A., 2000, In: Manset N., Veillet C., Crabtree D. (eds.) Astronomical Data Analysis Software and Systems IX, Vol. 216. Astronomical Society of the Pacific Conference Series, p. 591

Hovatta T., Aller M.F., Aller H.D., et al., 2014, AJ 147, 143

Hovatta T., Lister M.L., Aller M.F., et al., 2012, AJ 144, 105

Hovatta T., Lister M.L., Kovalev Y.Y., et al., 2010, International Journal of Modern Physics D 19, 943

Impey C.D., Tapia S., 1988, ApJ 333, 666

Jorstad S.G., Marscher A.P., Joshi M., et al., 2012, ArXiv e-prints

Jorstad S.G., Marscher A.P., Lister M.L., et al., 2005, AJ 130, 1418

Kadler M., Ojha R., TANAMI Collaboration 2015, Astronomische Nachrichten 336, 499

Kedziora-Chudczer L., 2006, MNRAS 369, 449

Kedziora-Chudczer L., Jauncey D.L., Lovell J.E.J., et al., 2001, In: Laing R.A., Blundell K.M. (eds.) Particles and Fields in Radio Galaxies Conference, Vol. 250. Astronomical Society of the Pacific Conference Series, p. 128

Kedziora-Chudczer L., Jauncey D.L., Wieringa M.H., et al., 1997, ApJL 490, L9

Kellermann K.I., 2002, Proc. Astron. Soc. Aust. 19, 77

Kellermann K.I., 2003, In: Zensus J.A., Cohen M.H., Ros E. (eds.) Radio Astronomy at the Fringe, Vol. 300. Astronomical Society of the Pacific Conference Series, p. 185

Kellermann K.I., Lister M.L., Homan D.C., et al., 2004, ApJ 609, 539

Kellermann K.I., Pauliny-Toth I.I.K., 1969, ApJL 155, L71

Khachikyan É.Y., Weedman D.W., 1971, Astrophysics 7, 231

Kovalev Y.Y., Kellermann K.I., Lister M.L., et al., 2005, AJ 130, 2473

Krichbaum T.P., Bach U., Graham D.A., et al., 2008, In: The role of VLBI in the Golden Age for Radio Astronomy., p. 1

Krolik J.H., 1999, Active galactic nuclei : from the central black hole to the galactic environment

Kunert-Bajraszewska M., Gawroński M.P., Labiano A., Siemiginowska A., 2010, MNRAS 408, 2261

Lawrence A., 1987, PASP 99, 309

Levenberg K., 1944, Quarterly of applied mathematics 2, 164

Li Z.Y., Chiueh T., Begelman M.C., 1992, ApJ 394, 459

Lister M.L., Aller H.D., Aller M.F., et al., 2009a, AJ 137, 3718

Lister M.L., Aller M.F., Aller H.D., et al., 2013, AJ 146, 120

Lister M.L., Cohen M.H., Homan D.C., et al., 2009b, AJ 138, 1874

Lobanov A.P., 1998, A&A 330, 79

Longair M.S., 2011, High Energy Astrophysics

Mankuzhiyil N., Ansoldi S., Persic M., Tavecchio F., 2011, ApJ 733, 14

Mannheim K., 1995, Astroparticle Physics 3, 295

Marscher A.P., 2006, Astronomische Nachrichten 327, 217

Marscher A.P., 2009, ArXiv e-prints

Marscher A.P., Gear W.K., 1985, ApJ 298, 114

Marscher A.P., Jorstad S.G., Agudo I., et al., 2012, ArXiv e-prints

McKinney J.C., Tchekhovskoy A., Blandford R.D., 2012, MNRAS 423, 3083

Müller C., Böck M., Wilms J., et al., 2012, ArXiv e-prints

Napier P.J., 1995, In: Zensus J.A., Diamond P.J., Napier P.J. (eds.) Very Long Baseline Interferometry and the VLBA, Vol. 82. Astronomical Society of the Pacific Conference Series, p. 59

Neeser M.J., Eales S.A., Law-Green J.D., et al., 1995, ApJ 451, 76

Nicolson G.D., Glass I.S., Feast M.W., Andrews P.J., 1979, MNRAS 189, 29P

Niinuma K., Kino M., Nagai H., et al., 2012, ApJ 759, 84

Norris R.P., 1988, In: Reid M.J., Moran J.M. (eds.) The Impact of VLBI on Astrophysics and Geophysics, Vol. 129. IAU Symposium, p. 485

Ojha R., Kadler M., Böck M., et al., 2010, A&A 519, A45

Penzias A.A., Wilson R.W., 1965, ApJ 142, 419

Perley R.A., Chandler C.J., Butler B.J., Wrobel J.M., 2011, ApJL 739, L1

Perucho M., 2013, In: European Physical Journal Web of Conferences, Vol. 61. European Physical Journal Web of Conferences, p. 02002

Piner B.G., Pant N., Edwards P.G., 2010, ApJ 723, 1150

Piner B.G., Pushkarev A.B., Kovalev Y.Y., et al., 2012, ApJ 758, 84

Rani B., Krichbaum T.P., Marscher A.P., et al., 2014, A&A 571, L2

Readhead A.C.S., 1994, ApJ 426, 51

Reber G., 1988, J. Roy. Astron. Soc. Can. 82, 93

Ricci R., Prandoni I., Gruppioni C., et al., 2004, VizieR Online Data Catalog 341

Rybicki G.B., Lightman A.P., 1979, Radiative processes in astrophysics, John Wiley & Sons

Ryle M., Elsmore B., Neville A.C., 1965, Nat 205, 1259

Savolainen T., Kovalev Y.Y., 2008, A&A 489, L33

Schmidt M., 1963, Nat 197, 1040

Schwab F.R., Cotton W.D., 1983, AJ 88, 688

Schwartz D.A., Marshall H.L., Lovell J.E.J., et al., 2000, ApJL 540, 69

Seyfert C.K., 1943, ApJ 97, 28

Shakura N.I., Sunyaev R.A., 1973, A&A 24, 337

Shen Z.Q., Wan T.S., Moran J.M., et al., 1997, AJ 114, 1999

Shen Z.Q., Wan T.S., Moran J.M., et al., 1998, AJ 115, 1357

Shepherd M.C., 1997, In: Hunt G., Payne H. (eds.) Astronomical Data Analysis Software and Systems VI, Vol. 125. Astronomical Society of the Pacific Conference Series, p. 77

Sikora M., Begelman M.C., Rees M.J., 1994, ApJ 421, 153

Singal A.K., 2009, ApJL 703, L109

Sokolovsky K.V., Kovalev Y.Y., Pushkarev A.B., Lobanov A.P., 2011, A&A 532, A38

Stawarz Ł., Ostrowski M., 2002, ApJ 578, 763

Stecker F.W., 2013, Phys. Rev. D 88, 047301

Stocke J.T., Morris S.L., Weymann R.J., Foltz C.B., 1992, ApJ 396, 487

Tavecchio F., Ghisellini G., 2008, MNRAS 385, L98

Tchekhovskoy A., McKinney J.C., 2012, MNRAS 423, L55

Tchekhovskoy A., McKinney J.C., Narayan R., 2012, In: Journal of Physics Conference Series, Vol. 372. Journal of Physics Conference Series, p. 012040

Tingay S.J., Murphy D.W., Lovell J.E.J., et al., 1998, ApJ 497, 594

Trüstedt J., 2013, *Master's thesis*, Julius-Maximilians-Universität Würzburg

Turner R.J., Ellingsen S.P., Shabala S.S., et al., 2012, ApJL 754, L19

Urry C.M., 1996, In: Miller H.R., Webb J.R., Noble J.C. (eds.) Blazar Continuum Variability, Vol. 110. Astronomical Society of the Pacific Conference Series, p. 391

Urry C.M., Padovani P., 1995, PASP 107, 803

Venturi T., 2010, In: 10th European VLBI Network Symposium and EVN Users Meeting: VLBI and the New Generation of Radio Arrays., p. 1

Véron-Cetty M.P., Véron P., 2000, A&AR 10, 81

Veron-Cetty M.P., Veron P., 2006, VizieR Online Data Catalog 7248, 0

Walker R.C., 1989, In: Perley R.A., Schwab F.R., Bridle A.H. (eds.) Synthesis Imaging in Radio Astronomy, Vol. 6. Astronomical Society of the Pacific Conference Series, p. 355

Wootten A., Thompson A.R., 2009, IEEE Proceedings 97, 1463

Zensus J.A., 1997, ARA&A 35, 607

Zensus J.A., Ros E., Kellermann K.I., et al., 2002, AJ 124, 662

Danksagung

An dieser Stelle möchte ich meine Dankbarkeit all jenen ausdrücken, die mich in meinem Studium begleitet und geprägt haben. Ohne ihre Unterstützung wäre diese Arbeit nicht möglich gewesen.

An erster Stelle möchte ich meinem Betreuer Prof. Dr. Matthias Kadler einen persönlichen Dank aussprechen. Er hat diese Arbeit nicht nur durch die Bereitstellung des Projekts möglich gemacht, sondern mein Interesse an der Astronomie durch seine Jet- und Methoden-Vorlesungen überhaupt erst geweckt. Vielen Dank für die Aufnahme in deine Arbeitsgruppe, für deinen Zuspruch und die vielen hilfreichen Diskussionen, ohne die diese Arbeit nicht in dieser Form nicht zustande gekommen wäre. Auch möchte ich mich bei Prof. Dr. Karl Mannheim für die Gelegenheit bedanken, am Lehrstuhl für Astronomie meine Abschlussarbeit schreiben zu können. Hervorheben möchte ich die positive Atmosphäre am Lehrstuhl. Das persönliche Engagement jedes Einzelnen und die daraus resultierenden gemeinsamen Aktivitäten verdeutlichen, dass hier Forschung gelebt wird.

Ich möchte mich bei allen Mitgliedern des TANAMI Projekts unter Leitung von Dr. Roopesh Ojha und Prof. Dr. Matthias Kadler bedanken, für die Bereitstellung der Datensätze und für das Feedback hinsichtlich der IDV-Quellen. Für die Einführung in die Auswertung von VLBI-Daten in Difmap möchte ich mich bei Dr. Jonas Truestedt und Paul Ray Burd ausdrücklich bedanken. Im selben Atemzug möchte ich auch Dr. Robert Schulz, Dr. Cornelia Müller, Amar Hekalo und Alexander Kappes nennen. Sie alle sind mir bei Rückfragen bezüglich Difmap und ISIS stets hilfreich zur Seite gestanden. Zudem bedanke ich mich bei Michael Kreter für seine Zusammenarbeit und das Erstellen der Fermi-Lichtkurven. Weiter möchte ich mich bei Dr. Dorith Glawion und Christoph Wendel bedanken, die mich mit offenen Armen in ihrem Büro aufgenommen haben.

Außerdem möchte ich mich bei Christoph Groß und Ulrich Krüger bedanken, die mich über mein ganzes Studium hinweg begleitet, unterstützt und mein Leben durch anregende Gespräche bereichert haben. Ohne euch wäre ich heute nicht, wo ich bin.

Schließlich möchte ich meiner Familie von ganzem Herzen danken, für ihre bedingungslose Unterstützung und dafür, dass sie mir dieses Studium ermöglicht haben. Die letzten Worte sind meiner Freundin Vanessa gewidmet: Ich kann meine Dankbarkeit dir gegenüber nicht in Worte fassen, ich bin einfach nur froh, dass es dich gibt.

Acknowledgements